

INTERNATIONAL SCHOOL FOR ADVANCED STUDIES

PHD COURSE IN THEORY AND NUMERICAL SIMULATION OF CONDENSED MATTER

ACADEMIC YEAR 2018/2019

**Multi-color Fermi-liquid theory of quantum transport
through a multilevel Kondo impurity**



SISSA

40!

THESIS SUBMITTED FOR THE DEGREE OF

DOCTOR OF PHILOSOPHY

Candidate:

Deepak Karki

Supervisor:

Prof. Mikhail Kiselev

Preface

The work presented in this thesis mainly focuses on the development of theoretical framework to describe the non-equilibrium transport through nano-sized quantum devices in the presence of strong electron-electron interactions and resonance scattering. The main objective of this research is to further understand the exotic transport processes in the non-equilibrium setup of a nanoscale system. The collection of findings presented in this thesis could be useful in the development of very efficient thermoelectric devices, quantum computation and information processing, and significantly improve the understanding of the many-body physics associated with the strongly-correlated electronic systems. In addition, the domain of applicability of the presented ideas and theoretical formulation are quite broad, not limited to the systems studied in this thesis.

To study the transport through the nano sized objects, several theoretical models, yet simple but very powerful, have been constructed for various type of multi-orbital quantum impurities with effective spin $S \geq 1/2$, in particular the quantum dots, carbon nanotubes and quantum point contacts, exhibiting the Kondo screening effects. The effects of applied voltage bias in the presence of finite temperature gradient are consistently treated within the full-fledged non-equilibrium Keldysh calculation. Thermoelectric transport of several variants of Kondo effects ranging from the conventional $SU(2)$ to exotic $SU(N)$ are explored using a controllable approximation based on local Fermi-Liquid theory known to be a paradigmatic approach for the description of a quantum impurity. Moreover, the low energy theory of non-equilibrium transport in multi-stage, multi-channel Kondo effects are investigated. A general method of full counting statistics of charge transfer in multi-stage Kondo effects has been developed and all the cumulants of charge current are studied. Different experimental setups have been suggested for the verification of new results presented in this thesis. Besides, several avenues for future research based on the ideas presented in this thesis are proposed and explained.

Contents

Preface	i
List of publications	v
1 Introduction and Overview	1
1.1 Brief overview of Kondo Physics	1
1.2 So what's still so new with Kondo effects in Fermi-liquid regime?	5
1.2.1 Thermoelectric transport through a spin-1/2 single channel Kondo effects: from $SU(2)$ to $SU(N)$ regime	5
1.2.2 Fermi liquid paradigm extended to multi-stage Kondo effects	9
1.3 Main Results	10
1.3.1 Thermoelectric power production in the presence of strong interactions and resonance scattering	11
1.3.2 Nonlinear theory of thermoelectrics with a $SU(N)$ Kondo impurity	12
1.3.3 Nonequilibrium transport through the two-stage, two-channel Kondo effect	13
1.3.4 Full counting statistics of the two-stage Kondo effect	15
1.4 Outline of this Thesis	16
2 Thermoelectrics with a $SU(N)$ Kondo impurity	17
2.1 Background	17
2.2 Thermoelectric transport	20
2.3 Output power of a heat engine in $SU(N)$ Kondo regime	22

2.4	Summary	25
3	Nonequilibrium theory of thermoelectrics of a $SU(N)$ Kondo impurity	26
3.1	Background	26
3.2	Theoretical formulation	29
3.3	Current Calculation	32
3.4	Seebeck effects	35
3.4.1	PH symmetric $SU(N)$ Kondo effects	37
3.4.2	Beyond half-filled $SU(N)$ Kondo effects	38
3.4.3	Paradigmatic $SU(4)$ Kondo effects	39
3.4.4	Possible resolution of the thermovoltage offset observed in experiment	41
3.5	Peltier effects	43
3.6	Summary	45
4	Two-color Fermi liquid theory for transport through a multilevel Kondo impurity	46
4.1	Background	46
4.2	Theoretical formulation	49
4.3	Fermi-Liquid Hamiltonian	50
4.4	Charge Current	53
4.4.1	Elastic current	54
4.4.2	Inelastic current	56
4.5	Transport properties	63
4.6	Summary	64
	Appendices	66
	Appendix 4.A Overview of flow from weak to strong coupling	66
	4.A.1 Weak coupling regime	66

4.A.2 Intermediate coupling regime	66
Appendix 4.B Counterterms	67
Appendix 4.C Elastic current	67
Appendix 4.D Net electric current	68
4.D.1 Linear Response (LR)	68
4.D.2 Beyond Linear Response (BLR)	69
Appendix 4.E Calculation of integrals	72
5 Full counting statistics of the two-stage Kondo effect	74
5.1 Background	74
5.2 Setup and model Hamiltonian	77
5.3 Full counting statistics	80
5.4 Summary	85
Appendices	86
Appendix 5.A Scattering corrections to the CGF	86
Appendix 5.B Interaction corrections to the CGF	87
Appendix 5.C Elastic integral	89
Appendix 5.D Inelastic Integral	90
6 Conclusions and perspectives	91
Bibliography	107

List of publications

This thesis is based on the following publications:

1. D. B. Karki and Mikhail N. Kiselev,
Nonlinear Seebeck effect of $SU(N)$ Kondo impurity,
[Phys. Rev. B **100**, 125426 \(2019\)](#) .
2. D. B. Karki and Mikhail N. Kiselev,
Effects of strong electron interactions and resonance scattering on power output of nano-devices,
[arXiv:1906.00724 \(2019\)](#).
3. D. B. Karki and Mikhail N. Kiselev,
Full counting statistics of the two-stage kondo effect,
[Phys. Rev. B **98**, 165443 \(2018\)](#).
4. D. B. Karki, Christophe Mora, Jan von Delft, and Mikhail N. Kiselev,
Two-color Fermi-liquid theory for transport through a multilevel Kondo impurity,
[Phys. Rev. B **97**, 195403 \(2018\)](#) [**Selected as Editors' Suggestion**].
5. D. B. Karki and Mikhail N. Kiselev,
Thermoelectric transport through a $SU(N)$ Kondo impurity,
[Phys. Rev. B **96**, 121403 \(2017\)](#) [**Rapid Communication**].

Chapter 1

Introduction and Overview

This chapter aims to provide a concise overview of this thesis including key results and corresponding discussions. We briefly review the current status of Kondo physics in relation to the topic under investigation and highlight the open problems of the field, their history, importance and challenges. We present the set of ideas and their origin that have been used in order to circumvent the difficulty associated with the problems which have been finally solved in this thesis. Afterward, the inclusive summary of the main finding and way of their experimental implementation are discussed. We close this chapter with short outline and suggestion about the effective reading of this thesis. All the materials presented in this thesis are based on the five recent publications [1-5] co-authored by the candidate.

1.1 Brief overview of Kondo Physics

The Kondo physics is connected with the novel experimental observation [6] reported in 1934 that some of the metals containing magnetic impurities showed an increase in resistivity when temperature is lowered below certain characteristics value. Since the electron-phonon scattering dominates the room temperature resistivity of a typical metal, the resistivity was expected to gradually decrease with decreasing temperature and saturates to a constant value when zero temperature is reached. This puzzle had persisted for almost three decades under the name “resistance anomaly” until its explanation put fourth by Jun Kondo in 1964 [7]. Kondo studied the interaction between the localized spin associated with the magnetic impurity and spins of conduction electrons in the metal using the method of perturbation. He showed that the resistance anomaly is connected with the increased scattering cross-section of the magnetic impurity due to the exchange interaction between localized spin and itinerant electrons in the metal. This interaction forms a cloud of conduction electrons around the impurity which screen the impurity spin and enhance the scattering of conduction electrons in the vicinity of Fermi level as illustrated in Fig 1.1. The main finding of Kondo that the resistance of a metal with magnetic impurities increases logarithmically when the temperature is lowered correctly describes the observed upturn of the low tempera-

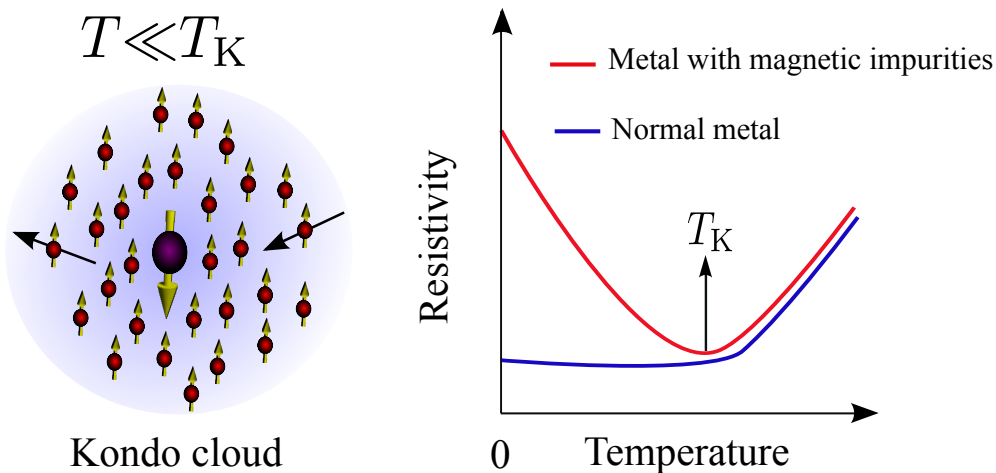


Figure 1.1: Left panel: Interaction between the localized spin and the spins of itinerant electrons results in the formation of screening cloud (Kondo cloud) of conduction electrons around the magnetic impurity. Right panel: The Kondo cloud enhances the scattering of conduction electrons in the vicinity of Fermi-level which give rise to the increase of resistivity below certain characteristics temperature, the Kondo temperature T_K . In normal metal (without magnetic impurities) this anomalous behavior is absent and the conductance below T_K saturates to a constant value set by residual impurities and structural defects.

ture resistance [8]. This celebrated discovery, however, resulted in an unphysical prediction that the resistance approaches towards infinity when the temperature is further lowered. Therefore, Kondo’s original prediction is applicable just above certain characteristics temperature scale called the Kondo temperature T_K . Below T_K the ordinary perturbation theory breaks down, therefore, a complete description of Kondo effect requires non-perturbative methods. A decade after the Kondo’s discovery, in 1974 Kenneth Wilson developed a non-perturbative method known as “numerical renormalization” [9] to provide the complete description of the physics associated with the Kondo effect in the broad range of temperatures. Wilson work explained that at temperature well below the Kondo temperature, $T \ll T_K$, the magnetic moment of the impurity gets screened completely by the spins of the conduction electrons in the metal and forms the spin singlet ground state. Later on the method of numerical renormalization has been extended to study the transport properties of the system [10, 11].

The formation of singlet ground state due to the Kondo effect leads to an increase of the probability for an electron to scatter by the impurity. This increased scattering cross-section results in the increased resistivity of a magnetic impurity embedded in the bulk sample. Does the same result apply to the impurity residing in a tunneling barrier separating two large electronic reservoirs, a typical transport setup in nanostructure? In this particular case the increased scattering rate leads to an enhanced probability for an electron to tunnel through the barrier, i.e., the enhanced scattering couples the electron states in two reservoirs. Therefore, in contrast to the Kondo effect in bulk sample, the conductance of nanostructure setup with Kondo effect increases with decreasing

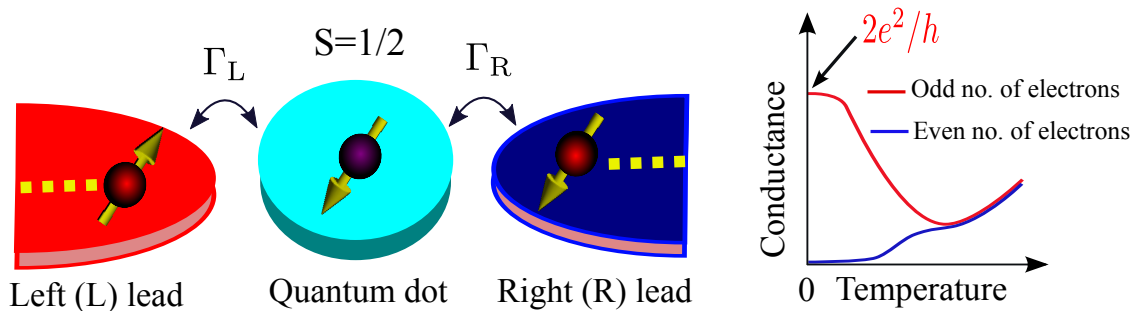


Figure 1.2: Left panel: Schematic representation of a QD with intrinsic spin $S=1/2$ tunnel coupled to two conducting reservoirs, the left (L) and right (R). The tunneling from/to the QD is controlled by intrinsic local level widths $\Gamma_{L/R}$. Right panel: The temperature dependence of conductance in a QD nano structure. The QD with odd number of electrons posses intrinsic spin $S=1/2$, which interact with the itinerant electrons in the electronic reservoirs. This exchange interaction results in the Kondo effect, thus, the zero temperature conductance reaches the maximum value known as the quantum of conductance. If the number of electrons in QD is even, the Kondo effect is absent since the total spin adds up to zero. Consequently, at zero temperature the electrons in the left reservoir remain completely decoupled from that in right reservoir resulting in the nullification of the conductance.

temperature and reaches its maximal value equal to the two times of quantum of conductance at $T=0$ as illustrated in Fig. 1.2. Similar behavior of conductance had been reported as a function of applied voltage bias ΔV [12, 13]. This zero-bias anomaly of the conductance were later explained in 1969 in the context of Kondo effect [14, 15]. Afterward several exciting theoretical works in Kondo effect contributed towards the better understanding of the phenomena [9, 16–19]. The growing interest in the field of Kondo effect was further intensified by the celebrated work of Philippe Nozieres [20] in 1974, where he proposed a low-energy theory called local Fermi-liquid theory of Kondo effect. In 1978 Duncan Haldane presented an expression of T_K in terms of the parameters of the Anderson model [21] which helped in further expanding the scope of Kondo paradigm. Several theoretical perseverances [22–26] finally guided experiment for the first observation of Kondo effect in semiconductor QD as reported in 1998 by two different groups [27, 28]. The temperature dependence of conductance $G(T)$ for a spin $S=1/2$ Kondo effect in the strong-coupling regime ($T \ll T_K$) as proved by theories and experiments [29] takes the form

$$G(T) = \frac{2e^2}{h} \frac{4\Gamma_L\Gamma_R}{(\Gamma_L + \Gamma_R)^2} \left[1 - \left(\frac{\pi T}{T_K} \right)^2 \right], \quad (1.1)$$

with e^2/h the quantum of conductance and $\Gamma_{L/R}$ are the intrinsic local level width associated with the tunneling from/to the QD. This scaling form is demonstrated in the right panel of Fig. 1.2. The equilibrium conductance behavior Eq. (1.1) was then extended to the out-of-equilibrium situation in the early experiment reported in Ref. [30]. With the growing interest in Kondo effects, researchers of different discipline started to use this paradigmatic phenomena as a clean testbed for the study of strongly correlated electron physics [31]. Kondo effect is also serving as a playground for the study of nonequilibrium physics which is regarded as quite challenging yet ubiquitous at the

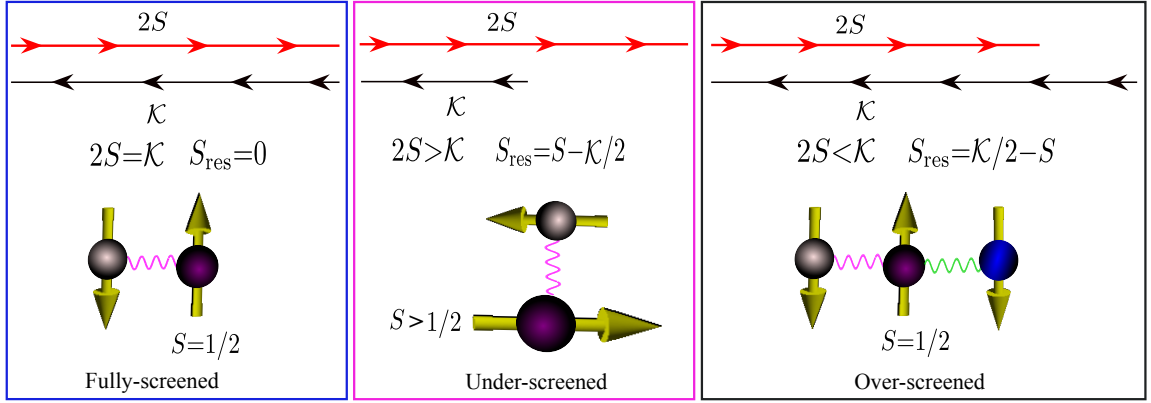


Figure 1.3: Classification of Kondo effects into fully-screened, under-screened and over-screened cases. The complete screening of localized spin S by the conduction electrons forms a singlet with zero residual moment $S_{\text{res}}=0$. These fully-screened Kondo effects falls into the FL universality class. While the under-screened Kondo effects can also be described to some extent in terms of FL paradigm, the over-screened situations are beyond the scope of FL theory.

nanoscale. The nonequilibrium physics associated with the system can, in practice, be extracted from the current through the system in response to possibly simultaneously occurring voltage and temperature biases. The application of two affinities (voltage bias and temperature gradient) across the nanoscale setup allows to study the thermoelectric transport, such as the Seebeck and Peltier effects. The experimental measurement of thermoelectric power (Seebeck coefficient) of Kondo correlated QD has been started in the mid 2000s [32] to use it as an independent probe of associated many-body physics and apply for the energy harvesters used in modern quantum technologies. Recent experiments [33–38] have further broaden the field of nano scale themoelectricity production utilizing the enhanced electronic properties of Kondo correlated nano devices. Going further into the detail of Kondo paradigm, at this stage, it is crucial to differentiate among different classes of Kondo effects and associated transport fingerprints. The competition among localized degrees of freedom, number of conduction channel, number of electronic reservoirs etc., can exhibit different forms of Kondo effects [26]. In the following we briefly summarize the broad classification of Kondo effects.

It is almost four decades since the seminal work of Nozieres and Blandin (NB) [22] about the Kondo effect in *real* metals. The concept of the Kondo effect studied for impurity spin $S=1/2$ interacting with a single orbital channel $\mathcal{K}=1$ of conduction electrons [7, 16–18, 20, 23, 39–41] was extended in [22] for arbitrary spin S and arbitrary number of channels \mathcal{K} . A detailed classification of possible ground states corresponding to the under-screened $\mathcal{K}<2S$, fully screened $\mathcal{K}=2S$ and overscreened $\mathcal{K}>2S$ Kondo effect has been given in [26, 42, 43] as shown in Fig. 1.3. In the fully screened case the conduction electrons completely screen the impurity spin to form a singlet ground state [44]. As a result, the low-energy physics is described by a local Fermi-Liquid (FL) theory [20, 22]. In the under-screened Kondo effect, the available conducting channels are not enough to provide complete screening [45, 46]. Thus, there is a finite concentration of impurities with a residual spin contributing to the thermodynamic and transport properties. In contrast to the underscreened

and fully-screened cases, the physics of the overscreened Kondo effect is not described by the FL paradigm resulting in dramatic change of the thermodynamic and transport behaviour [10]. However, in this thesis we restrict ourselves to the study of non-equilibrium transport properties of fully screened Kondo effects described by FL theory.

1.2 So what's still so new with Kondo effects in Fermi-liquid regime?

When the number of conduction channels \mathcal{K} and the spin of localized impurity S bears the specific form $\mathcal{K}=2S$, the impurity spin gets fully screened which forms a ground state singlet. At strong-coupling regime the complete screening give rise to a FL. The usual situation corresponds to the case of spin $S=1/2$ impurity interacting with the single channel $\mathcal{K}=1$ of conduction electrons. Furthermore, it has been argued that in real metals the spin-1/2 single-channel Kondo effect is unlikely to be sufficient for the complete description of the physics of a magnetic impurity in a non-magnetic host [29, 47–52]. In many cases truncation of the impurity spectrum to one level is not possible and besides there are several orbitals of conduction-electrons which interact with the higher spin $S>1/2$ of the localized magnetic impurity [10], giving rise to the phenomenon of multi-stage, multi-channel Kondo screening [24, 53] even in the FL regime. The most general case of experimental relevance for the multi-stage Kondo paradigm is the spin $S=1$ impurity screened by two channels $\mathcal{K}=2$ of conduction electrons [47, 49]. While the single channel spin-1/2 Kondo effects are being widely studied, the fully screened Kondo effects with higher spin $S>1/2$ have received much less attention over the past years. Though the ground state is of FL universality class, the consistent treatment of the competition between the channels creates the major complexity of the problem. Given that, we consider two prototypical examples of the fully screened Kondo effects: i) spin-1/2 single channel and ii) spin-1 two channel and develop a local FL theory of quantum transport applicable in the strong-coupling regime to study the non-equilibrium transport in the presence of voltage bias and temperature gradient. In the following section we discuss in detail about “Why we took this route?” and “What are our contributions to above mentioned fields of fully screened Kondo effects?”.

1.2.1 Thermoelectric transport through a spin-1/2 single channel Kondo effects: from $SU(2)$ to $SU(N)$ regime

Greatly enhanced thermoelectric response of nano scale systems over conventional bulk materials has revived further the field of thermoelectricity [54–56]. Rapid development of nanotechnology has fueled several exciting thermoelectric experiments on nano materials and their theoretical formulation [57] to fulfill the urgent demand of energy harvesters for quantum technologies. The charge quantization in quantum devices [58] furnishes a controllable comprehension of underlying transport processes. Consequently, spectacular thermoelectric measurement of prototypical nano scale systems such as quantum dots (QDs), carbon nano-tubes (CNTs), quantum point contacts (QPCs),

etc has been reported over the past years [54, 59]. So why Kondo effect for thermoelectricity?

Why Kondo effect for thermoelectricity?

At the nanoscale, the single electron effects become very important resulting in the ubiquitousness of electron interactions. Equivalently, strong Coulomb interaction is at the cornerstone of nano devices. The resonance scattering often combines with strong electron interaction which drives the system to possess very peculiar functionality [60, 61] due to the emergence of Kondo effect. As follows from the FL theory, the thermopower \mathcal{S} (Seebeck effect) of bulk metals is directly proportional to the temperature T and inversely proportional to the Fermi energy ε_F [62]; $\mathcal{S}_{\text{bulk}} \propto T/\varepsilon_F$. The resonance scattering on a quantum impurity, however, dramatically enhances this effect due to the emergence of new quasi-particle resonances at the Fermi level described by the Kondo effect [10, 20, 22]. The contribution to the Seebeck effect proportional to the concentration of impurities at low T , as a result, scales as $\mathcal{S}_{\text{Kondo}} \propto T/T_K$ [10, 62] where T_K is a characteristic energy defining the width of the Kondo resonance, the Kondo temperature. Since $T_K \ll \varepsilon_F$ we arrive at the conclusion that $\mathcal{S}_{\text{Kondo}} \gg \mathcal{S}_{\text{bulk}}$. The Kondo effect in nano-devices is, thus, a key for enhancing the thermopower production [32]. The tunable thermo-transport through nano-devices controlling the heat flow is needed for efficient operation of quantum circuits elements: single-electron transistors, quantum diodes etc to perform controllable heat guiding.

Can we really produce appreciable thermopower with Kondo devices?

Let us consider the general case of spin-1/2 Kondo impurity tunnel coupled to two conducting reservoirs, the left (L) and right (R). Furthermore, the rotation of the electrons in the reservoirs and the impurity are assumed to be described by the SU(2) transformation (we refer this particular case as “conventional SU(2) Kondo effect”). In addition, the left and right reservoirs are in equilibrium, separately, at temperatures T_γ ($\gamma=L, R$) and chemical potentials μ_γ respectively. Note that throughout the calculations we use the system of atomic unit, $\hbar=k_B=e=1$ unless explicitly written. As far as the condition $T_L \neq T_R$ and $\mu_L \neq \mu_R$ is satisfied, heat current (I_h) and charge current (I_c) start to flow from one reservoir to another via the Kondo impurity. To be more explicit, we consider the voltage bias and temperature gradient across the impurity in such a way that $\mu_L - \mu_R = \Delta V$ and $T_L - T_R = \Delta T$. We choose the right reservoir to define the reference temperature, $T_{\text{ref}} \equiv T_R = T$. Then the charge and the heat currents in the linear response theory are connected by the Onsager relations [63, 64],

$$\begin{pmatrix} I_c \\ I_h \end{pmatrix} = \begin{pmatrix} L_{11} & L_{12} \\ L_{21} & L_{22} \end{pmatrix} \begin{pmatrix} \Delta V \\ \Delta T \end{pmatrix}. \quad (1.2)$$

The Onsager transport coefficients L_{ij} in Eq. (2.2) provide all the thermoelectric measurements of interests in linear response regime [65]. As we anticipated earlier, the low energy transport via fully screened Kondo impurity is completely described by a local FL theory [20]. Therefore the coefficients L_{ij} are characterized by the single particle T-matrix $T_\sigma(\varepsilon)$ of FL quasi-particles [29, 65]. Such connection is governed by defining the transport integrals $\mathcal{I}_n(T)$ ($n=0, 1$ and 2) in terms of

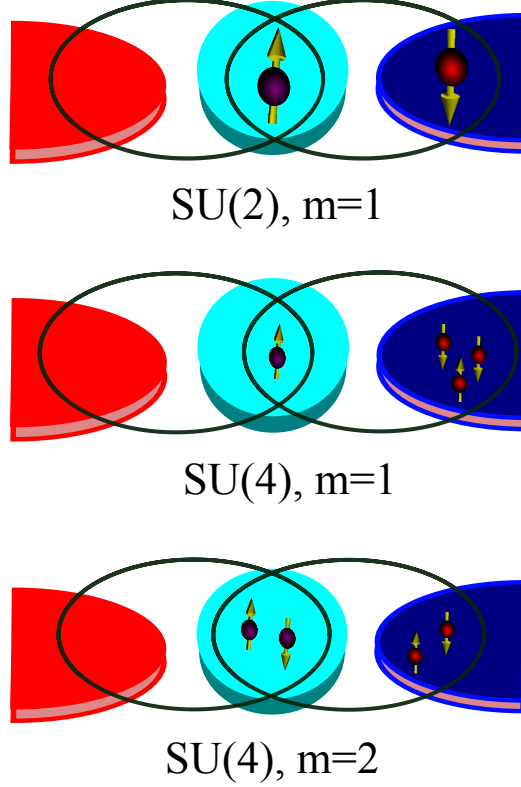


Figure 1.4: The ground state of the conventional SU(2) and SU(4) Kondo effect. While the SU(2) Kondo effect occurs at half filling, the SU($N = 4$) Kondo effect offers a non-trivial occupation away from the PH-symmetric point, namely the $m=1$ and $m=3$ state (not shown in figure since it is related to the case of $m=1$ via the PH symmetric transformation).

the imaginary part of the T-matrix [29],

$$\mathcal{I}_n(T) = \sum_{\sigma=\uparrow,\downarrow} \int_{-\infty}^{\infty} \frac{d\varepsilon}{2\pi} \varepsilon^n \left[-\frac{\partial f(\varepsilon)}{\partial \varepsilon} \right] \text{Im} [-\pi\nu T_{\sigma}(\varepsilon)]. \quad (1.3)$$

Here $f(\varepsilon) = [1 + \exp(\varepsilon/T)]^{-1}$ is the equilibrium Fermi-distribution function of the reference reservoir, the term $\text{Im} [-\pi\nu T_{\sigma}(\varepsilon)]$ represents the spectral function of the Kondo impurity. Density of states per species for the one-dimensional channel ν and the Fermi-velocity v_F are related as $\nu = 1/2\pi v_F$. Then the transport coefficients characterizing the charge current are expressed in terms of the transport integrals, namely, $L_{11} = \mathcal{I}_0$ and $L_{12} = -\mathcal{I}_1/T$ [66]. The electrical conductance is given by the coefficient L_{11} and the thermopower (Seebeck coefficient) by the ratio L_{12}/L_{11} .

Carefully analyzing the form of Eq. (1.3) we see that the coefficient L_{11} will be non-zero if the spectral function is either fully symmetric or contain some terms that are symmetric with energy ε . In contrast, the Onsager's coefficient L_{12} vanishes for symmetric spectral function, thus, is the measure of the asymmetry of the spectral function. Now the major concern is what is the spectral function of the SU(2) Kondo impurity? Is it fully symmetric with respect to energy? The answer is “yes it is fully symmetric” in accordance with the expression of spectral function in the

strong-coupling regime [29],

$$\text{Im}[-\pi\nu T_\sigma(\varepsilon)] = 1 - \frac{3}{2} \left(\frac{\varepsilon}{T_K^{\text{SU}(2)}} \right)^2 - \frac{1}{2} \left(\frac{\pi T}{T_K^{\text{SU}(2)}} \right)^2. \quad (1.4)$$

Here $T_K^{\text{SU}(2)}$ is the Kondo temperature of SU(2) Kondo effect. The Eq. (1.4) shows that the thermopower of a conventional Kondo effect vanishes in linear response level of calculation. What is the simple explanation of this behavior? The spin-1/2 SU(2) Kondo impurity physics arises at the half-filled particle-hole (PH) symmetric regime. We refer to “electrons” as quasi-particles above ε_F and “holes” as the excitations below ε_F . The PH symmetry, being responsible for the enhancement of the electric conductance, suppresses however the thermo-electric transport. This is because the heat current carried by electrons is completely compensated by the heat current carried by holes resulting the nullification of power production. The emergent PH symmetry in SU(2) Kondo regime is shown in the upper panel of the Fig. 1.4. How to bypass the PH symmetry problem occurring with conventional SU(2) Kondo effects so as to achieve appreciable thermopower? In addition, it is very rare to realize the system with exact PH symmetry, therefore, one needs a theoretical framework that can capture the breaking of PH symmetry in order to describe the experimental results. How to develop a low energy theory of transport that is beyond the SU(2) Kondo paradigm?

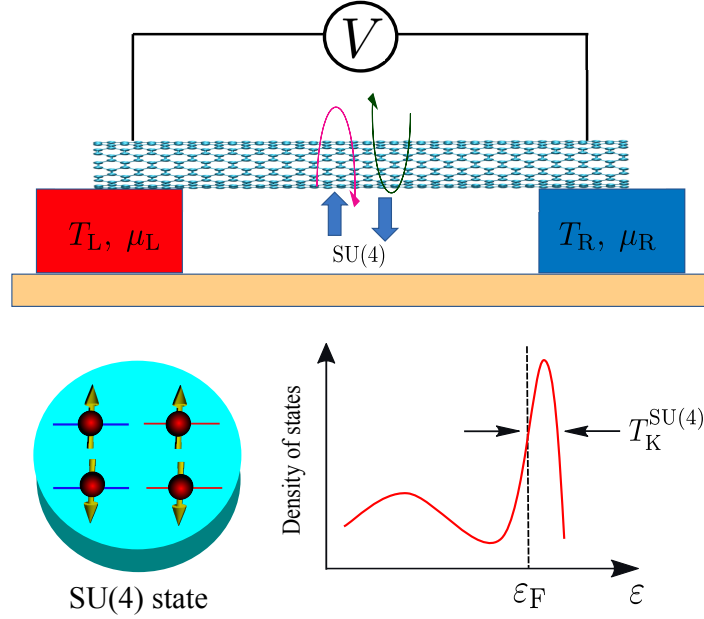


Figure 1.5: Upper panel: An example of SU($N=4$) Kondo correlated heat engine where a CNT is connected between two fermionic reservoirs, the hot (red) and the cold (blue). Voltage bias ΔV and temperature gradient $\Delta T=T_L-T_R$ are applied across the CNT quantum dot. Lower panel: The doubly degenerate orbital degree of freedom in CNT combines with spin degeneracy to form a Kondo effect with SU(4) symmetry group. The SU(4) Kondo effects occur with at most three electrons. While the state with two electron forms a PH symmetric state, the one or three electron case explicitly breaks the PH symmetry. The density of states (spectral function) for beyond PH symmetric SU(4) Kondo effects is not symmetric with respect to the Fermi level. Therefore, these systems offer huge thermopower and other fascinating thermoelectric transport properties.

SU(2) to SU(N) Kondo effects: root of achieving huge thermopower

From the above discussion we see that to achieve appreciable thermopower, the occupation factor of the quantum impurity should be integer, while the PH symmetry should be lifted. Such properties are generic for the SU(N) Kondo models with the filling factors different from $1/2$ (see Fig. 1.4). That means, the SU(N) Kondo model with integer occupancy m offers the possibility of avoiding half-filled regime so as to achieve the enhanced thermoelectric power production over the conventional SU(2) Kondo correlated systems [1, 4, 67]. The orbital degeneracy of the quantum impurity combines with the true spin symmetry to form the Kondo effect described by higher symmetry group SU(N). Here the occupancy factor m takes all possible values starting from 1 to $N-1$. The paradigmatic SU(4) Kondo physics has been experimentally studied in CNTs [35, 68–72], double QDs [73] and single-atom transistor [74]. Various theoretical works [75–80] have contributed towards better understanding of SU(4) Kondo physics over past years. The SU(4) Kondo effect in CNT is demonstrated in Fig.1.5. In addition, exciting proposals have been put forth for the experimental realization of different variants of SU(N) Kondo systems. Possible realization of SU(3) Kondo effects using triple QDs with three and four edge states of the quantum Hall effects was suggested in Ref. [81], which been verified recently using numerical renormalization group study [82]. The proposals for the solid-state realization of SU(6) [83] and SU(12) [84] Kondo effects have likewise attracted considerable attentions both theoretically and experimentally. Beside obtaining the solid-state realization of these exotic SU(N) Kondo effects, an increasing effort has been put in their cold atomic realization [85–88]. Given that, we develop a low energy theory of thermoelectric transport through a SU(N) Kondo impurity based on the local FL theory in combination with non-equilibrium Keldysh approach. Dramatic transport characteristics such as huge power factor, thermopower and Peltier coefficients with a SU($N>2$) Kondo effects are reported.

1.2.2 Fermi liquid paradigm extended to multi-stage Kondo effects

Multi-orbital quantum impurity with effective spin $S=1$ connected to two terminals can results in a Kondo effect exhibiting two-stage screening [2]. The first-stage screening process constitutes an under-screened Kondo effect where the impurity spin is effectively reduced from $S=1$ to $S=1/2$. Subsequently, second-stage screening leads to complete screening of the impurity spin and the formation of a Kondo singlet. This feature of screening is called two-stage Kondo (2SK) effect [45, 49]. This two-stage screening process is illustrated in Fig. 1.6. The low energy description of such 2SK effects is still governed by a local FL theory. Nonetheless, transport properties of such FL get modified in dramatic ways compared to single channel Kondo effects [2]. The strong interplay between two conduction channels, both close to resonance scattering, causes strikingly different transport features over single channel case. The lack of compatible cure of the two Kondo resonances makes the 2SK paradigm far from being trivial for several years [45, 49, 89]. Given that, we develop two-color Fermi-liquid theory to analyze the equilibrium and non-equilibrium transport properties of a generic 2SK effects based on the non-equilibrium Keldysh formalism. The generalization of Kondo screening in three and beyond stages are also within the scope of developed formalism. In addition to the non-equilibrium charge current, all of its moments are studied using the method of

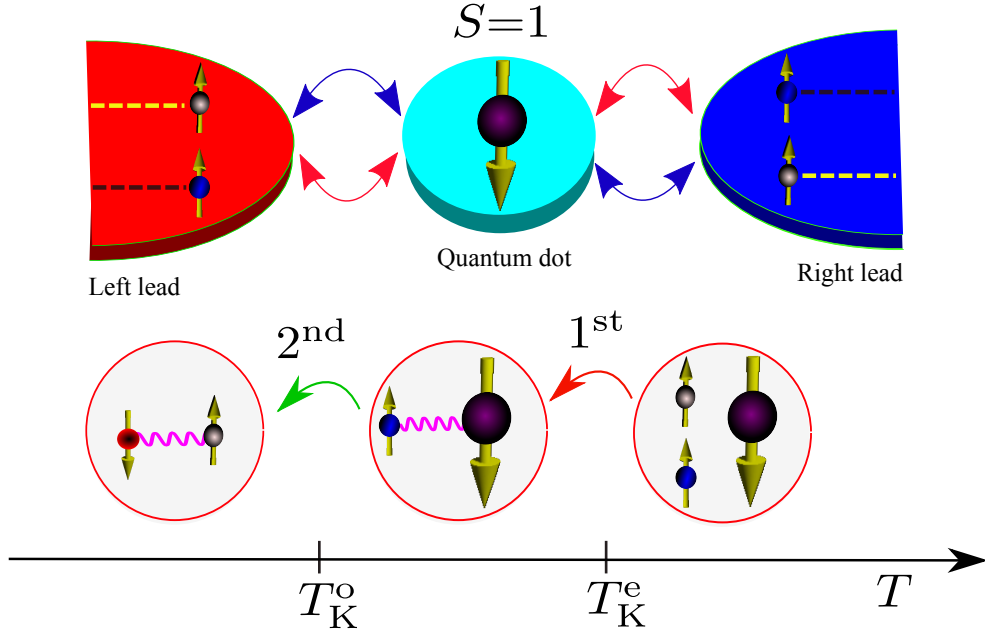


Figure 1.6: Upper panel: Schematic representation of a quantum impurity with an effective spin $S=1$ tunnel-coupled to two electronic reservoirs as a prototypical example of the two-stage, two-channel Kondo effect. The symmetric and anti-symmetric combinations of electrons states in the reservoirs are represented by “even (e)” and “odd (o)” channels. The Kondo temperatures of even/odd channels are $T_K^{e/o}$. Lower panel: Flow diagram of two-stage Kondo model from weak to strong coupling.

full counting statistics. The absence of zero-bias anomaly and non-monotonicity of FL transport coefficients are demonstrated as the hallmarks of multi-stage Kondo effects in its strong-coupling regime $T \ll \min(T_K^e, T_K^o)$. A novel method of measuring FL transport coefficients of the 2SK effect by the independent measurements of charge current and its noise is proposed.

1.3 Main Results

The main results presented in this thesis can be divided into two broad categories. The study of non-equilibrium thermoelectrics with a $SU(N)$ Kondo impurity constitutes the first part. In this part, two reciprocal measures of thermoelectrics namely, the Seebeck and Peltier coefficients are investigated. The role of junction asymmetry in enhancing the thermoelectric transport coefficients is discussed. Moreover, the power output of a heat engine in $SU(N)$ Kondo regime is explored which is shown to be bounded from below by zero with the upper bound strictly set by the filling factor and reference temperature. The second part is devoted to the development of a local FL theory for the non-equilibrium transport through higher spin $S=1$ quantum impurity in the strong-coupling Kondo regime. The strong-coupling regime of a $S=1$ quantum impurity interacting with the two external reservoirs constitutes a pro-typical example of two-stage, two-channel Kondo effect. The absence of zero-bias anomaly and the non-monotonicity of the transport coefficients are demonstrated to be

the major hallmarks of multi-stage, multi-channel Kondo effects. The second part also contains the study of full counting statistics of the multi-stage Kondo paradigm. In the following we announce the key results presented in this thesis.

1.3.1 Thermoelectric power production in the presence of strong interactions and resonance scattering

Enhancing power production in nano-devices has been limited due to the recent finding of quantum mechanical upper bound in power output of non-interacting systems P_{\max}^0 [90, 91],

$$P_{\max}^0 \leq \frac{N\pi^2}{h} A_0 \Delta T^2, \quad A_0 \simeq 0.0321, \quad (1.5)$$

with h Planck's constant, N is the number of conduction modes and ΔT is the applied temperature gradient. The Eq. (1.5) illustrates the fact that the power output grows linearly with number of conduction modes N . However, it has been noticed that, most of the thermoelectric engines are limited to the setup with $N \sim 1$. The search towards the physical realization of the systems with $N \gg 1$ is one of the major research concern of the field. Note that the recent experiment [92] has reported almost 50% of upper bound of power production in one dimensional nanowire. How to enhance further the achievable power output of a generic nano device is another hottest research topic of the field [92]. Furthermore, since the interactions are ubiquitous at nano-scale, examining the universality of predicted upper bound in the presence of strong interactions looks like a earnest need and serious challenge. In this facet, we develop a local Fermi-liquid approach to examine the influences of strong interactions and resonance scattering on the power production of a generic nano device in $SU(N)$ Kondo regime with arbitrary filling factor m . We uncover the bounded value of power factor with lower bound zero and upper bound set by the filling factor and reference temperature. While the lower bound is strictly satisfied by half-filled Kondo impurity, the upper bound explicitly depends on the reference temperature for given filling factor. These findings are summarize with the an equation of output power of a $SU(N)$ Kondo impurity P_{\max}^{Kondo} ,

$$P_{\max}^{\text{Kondo}} = \frac{N\pi^2}{h} \left[\frac{1}{36} \frac{\sin^2\left(\frac{2\pi m}{N}\right) \left(\frac{\pi T}{T_K^{\text{SU}(N)}}\right)^2}{\sin^2\left(\frac{\pi m}{N}\right) + \frac{1}{3} \left(\frac{\pi T}{T_K^{\text{SU}(N)}}\right)^2 \frac{N+1}{N-1} \cos\left(\frac{2\pi m}{N}\right)} \right] \Delta T^2, \quad (1.6)$$

where T is the reference temperature and $T_K^{\text{SU}(N)}$ is the Kondo temperature. The output power Eq. (1.6) explicitly depends on the internal parameters of the system such as N , m and $T_K^{\text{SU}(N)}$ unlike the non-interacting systems. With the help of Eq. (1.6), we report about 50% of quantum bound of power production in an experimentally studied $SU(4)$ Kondo effect in carbon nano tube setup. In addition, we demonstrate that the $SU(N)$ Kondo effects away from half-filling can provide an experimental realization with $N \gg 1$ so as to increase the total power production of a heat engine.

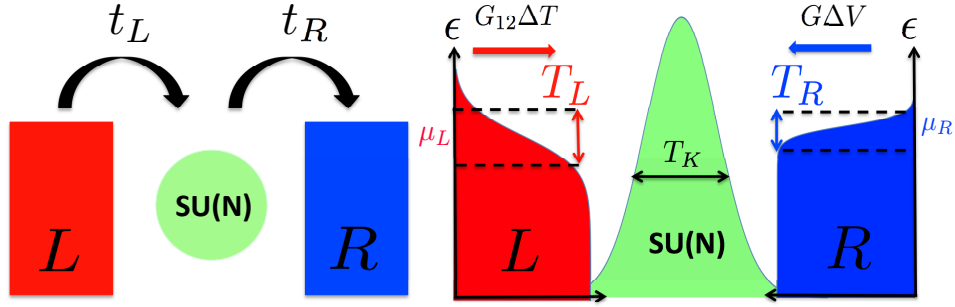


Figure 1.7: Left panel: Schematic representation for the tunneling $t_{L/R}$ through the $SU(N)$ quantum impurity. Right panel: Fermi distribution functions of the left (hot) and right (cold) leads at temperatures $T_{L/R}$ and chemical potential $\mu_{L/R}$. The thermo-voltage $\Delta V = |\mu_R - \mu_L|/e$ is applied to achieve the steady state with zero net current across the impurity. Left (red)/right (blue) arrows show directions of thermo- and electric- currents. Resonance Kondo peak of width T_K in density of states is shown by the green color.

1.3.2 Nonlinear theory of thermoelectrics with a $SU(N)$ Kondo impurity

Efficient control of heat flow through nano-sized quantum devices (such as single-electron transistors, quantum diodes etc.) is one of the important directions of modern quantum technologies and quantum computing. For example, a quantum dot (one of promising realizations of the single electron transistor) is typically sandwiched between two external reservoirs and therefore accessible through quantum tunneling effects. Besides, at very low temperatures, electrons carry both charge and heat serving as a driving force of thermoelectric phenomena. Assuming that the source and the drain are biased by an external electric potential and characterized by two different temperatures (as shown in Fig 1.7), both scattering and interactions in the quantum dot develop at out-of-equilibrium conditions. The involvement of strong electron-electron interactions and resonance scattering demands a non-perturbative treatment of the problem. In this facet, we construct a new approach to the quantum thermoelectric transport through nano-devices based on non-equilibrium many-body theory. This approach allowed for a mapping of a model of quantum-spin-impurity onto a Fermi system which scatters and interacts at the quantum dot position.

In summary, we investigate thermoelectric transport through a $SU(N)$ quantum impurity in the Kondo regime. The strong coupling fixed point theory is described by the local Fermi-liquid paradigm. Using Keldysh technique we analyze the electric current through the quantum impurity at both finite bias voltage and finite temperature drop across it. The theory of a steady state at zero-current provides a complete description of the Seebeck effect. The Peltier coefficient is defined as the ratio of heat current to the charge current at isothermal condition. We find pronounced non-linear effects in temperature drop at low temperatures. We illustrate the significance of the non-linearities for enhancement of thermopower and Peltier coefficient by two examples of $SU(4)$ symmetric regimes characterized by a filling factor m : i) particle-hole symmetric at $m=2$ and ii) particle-hole non-symmetric at $m=1$. We analyse the effects of potential scattering and coupling asymmetry on the transport coefficients. We discuss connections between the theory and transport

experiments with coupled quantum dots and carbon nanotubes.

One of the central result of this work is the expression of the charge current of a $SU(N)$ Kondo impurity upto cubic response in applied bias ΔV and temperature gradient ΔT . For $T_K^{SU(N)}$ being the Kondo temperature and $G_0(N)$ the unitary conductance, the charge current $I_c(N, m)$ of a $SU(N)$ Kondo impurity with m electrons is

$$\begin{aligned} \mathcal{J}(N, m) &\equiv \frac{I_c(N, m)}{G_0(N)T_K^{SU(N)}} \\ &= \mathcal{L}_1^1 \Delta \bar{V} + \mathcal{L}_2^1 \Delta \bar{T} + \mathcal{L}_1^2 \Delta \bar{V}^2 + \mathcal{L}_2^2 \Delta \bar{T}^2 + \mathcal{L}_{12}^{11} \Delta \bar{V} \Delta \bar{T} + \dots \end{aligned} \quad (1.7)$$

Where the over-line symbol represents that the given quantity is normalized with the corresponding Kondo temperature such as $\bar{T} \equiv T/T_K^{SU(N)}$ and similarly the others. The transport coefficients in Eq. (1.7) are then expressed as a function of the intrinsic parameters of the $SU(N)$ Kondo impurity,

$$\begin{aligned} \mathcal{L}_1^1 &= \left[\sin^2 \left(\frac{\pi m}{N} \right) + \frac{1}{3} \frac{N+1}{N-1} \cos \left(\frac{2\pi m}{N} \right) (\pi \bar{T})^2 \right], \\ \mathcal{L}_2^1 &= -\frac{\pi^2}{3} \bar{T} \sin \left(\frac{2\pi m}{N} \right), \quad \mathcal{L}_1^2 = \frac{1}{2} \mathcal{C} \sin \left(\frac{2\pi m}{N} \right), \\ \mathcal{L}_2^2 &= -\frac{\pi^2}{6} \sin \left(\frac{2\pi m}{N} \right), \\ \mathcal{L}_{12}^{11} &= -\frac{\pi^2}{3} \bar{T} \left[\frac{\mathcal{C}(N-2) - N-1}{N-1} \cos \left(\frac{2\pi m}{N} \right) + 2\mathcal{C}\mathcal{A} \sin \left(\frac{2\pi m}{N} \right) \right], \end{aligned} \quad (1.8)$$

and similarly the higher order coefficients. In Eq. (1.8), the symbol $\mathcal{C} \equiv \cos 2\theta$ with $\theta \in (0, \pi/2)$ stands for the junction asymmetry and the parameter \mathcal{A} is defined as

$$\mathcal{A} \equiv \frac{N-2}{N-1} \frac{\Gamma(1/N) \tan(\pi/N)}{\sqrt{\pi} \Gamma(\frac{1}{2} + \frac{1}{N})} \cot \left[\frac{m\pi}{N} \right]. \quad (1.9)$$

1.3.3 Nonequilibrium transport through the two-stage, two-channel Kondo effect

A multi-orbital quantum impurity with effective spin $S > 1/2$ connected to several reservoirs of conduction electrons can lead to a Kondo effect exhibiting multi-stage screening. In a prototypical nano-scale device consisting of a $S=1$ quantum impurity connected to two conducting reservoirs, the first-stage screening process constitutes an under-screened Kondo effect where the impurity spin is effectively reduced from $S=1$ to $S=1/2$. Subsequently, second-stage screening leads to complete screening of the impurity spin and the formation of a spin singlet. Due to this two-stage screening mechanism, transport coefficients such as the differential conductance exhibit a non-monotonic dependence on external magnetic field, applied source-drain voltage and temperature. Theoretically understanding the equilibrium and non-equilibrium properties of the strong-coupling regime resulting from this two-stage screening mechanism has been an open problem for more than two decades, because, in contrast to standard impurity models such as the Kondo model or the single-impurity Anderson model, not one but two non-trivial phase shifts are involved.

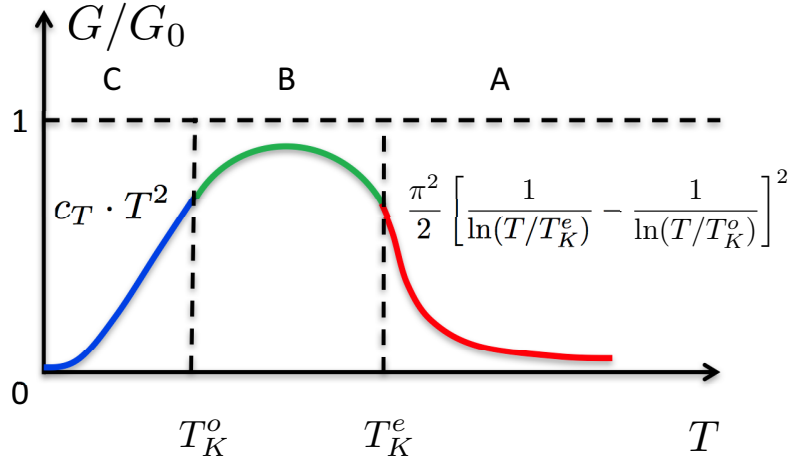


Figure 1.8: Schematic representation of the non-monotonic behavior of the differential conductance G/G_0 ($G_0 = 2e^2/h$ is the conductance quantum) as a function of temperature resulting from a two-stage Kondo effect. There are three characteristic regimes: (A) weak, (B) intermediate and (C) strong coupling. In the weak coupling (A)-regime the screening is absent and the transport coefficients are fully described by the perturbation theory. In the intermediate regime (B), the Kondo impurity is partially screened (see the first stage at the top panel); the residual interaction of electrons with the under-screened spin is antiferromagnetic. The description of the FL transport coefficients in the strong coupling regime (C) at the second stage of the screening is the central result of our work.

We consider a quantum dot with $\mathcal{K} \geq 2$ orbital levels occupied by two electrons connected to two electric terminals. The generic model is given by a multi-level Anderson Hamiltonian. The weak-coupling theory at the particle-hole symmetric point is governed by a two-channel $S=1$ Kondo model characterized by intrinsic channels asymmetry. These channels are leveled as “even (e)” and “odd (o)” characterized by the respective Kondo temperatures $T_K^{e/o}$. Based on the conformal field theory approach we derived an effective Hamiltonian at a strong-coupling fixed point. The Hamiltonian capturing the low-energy physics of a two-stage Kondo screening represents the quantum impurity by a two-color local Fermi-liquid. Using non-equilibrium (Keldysh) perturbation theory around the strong-coupling fixed point we analyse the transport properties of the model at finite temperature (T), Zeeman magnetic field (B) and source-drain voltage (eV) applied across the quantum dot. We compute the Fermi-liquid transport constants and discuss different universality classes associated with emergent symmetries. The key result of this work is the non-monotonicity of the conductance in two-stage, two-channel Kondo effect as demonstrated in Fig 1.8. While we illustrate the general theory of two resonance scattering channels by the two-stage Kondo problem, the developed formalism is applicable for a broad class of models describing quantum transport through nano-structures and behavior of strongly correlated electronic systems. In addition, it is straightforward to extend the presented ideas for generic Anderson-type models away from the PH symmetric point and generalize it for the $SU(N)$ Kondo impurity in multi-stage setup.

1.3.4 Full counting statistics of the two-stage Kondo effect

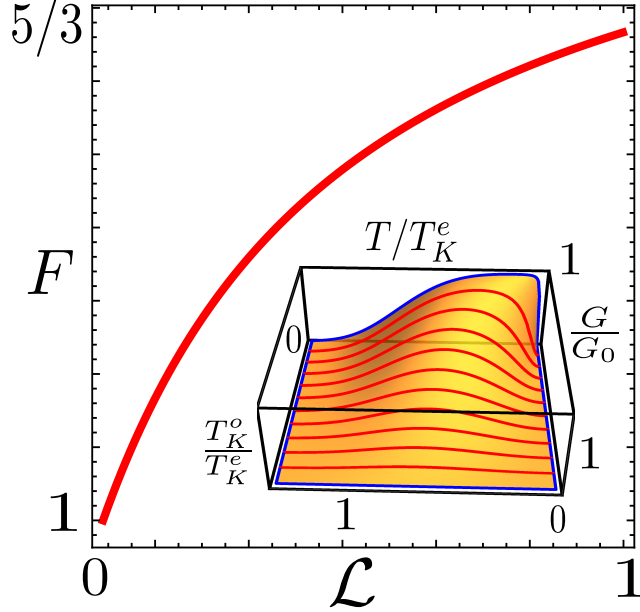


Figure 1.9: The evolution of Fano factor (F) as a function of channel asymmetry parameter (\mathcal{L}) for a generic two-stage Kondo effect. Inset: The non-monotonic conductance behavior, the major hallmark of multi-stage Kondo paradigm.

The method of full counting statistics (FCS) furnishes an elegant way to scrutinize an *arbitrary* (n -th) order cumulant of current through a nanodevices. The probabilistic interpretation of charge transport is at the core of FCS theory. The primary object of FCS is the moment generating function (MGF) for the probability distribution function (PDF) of transferred charges within a given time interval. The moments of PDF of order $n \geq 2$ characterize the current fluctuations. The FCS scheme permits in this way a transparent study of the quantum transport in various nanostructures. Various seminal works [93–97] paved the way to access the associated FCS in single channel spin-1/2 Kondo effects. As we already anticipated that the transport properties of two-stage Kondo effects are in strikingly contrast with the single channel case, the development of FCS for multi-stage, multi-channel Kondo paradigm seems to be a serious challenge. In this facet, we developed a theoretical framework which extends the method of FCS from conventional single channel Kondo screening schemes to multi-channel Kondo paradigm. The developed idea of FCS has been demonstrated considering an example of two-stage Kondo (2SK) model. We analyzed the charge transferred statistics in the strong-coupling regime of a 2SK model using non-equilibrium Keldysh formulation. One of the central result of this work is the prediction of bounded value of Fano factor (F), $1 \leq F \leq 5/3$ in 2SK model, which confirmed the cross-over regimes (from Poissonian to super-Poissonian) of charge transferred statistics in 2SK effect as shown in Fig. 1.9. An innovative way of measuring transport properties of 2SK effect, by the independent measurements of charge current and its noise, has been proposed.

1.4 Outline of this Thesis

In chapter 2 we present our calculation for the power production of a heat engine in the strong-coupling regime of a $SU(N)$ Kondo impurity, and show that it is bounded from below by zero and upper bound is strictly set by the filling factor and reference temperature. The chapter 3 is devoted to the development of the non-equilibrium theory of thermoelectric transport through a $SU(N)$ Kondo impurity. Two reciprocal measure of thermoelectrics namely, the Seebeck coefficient and Peltier coefficients are calculated in $SU(N)$ Kondo regime and the strong dependence of nonlinearity and junction asymmetry on the thermoelectric transport coefficients are explored. In addition, the mysterious experimental thermo-voltage offset observed with the $SU(2)$ Kondo correlated QD has been explained as an effect associated with nonlinearity. In chapter 4 we present a local FL theory for the quantum transport through the multi-stage, multi-channel Kondo effect and demonstrate the formalism for prototypical two-stage Kondo effect relevant to the spin-1 QD tunnel coupled to the two external reservoirs. In the last chapter of this thesis, we develop a theoretical framework which extends the method of full counting statistics from conventional single channel Kondo screening schemes to multi-channel Kondo paradigm. The developed idea of full counting statistics has been demonstrated considering an example of two-stage Kondo effect. We did our best to make each chapter self contained and independent from each other. Therefore, if you are interested in reading this thesis, you can start from any chapter you like.

Chapter 2

Thermoelectrics with a $SU(N)$ Kondo impurity

This chapter explores the thermoelectric power output of a heat engine in $SU(N)$ Kondo regime. Some parts of this chapter have been previously published as:

D. B. Karki and Mikhail N. Kiselev,

Effects of strong electron interactions and resonance scattering on power output of nano-devices, [arXiv:1906.00724](https://arxiv.org/abs/1906.00724).

2.1 Background

Greatly enhanced thermoelectric response of nano scale systems over conventional bulk materials has revived further the field of thermoelectricity [54–56]. Rapid development of nanotechnology has fueled several exciting thermoelectric experiments on nano materials and their theoretical formulation [57] to fulfill the urgent demand of energy harvesters for quantum technologies. The charge quantization in quantum devices [58] furnishes a controllable comprehension of underlying transport processes. Consequently, spectacular thermoelectric measurement of prototypical nano scale systems such as quantum dots (QDs), carbon nano-tubes (CNTs), quantum point contacts (QPCs), etc has been reported over the past years [54, 59]. In such a small systems the electron interactions are ubiquitous. Equivalently, strong Coulomb interaction is at the cornerstone of nano devices. The resonance scattering often combine with strong electron interaction resulting the system to posses very peculiar functionality [60, 61]. Therefore unified description of resonance scattering and strong electrons interaction at the nano scale have remained a challenging task for modern quantum technologies.

In the past years several perseverance have been devoted for the consistent description of thermoelectricity in QD based heat engines [57]. Efficiency and power production of a heat engine are the two connected fundamental ingredients of thermoelectric production [98–101]. Reversible engine, though Carnot efficient, are not of any practical applications since they do not produce finite

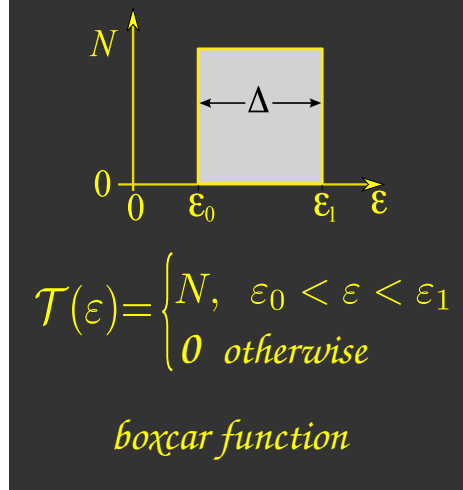


Figure 2.1: The boxcar transmission function $\mathcal{T}(\varepsilon)$ producing the maximum power output suggested in Ref [90]. The number of conduction modes is represented by N .

power [98]. Consequently the search for quantum thermoelectric devices with maximum attainable output power maintaining good efficiency have remained one of the active and demanding field of research in mesoscopic physics [57, 101]. Even though unveiling the universal upper bound of output power in nano devices looks like a serious challenge, certain attempts of this facet has been reported recently [90, 91, 102] by Whitney. These fundamental discoveries, for the first time, have shown that the quantum mechanics sets an upper bound on the power output of the non-interacting systems. Based on the non-linear scattering theory, the maximum power production of two-terminal nano devices established by Whitney [90] can be cast into the compact form

$$P_{\max}^0 \leq \frac{N}{h} A_0 \pi^2 \Delta T^2, \quad (2.1)$$

with the constant $A_0 \simeq 0.0321$, N is the number of transverse modes participating in the transport, h is the Planck's constant and ΔT is the applied temperature gradient. The equality in Eq. (2.1) is satisfied when the transmission is a boxcar function as shown in Fig. 2.1. Furthermore, according to the Whitney's formula Eq. (2.1), the power output grows linearly with numbers of conduction mode N . Therefore the setup with $N \gg 1$ would be highly advantageous for the better thermoelectric performance of a nano device. Since most of the thermoelectric devices are limited to the setup with $N \sim 1$ [90], Whitney further suggested to use many properly engineered quantum systems in parallel to increase N . In the experimental side, only about 50% of quantum upper bound of power output has been recently observed in one dimensional nano wire [92].

In addition to greatly contributing towards the better understanding of nano scale thermoelectricity, Whitney's prediction has open diverse valid avenues for further research, both theoretical and experimental. On one hand, examinations of how universal is this bound P_{\max}^0 in the presence of strong electron interactions are of earnest interest [91]. On the other hand, the intense search of better energy harvesters for quantum technologies demands properly addressing the fundamental question "can one deigned a operating nano devices in the interacting regime with similar upper bound as in non-interacting case P_{\max}^0 ?" In addition, how to experimentally achieve the setup with

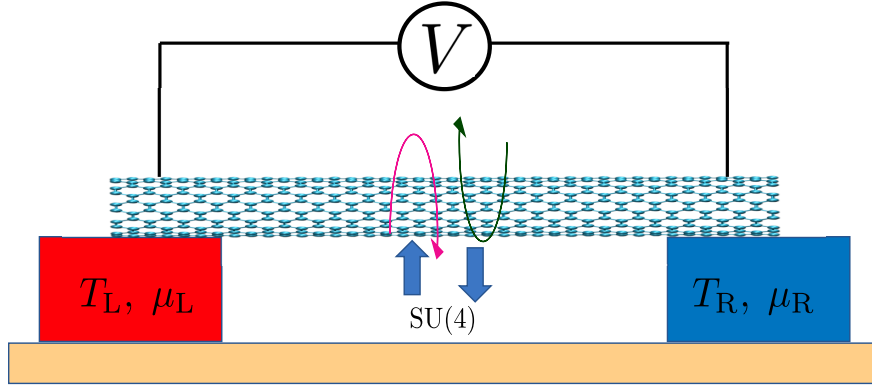


Figure 2.2: An example of $SU(N=4)$ Kondo correlated heat engine where a CNT is connected between two fermionic reservoirs, the hot (red) and the cold (blue). Voltage bias ΔV and temperature gradient $\Delta T = T_L - T_R$ is applied across the CNT quantum dot. The doubly degenerate orbital degree of freedom in CNT combines with spin degeneracy so as to form a Kondo effect with $SU(4)$ symmetry group.

$N \gg 1$ to increase the total power output of a nano device made up of a single quantum system is also the active field of research in mesoscopic physics.

In this chapter, we investigate the influences of strong electron interactions and resonance scattering on the output power of a generic nano device and discuss it in relation to the Whitney's formula. The strong electron correlation at the nano scale often results in dramatic transport properties. The most prominent example of low energy phenomena resulting from the strong interaction is the Kondo effect. Therefore, we chose a heat engine in Kondo correlated regime to reveal how the interactions modify the non-interacting upper bound of power production. As anticipated in chapter 1, the emergent particle-hole (PH) symmetry of conventional $SU(2)$ Kondo effects results in vanishingly small thermopower. Due to this difficulty associated with $SU(2)$ Kondo effect, we consider the paradigmatic $SU(N)$ Kondo regime. We proceed with the local Fermi-Liquid based calculation of power production in thermoelectric heat engine mediated by strongly coupled $SU(N)$ Kondo impurity. We concentrate our discussion mainly on the experimentally studied beyond half-filled $SU(4)$ Kondo effects. In addition, we examine power output with some proposed realizations of $SU(N)$ Kondo variants such as $SU(N=3, 6, 12)$.

The paradigmatic Kondo screening phenomena [7] play the central role in enhancing nano scale thermoelectricity by the formation of the quasi particle resonances at the Fermi level [32]. Recent experimental progress [33–38] has revived further the realm of transport measurements in Kondo correlated nano scale systems. The low temperature Kondo regime (the strong-coupling regime), emerges from the complete screening of spin of the localized impurity, is completely described by a local Fermi-Liquid (FL) theory [20]. Consequently, electrons (particles) and holes picture manifests itself in the quasi-particle description of thermoelectric transport. Being protected by particle-hole (PH) symmetry the conventional spin 1/2, $SU(2)$ Kondo impurity offers vanishingly small power output [1, 65]. This trouble is circumvented elegantly by uplifting the degeneracy of quantum impurity keeping the integer occupancy. These properties are exploited in beyond half-filled $SU(N)$ Kondo effects. In addition, these $SU(N)$ quantum impurity with integer

occupancy $m=1, 2 \dots N-1$, could provide much higher Kondo temperature over conventional SU(2) Kondo systems.

While the transport characteristics of conventional SU(2) Kondo effects has long been investigated [32, 103–105], the exotic SU(N) quantum impurities are of current interests. The authors of Ref. [81] have proposed two different realizations of SU(3) Kondo effect in QDs, namely, triple QDs with three and four edge states of the quantum Hall effects. Proposal and numerical demonstration of the SU(3) Kondo effect in spin less triple QDs have been also reported in recent years [82]. The paradigmatic SU(4) Kondo physics has been experimentally realized in CNTs [35, 68–70], double QDs [73] and single-electron transistor [74]. These studied were supplemented by different analytical and numerical approaches [75–78, 80]. In addition, several perseverance has been devoted in the cold atomic realization of SU($2l+1$), l being the orbital quantum number, Kondo physics [85, 87]. These perseverances have paid much attention towards the particular SU(3) Kondo effects [85]. Very recently, proposal of SU(6) Kondo effects in cold atom has been also reported [88] in addition to its earlier proposal using three-orbital Anderson impurity [83]. Utilizing the spin, orbital and valley degeneracy one can expects Kondo effects even with much higher symmetry group, for example, the SU(12) Kondo effects in CNTs [84]. Given that, the investigation of power production in SU(N) quantum impurity is very fundamental open problem of the field.

2.2 Thermoelectric transport

The charge and the heat currents in the linear response theory are connected by the Onsagar relations [63, 64],

$$\begin{pmatrix} I_c \\ I_h \end{pmatrix} = \begin{pmatrix} L_{11} & L_{12} \\ L_{21} & L_{22} \end{pmatrix} \begin{pmatrix} \Delta V \\ \Delta T \end{pmatrix}, \quad (2.2)$$

with the setting $e=\hbar=1$. The Onsagar transport coefficients L_{ij} in Eq. (2.2) provide all the thermoelectric measurements of interests in linear response regime [65]. As we anticipated earlier, the low energy transport via fully screened SU(N) Kondo impurity is completely described by a local FL theory [20]. Therefore the coefficients L_{ij} are characterized by the single particle T-matrix $T_r(\varepsilon)$ of FL quasi-particles [29, 65]. Such connection is governed by defining the transport integrals $\mathcal{I}_n(T)$ ($n=0, 1$ and 2) in terms of the imaginary part of the T-matrix [29],

$$\mathcal{I}_n(T) = \sum_r \int_{-\infty}^{\infty} \frac{d\varepsilon}{2\pi} \varepsilon^n \left[-\frac{\partial f(\varepsilon)}{\partial \varepsilon} \right] \text{Im} [-\pi \nu T_r(\varepsilon)]. \quad (2.3)$$

Here $f(\varepsilon) = [1 + \exp(\varepsilon/T)]^{-1}$ is the equilibrium Fermi-distribution function of the reference reservoir. The orbital index is represented by the symbol r which takes all possible values starting from 1 to N . Density of states per species for the one-dimensional channel ν and the Fermi-velocity v_F are related as $\nu = 1/2\pi v_F$. Then the transport coefficients characterizing the charge current are expressed in terms of the transport integrals, namely, $L_{11} = \mathcal{I}_0$ and $L_{12} = -\mathcal{I}_1/T$ [66]. This reduces our task to find the expression of the T-matrix of Eq. (2.3) using a local FL-paradigm. Suppose $\mathcal{G}_{kr}^0(\varepsilon)$ and $\mathcal{G}_{kr}(\varepsilon)$ represents the bare and full Green's functions (GFs) of FL quasi-particles. In addition, we consider the k -independence of the T-matrix which is valid for the local interactions

considered in this work. Then the diagonal part of a single-particle T-matrix $T_{\mathbf{r}}(\varepsilon)$ is defined by the Dyson equation [29],

$$\mathcal{G}_{k_{\mathbf{r}},k'_{\mathbf{r}'}}(\varepsilon) = \delta_{\mathbf{r}\mathbf{r}'}\mathcal{G}_{k_{\mathbf{r}}}^0(\varepsilon) + \mathcal{G}_{k_{\mathbf{r}}}^0(\varepsilon)T_{\mathbf{r}\mathbf{r}'}(\varepsilon)\mathcal{G}_{k'_{\mathbf{r}'}}^0(\varepsilon). \quad (2.4)$$

Where $\delta_{\mathbf{r}\mathbf{r}'}$ is the Kronecker delta function. Fourier transformation of Eq. (2.4) into the position space reads

$$\begin{aligned} \mathcal{G}_{\mathbf{r}\mathbf{r}'}(x, x'; \varepsilon) &= \frac{1}{L} \sum_{kk'} e^{i(kx-k'x')} [\delta_{\mathbf{r}\mathbf{r}'}\mathcal{G}_{k_{\mathbf{r}}}^0(\varepsilon) + \mathcal{G}_{k_{\mathbf{r}}}^0(\varepsilon)T_{\mathbf{r}\mathbf{r}'}(\varepsilon)\mathcal{G}_{k'_{\mathbf{r}'}}^0(\varepsilon)] \\ &= \frac{1}{iv_{\mathbf{F}}} e^{i(\varepsilon/v_{\mathbf{F}}+k_{\mathbf{F}})(x-x')} [\theta(x-x')\delta_{\mathbf{r}\mathbf{r}'} - \theta(x)\theta(-x')2i\pi\nu T_{\mathbf{r}\mathbf{r}'}(\varepsilon)]. \end{aligned} \quad (2.5)$$

In Eq. (2.5), $\theta(x)$ is the step function and we used the linearized dispersion relation: $\xi_k=v_{\mathbf{F}}(k-k_{\mathbf{F}})$. From Eq. (2.5) it is seen that the element $\mathbb{S}_{\mathbf{r}\mathbf{r}'}(\varepsilon) \equiv [\delta_{\mathbf{r}\mathbf{r}'} - 2i\pi\nu T_{\mathbf{r}\mathbf{r}'}(\varepsilon)]$ must be a 2×2 unitary matrix to ensure the particle conservation. To compute the T-matrix accounting for the scattering effects in FL, we can safely assume that the low-energy electron cannot flip spin due to the scattering events. This argument ensures that the scattering matrix $\mathbb{S}_{\mathbf{r}\mathbf{r}'}(\varepsilon)$ should be diagonal. Then the elastic part (scattering) of T-matrix $T_{\mathbf{r}\mathbf{r}'}^{\text{el}}(\varepsilon)$ is defined as

$$T_{\mathbf{r}\mathbf{r}'}^{\text{el}}(\varepsilon) = \frac{i\delta_{\mathbf{r}\mathbf{r}'}}{2\pi\nu} [\mathbb{S}_{\mathbf{r}\mathbf{r}'}^{\text{el}}(\varepsilon) - 1] \implies -\pi\nu T_{\mathbf{r}\mathbf{r}'}^{\text{el}}(\varepsilon) = \frac{1}{2i} [e^{2i\delta_{\mathbf{r}}^{\text{el}}(\varepsilon)} - 1]. \quad (2.6)$$

In Eq. (2.6) we express the elastic part of the scattering matrix $\mathbb{S}_{\mathbf{r}}^{\text{el}}(\varepsilon)$ in terms of the scattering phase shift $\delta_{\mathbf{r}}^{\text{el}}(\varepsilon)$ such that $\mathbb{S}_{\mathbf{r}}^{\text{el}}(\varepsilon)=e^{2i\delta_{\mathbf{r}}^{\text{el}}(\varepsilon)}$. For the $\text{SU}(N)$ Kondo impurity the equilibrium phase shift accounting for the scattering effects and Hartree contribution to the self energy is written in terms of the Nozieres FL parameters [20, 106]

$$\delta_{\sigma}^{\text{el}}(\varepsilon) = \delta_0 + \alpha_1\varepsilon + \alpha_2 \left[\varepsilon^2 - \frac{(\pi T)^2}{3} \right]. \quad (2.7)$$

This general expression for the elastic phase shift is applicable to the strong-coupling regime of $\text{SU}(N)$ Kondo impurity with upto $m=N-1$ electrons. The phase shift corresponds to the perfect transmission is given by [106]

$$\delta_0 = m\pi/N. \quad (2.8)$$

The first and second generations of FL coefficients, α_1 and α_2 respectively, are related to the Kondo temperature of the system [1]. For the sake of simplicity, we define the Kondo temperature such that

$$T_{\text{K}}^{\text{SU}(N)}=1/\alpha_1, \quad (2.9)$$

where the N -dependence in the FL parameters is implicit. The exact relation between α_1 and α_2 is given by the Bethe-ansatz solution [107]:

$$\frac{\alpha_2}{\alpha_1^2} = \frac{N-2}{N-1} \frac{\Gamma(1/N) \tan(\pi/N)}{\sqrt{\pi}\Gamma(\frac{1}{2} + \frac{1}{N})} \cot \left[\frac{m\pi}{N} \right]. \quad (2.10)$$

Where $\Gamma(x)$ is the Euler's gamma-function. Note that for the half-filled systems, $m=N/2$ (with even N), the second generation of the FL-coefficients gets nullified. The T-matrix accounting for

the inelastic effects (leaving aside the corresponding Hartree contributions) associated with the quasi-particle interaction in FL theory is given by [20, 24]

$$T_r^{\text{in}}(\varepsilon) = \frac{N-1}{2i\pi\nu} [\varepsilon^2 + (\pi T)^2] \phi^2. \quad (2.11)$$

Here ϕ is the FL-coefficient representing the interaction effects originated from the four-fermions interaction, the interactions beyond four fermions is neglected for the description of low-energy transport processes. It has been proved that the coefficient ϕ is related with α_1 such that $\alpha_1 = (N-1)\phi$ [107]. In addition, the inelastic part of the T-matrix Eq. (2.11) is an even function of energy, that is the inelastic transmission function is symmetric with respect to the energy. Such a perfect symmetry tends to nullify the thermoelectric response as will be clear in the following section. Therefore in the linear response level of calculations the thermoelectric coefficient \mathcal{I}_1 is solely governed by the scattering effects associated with the FL quasi-particles plus the Hartree contribution to the self energy. The T-matrix accounting for the scattering and interactions in the FL is expressed as [29],

$$T_r^{\text{tot}}(\varepsilon) \equiv T_r(\varepsilon) = T_r^{\text{el}}(\varepsilon) + e^{2i\delta_0} T_r^{\text{in}}(\varepsilon). \quad (2.12)$$

Note that the expression of $-\pi\nu\text{Im}T_r(\varepsilon)$ in Eq. (2.12) contains the cosine factor $\cos 2\delta_0$ coupled with the inelastic part Eq. (2.11). Interestingly, the factor $\cos 2\delta_0$ dramatically modifies some transport behaviors. For the quarter filled SU(N) impurity such that, $m/N = 1/4$ or $3/4$, the imaginary part of second term in Eq. (2.12) vanishes. Such systems are merely described by the phase shift expression Eq. (2.7). This ideal situation corresponds to the Kondo effects in CNT (see Fig 2.2), where the SU(4) Kondo effect comes into play with $m=1, 2$ or 3 . While the $m = 2$, SU(4) systems have poor thermoelectric performance due to the emergent PH symmetry, the systems of SU(4) impurity beyond half-filled regime are the ideal test-bed for the study of transport behavior. Use of T-matrix expression given in Eq. (2.12) into the transport integrals Eq. (2.3) followed by the Taylor series expansion up to the second order in energy yields,

$$\begin{aligned} \mathcal{I}_n(T) = & \frac{G_0^{\text{SU}(N)}}{4T} \int_{-\infty}^{\infty} d\varepsilon \frac{\varepsilon^n}{\cosh^2(\varepsilon/2T)} \left[\sin^2 \delta_0 \right. \\ & + \frac{(\pi T)^2}{2N-2} \left(\alpha_1^2 \cos 2\delta_0 - \frac{2N-2}{3} \alpha_2 \sin 2\delta_0 \right) \\ & \left. + \alpha_1 \sin 2\delta_0 \varepsilon + \left(\frac{2N-1}{2N-2} \alpha_1^2 \cos 2\delta_0 + \alpha_2 \sin 2\delta_0 \right) \varepsilon^2 \right]. \end{aligned} \quad (2.13)$$

Here $G_0^{\text{SU}(N)} = N/2\pi$ is the unitary conductance of SU(N) system. All the fundamental measures of thermoelectricity in the linear response level of calculation can be extracted from Eq. (2.13).

2.3 Output power of a heat engine in SU(N) Kondo regime

Though all the fundamental measure of thermoelectricity can be extracted from Eq. (2.13), here we shall focus only on the power production. Any thermoelectric devices would need finite output power $P = -I_c \Delta V$ for the successful operation. In addition, the output power can be optimized

2.3. Output power of a heat engine in SU(N) Kondo regime

with respect to the applied bias for the given temperature drop across the impurity. For instance, from Eq. (2.2) we express the charge current as

$$I_c = L_{11}\Delta V + L_{12}\Delta T. \quad (2.14)$$

Maximizing the output power $P = -I_c\Delta V$ using Eq. (2.14) we get

$$P_{\max} = \frac{1}{4} \frac{L_{12}^2}{L_{11}} \Delta T^2. \quad (2.15)$$

Using the transport integral provided by the Eq. (2.13) we cast the maximum power produced by the SU(N) Kondo correlated nano devices into the form

$$P_{\max}^{\text{Kondo}} = \frac{N\pi^2}{h} A_0^{\text{Kondo}} \Delta T^2. \quad (2.16)$$

In Eq. (2.16) we retained the constant h for its transparency. The numerical factor A_0^{Kondo} is the characteristics of the SU(N) Kondo impurity which is given by

$$A_0^{\text{Kondo}} = \frac{1}{36} \frac{\sin^2\left(\frac{2\pi m}{N}\right) \left(\frac{\pi T}{T_K^{\text{SU}(N)}}\right)^2}{\sin^2\left(\frac{\pi m}{N}\right) + \frac{1}{3} \left(\frac{\pi T}{T_K^{\text{SU}(N)}}\right)^2 \frac{N+1}{N-1} \cos\left(\frac{2\pi m}{N}\right)}. \quad (2.17)$$

Note that the maximum power production Eq. (2.16) of thermoelectric devices with SU(N) Kondo impurity has analogous form with the corresponding Whitney's formula. While in non-interacting system studied in Ref. [90] the factor A_0 is purely a constant number, the SU(N) Kondo impurity offers its generalization that also depends on the system properties. Note that, for the low energy description of problem considered in this work, we set the reference temperature $T \leq T_K^{\text{SU}(N)}/7$ to fulfill all the assumptions made in deriving the non-interacting upper bound in Ref. [90].

From Eq. (2.17) it is clearly seen that the PH symmetry of the problem, mainly the half filling $m/N=1/2$ situation, tends to nullify the power production. Furthermore, the SU(N) Kondo impurity with large N and small m are again not preferable for the propose of achieving appreciable power production. Another very interesting limit of Eq. (2.17) is the quarter filled situation, $m/N=1/4$. In this limit the power production is universal, irrespective of m and N as far as their ratio is one quarter,

$$A_0^{\text{Kondo}} \Big|_{m/N=1/4} = \frac{\pi^2}{18} \left(\frac{T}{T_K^{\text{SU}(4)}}\right)^2. \quad (2.18)$$

The factor A_0^{Kondo} characterizing the power output per degeneracy of SU(N) Kondo effect is plotted (in the unit of A_0) in Fig. 2.3 as a function of occupancy m for fixed N (upper panel) and in reverse order (lower panel). As seen from the Fig 2.3, about 50% of quantum upper bound of output power can be generated with SU(N) Kondo effects. Though the power output per degeneracy is half of the quantum bound, SU(N) Kondo effect offers the possibility of $N \gg 1$ and results in a giant output power. Note that, mere increase of N fixing m to the small value would not be at all advantageous to increase the power output (see lower panel of Fig. 2.3). This generic feature of strong interplay between the Kondo resonance and filling factor is in striking contrast to the non-interacting system studied in Ref. [90]. In addition, the optimal value for the coefficient A_0^{Kondo} given in Eq. (2.17) is achieve with the filling factor $m/N=1/6$ relevant to the existing proposed realizations [83, 84, 88].

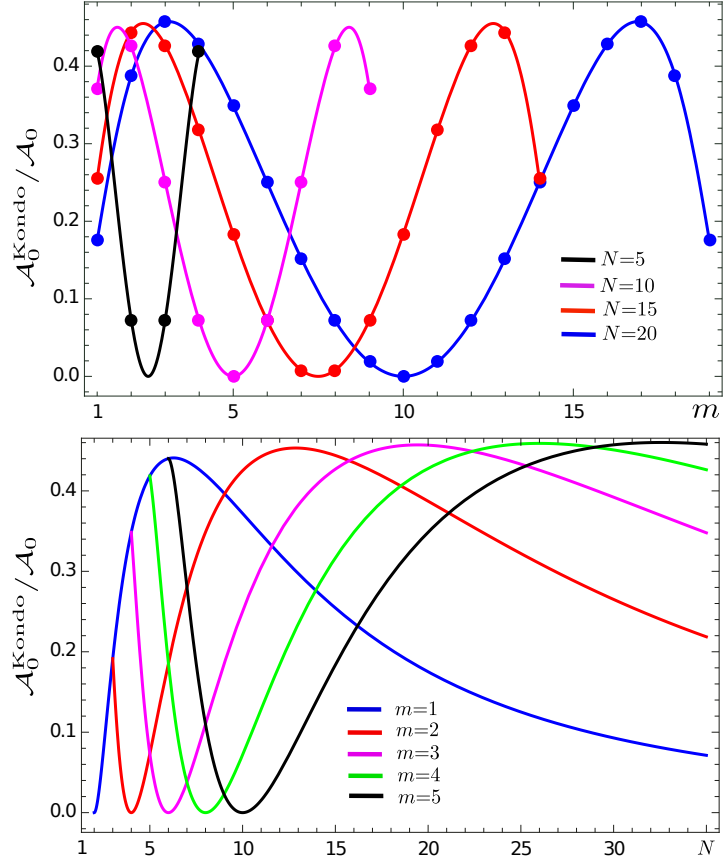


Figure 2.3: Upper panel: The output power of $SU(N)$ Kondo impurity per degeneracy in the unit of corresponding quantum upper bound as a function of occupancy m for fixed N . Lower panel: The decay of output power of $SU(N)$ Kondo impurity with N for given m . For both plots the reference temperature has been fixed to $T = T_K^{\text{SU}(N)} / 7$.

2.4 Summary

We develop a Fermi-liquid based approach to investigate the output power of a generic nano device in the presence of strong electron interactions and resonance scattering. The developed formalism is employed to reveal the output power of a $SU(N)$ Kondo impurity which offers the nontrivial occupations away from the half-filling. The strong interplay of Kondo resonance and the filling-factors in a beyond half-filled Kondo effect is found to be a key of enhancing output power which results in about 50% of quantum upper bound of power output. We provide an efficient experimental way of increasing the total power of a nano device by uplifting the degeneracy factor N as well as the electrons occupation m fulfilling the ratio $m/N \sim 1/6$ since the power production grows linearly with N . Our suggestion is in contrast to the previous suggestion [90] of using many properly engineered quantum systems in parallel to increase the factor N .

Chapter 3

Nonequilibrium theory of thermoelectrics of a $SU(N)$ Kondo impurity

In this chapter we explore the nonlinear thermoelectric associated with the $SU(N)$ Kondo effect. The content of this chapter was previously published as:

1. **D. B. Karki** and Mikhail N. Kiselev,
Nonlinear Seebeck effect of $SU(N)$ Kondo impurity,
[Phys. Rev. B **100**, 125426 \(2019\)](#) .
2. **D. B. Karki** and Mikhail N. Kiselev,
Thermoelectric transport through a $SU(N)$ Kondo impurity,
[Phys. Rev. B **96**, 121403 \(2017\)](#) [**Rapid Communication**].

3.1 Background

Recent progress in understanding of thermoelectric phenomena on the nanoscale stimulated both new experiments [33–35] and development of new theoretical approaches to this problem [57]. One of the fundamental properties of the quantum transport through nano-sized objects (quantum dots (QD), carbon nanotubes (CNT), quantum point contacts (QPC) etc) is associated with the charge quantization [59]. It offers a very efficient tool for the quantum manipulation of the single-electron devices being building blocks for quantum information processing. The universality of the heat flows in the quantum regime, scales of the quantum interference effects and limits of the tunability are the central questions of the new emergent field of the quantum heat transport [32–35, 108, 109]. Besides, the effects of strong electron correlations and resonance scattering become very pronounced at low temperatures and can be measured with high controllability (e.g. external electric and magnetic fields, geometry, temperature etc) of the semiconductor nano-devices. Therefore, investigation

of the quantum effects and influence of strong correlations and resonance scattering on the heat transport (both experimentally and theoretically) is one of the cornerstones of quantum electronics.

A generic nano device consists of a quantum impurity with intrinsic spin S which is tunnel coupled to two electron reservoirs, the source and the drain. The low energy transport processes are then controlled by the strong interaction between localized spin S and itinerant electrons in the reservoirs. The spin $S=1/2$ impurity interacting with a single orbital channel of conduction electrons forms a fully screened ground state resulting in quasi-particle resonances at the Fermi level. This paradigmatic screening phenomenon is termed as Kondo effect [7] which is characterized by a low energy scale T_K , the Kondo temperature. As follows from the Fermi-liquid (FL) theory, the thermoelectric power (Seebeck coefficient) of bulk metals is directly proportional to the temperature T and inversely proportional to the Fermi energy ε_F [62]. The resonance scattering on a quantum impurity, however, dramatically enhances this effect due to the emergence of new quasi-particle resonances at the Fermi level described by the Kondo effect [10, 20, 22]. The contribution to the Seebeck coefficient then scales as T/T_K [10, 62] with $T_K \ll \varepsilon_F$. Therefore, the many-body Kondo resonance at the Fermi level opens an effective path towards the enhancement of thermoelectric production at the nano scale level [32]. Recent experiments [33–38] have further expanded the scope of transport measurements in Kondo correlated nano scale systems. Most of these studies have been focused on the transport measurement of the conventional spin $S=1/2$ Kondo impurity described by the $SU(2)$ symmetry group. However, the conventional $SU(2)$ Kondo effects, being protected by particle-hole (PH) symmetry, offer vanishingly small thermoelectric conversion [65]. To achieve appreciable thermopower, the occupation factor of the quantum impurity should be integer, while the PH symmetry should be lifted [1]. The $SU(N)$ Kondo model with integer occupancy m offers the possibility of avoiding half-filled regime so as to achieve the enhanced thermoelectric production over the conventional $SU(2)$ Kondo correlated systems [1, 4, 67].

The orbital degeneracy of the quantum impurity combines with the true spin symmetry to form the Kondo effect described by higher symmetry group $SU(N)$. Here the occupancy factor m takes all possible values starting from 1 to $N-1$. The paradigmatic $SU(4)$ Kondo physics has been experimentally studied in CNTs [35, 68–72], double QDs [73] and single-atom transistor [74]. Various theoretical works [75–80] have contributed towards the better understanding of $SU(4)$ Kondo physics over the past years. In addition, exciting proposals has been put forth for the experimental realization of different variants of $SU(N)$ Kondo systems. Possible realization of $SU(3)$ Kondo effects using triple QDs with three and four edge states of the quantum Hall effects was suggested in Ref. [81], which been verified recently using numerical renormalization group study [82]. The proposals for the solid-state realization of $SU(6)$ [83] and $SU(12)$ [84] Kondo effects have likewise attracted considerable attentions both theoretically and experimentally. Beside obtaining the solid-state realization of these exotic $SU(N)$ Kondo effects, an increasing effort has been put in their cold atomic realization [85–88]. These studies on $SU(N)$ Kondo effects have been concentrated solely on the charge current measurements. However, thermoelectric characterization in a generic nano device usually involves two reciprocal processes, namely, the Seebeck effects and the Peltier effects. To the best of our knowledge very few studies have tried to uncover the thermoelectric measurements of Kondo effects described by higher symmetry group, such as the

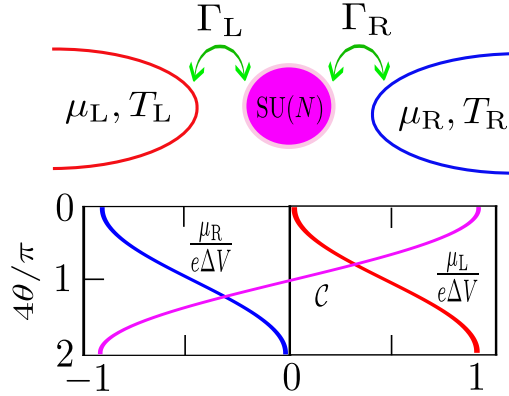


Figure 3.1: Upper panel: A $SU(N)$ quantum impurity is sandwiched between two conducting reservoirs. The left (red) and right (blue) reservoirs are in thermal equilibrium, separately, at temperature T_L and T_R respectively. The tunneling-matrix elements from the impurity to the left/right reservoirs are characterized by $t_L = t \cos \theta$ and $t_R = t \sin \theta$ with $\theta \in (0, \pi/2)$. The particular case of $\theta = \pi/4$ reproduces a perfectly symmetric setup. The intrinsic total local level width associated with the tunneling is given by $\Gamma_{L/R} = \pi \rho_{\text{res}} |t_{L/R}|^2$, ρ_{res} being the density of states of the reservoirs. Lower panel: The asymmetry of the tunneling junction is accounted for by introducing a parameter $C \equiv (\Gamma_L - \Gamma_R)/(\Gamma_L + \Gamma_R) = \cos 2\theta$. The magenta line represents the variation of asymmetry parameter C with respect to the asymmetry angle θ . For the sake of simplicity we choose the Fermi level in such a way that the chemical potentials of the left and right reservoirs take some specific values $\mu_{L/R} = \pm \frac{e\Delta V}{2}(1 \mp C)$. This choice of chemical potentials amounts to greatly simplify the calculation of charge and heat current through a strongly coupled Kondo impurity (see text for detail). These chemical potentials are represented by the red and blue curve respectively.

Seebeck effects with a $SU(4)$ Kondo effects have been studied in Ref. [67].

In this chapter we develop a fully-fledged theory for the thermoelectric transport through a $SU(N)$ Kondo model in the strong coupling regime $T \ll T_K$. The approach is based on real time out-of-equilibrium Keldysh calculations. We use the local Fermi-liquid paradigm for constructing a perturbative expansion for the electric current around the strong coupling fixed point of the model. We illustrate the thermoelectric properties of the experimentally studied $SU(N)$ Kondo effects described by the $SU(2)$ and $SU(4)$ model. We present the discussion of thermoelectrics of the theoretically proposed $SU(N)$ Kondo variants such as the $SU(3)$, $SU(6)$ and $SU(12)$ Kondo effects. We compute the thermoelectric power for arbitrary temperature drop between the electron reservoirs and discuss the significance of non-linear effects in temperature drop. The local Fermi-liquid theory of thermoelectricity presented in this chapter also accounts for the effects associated with the coupling asymmetry which could provide important informations about the underlying many body effects [106].

3.2 Theoretical formulation

We consider a quantum impurity tunnel coupled to two conducting reservoirs as shown in Fig. 3.1. The impurity possess N -fold degeneracy by combining the spin and other degrees of freedom, such as the orbital degeneracy. In addition, there are N -species (orbitals) of electrons in both left (L) and right (R) reservoirs. The rotation of the reservoir's electrons is then described by the $SU(N)$ transformation. Therefore, to describe our system we start form $SU(N)$ impurity Anderson model [21, 110],

$$H = \sum_{k,r} \varepsilon_k \left[c_{L,kr}^\dagger c_{L,kr} + c_{R,kr}^\dagger c_{R,kr} \right] + H_{\text{imp}} + H_{\text{tun}}. \quad (3.1)$$

Here we introduce the notation “r” to represent the orbital index that takes all possible values starting from 1 to N . The operator $c_{\gamma,kr}^\dagger$ creates an electron with momentum k in r-th orbital of the γ ($=L, R$) reservoir. The energy of conduction electrons ε_k is measured with respect to the chemical potential μ . The second term of Eq. (3.1) represents the Hamiltonian of the impurity possessing N degenerate flavors with single energy level ε_d . Then we write the impurity Hamiltonian as

$$H_{\text{imp}} = \varepsilon_d \sum_r d_r^\dagger d_r + U \sum_{r < r'} d_r^\dagger d_r d_{r'}^\dagger d_{r'}, \quad (3.2)$$

where d_r^\dagger is the electron creation operator of the impurity and U represents the charging energy which is assumed to be the largest energy scale of the model. The tunneling processes from the impurity to the reservoirs are accounted for by the very last term of the Eq. (3.1),

$$H_{\text{tun}} = \sum_{k,r} \left(t_L c_{L,kr}^\dagger + t_R c_{R,kr}^\dagger \right) d_r + \text{H.c.}, \quad (3.3)$$

We explicitly assume the tunneling asymmetry by assigning the tunneling-matrix elements t_γ such that $t_L = t \cos \theta$ and $t_R = t \sin \theta$ with $\theta \in (0, \pi/2)$. Then the intrinsic total local level width associated with the tunneling is given by $\Gamma_\gamma = \pi \rho_{\text{res}} |t_\gamma|^2$ with ρ_{res} being the density of states of the reservoirs. For the sake of clarity, we introduce the parameter $\mathcal{C} \equiv (\Gamma_L - \Gamma_R)/(\Gamma_L + \Gamma_R) = \cos 2\theta$ to characterize the asymmetry of the tunneling junction. This asymmetry further appears in the Glazman-Raikh rotation [111] of Eq. (3.1) in the basis of reservoirs electrons

$$\begin{pmatrix} b_{kr} \\ a_{kr} \end{pmatrix} = \begin{pmatrix} \cos \theta & \sin \theta \\ \sin \theta & -\cos \theta \end{pmatrix} \begin{pmatrix} c_{L,kr} \\ c_{R,kr} \end{pmatrix}. \quad (3.4)$$

Note that the transformation Eq. (3.4) effectively decouples the operators a_{kr} from the impurity degrees of freedom. Here we consider the general case of having arbitrary number of electrons $m=1, 2, \dots, N-1$ in the impurity. Therefore, the specific choice of impurity level $\varepsilon_d = U(1 - m - m/N)$ provides the fundamental representation with $\sum_r d_r^\dagger d_r \equiv \sum_r n_r = m$. We then perform the Schrieffer-Wolff transformation [112] followed by the rotation Eq. (3.4) of the Hamiltonian Eq. (3.1) to project out the charge states, which results in

$$\mathcal{H} = \sum_{k,r} \varepsilon_k \left(a_{kr}^\dagger a_{kr} + b_{kr}^\dagger b_{kr} \right) + H_{\text{Kondo}}. \quad (3.5)$$

The Kondo Hamiltonian is expressed in terms of anti-ferromagnetic coupling J_K between the impurity spin \vec{S} and the spin operator of reservoir electrons placed at the origin \vec{T} as [106, 107, 113]

$$H_{\text{Kondo}} = J_K \vec{S} \cdot \vec{T}, \quad J_K = \frac{t^2}{U} \frac{N^2}{m(N-m)}. \quad (3.6)$$

The N^2-1 traceless components of impurity spin $\mathcal{S}^i (i=1, 2 \dots N^2-1)$ are given by

$$\mathcal{S}^{r,r'} = d_r^\dagger d_{r'} - m/N \delta_{r,r'}, \quad (3.7)$$

with the constraint $r, r' \neq N, N'$. Likewise, the spin operator of reservoir electrons placed at the origin is expressed as $\vec{T} = \sum_{kk', rr'} b_{kr}^\dagger \Lambda_{rr'}^i b_{k'r'}$, Λ^i being the $N \times N$ generators of $SU(N)$ group. Note that \mathcal{S}^i are $\frac{N!}{m!(N-m)!} \times \frac{N!}{m!(N-m)!}$ matrices acting on states with m electrons.

The ground state of spin $S=1/2$ $SU(N)$ impurity considered in this work is characterized by the complete screening of impurity spin which results in the formation of Kondo singlet. The low-energy regime of fully-screened Kondo effect is consistently describe by FL theory [20, 24, 114]. Applying the standard point-splitting procedure [1, 24, 106, 107] to the Hamiltonian Eq. (3.6) results in the low energy FL Hamiltonian of $SU(N)$ Kondo impurity,

$$\begin{aligned} \mathcal{H}_0 &= \nu \sum_r \int_\varepsilon \varepsilon \left[a_{\varepsilon r}^\dagger a_{\varepsilon r} + b_{\varepsilon r}^\dagger b_{\varepsilon r} \right], \\ \mathcal{H}_{\text{el}} &= - \sum_r \int_{\varepsilon_{1-2}} \left[\frac{\alpha_1}{2\pi} (\varepsilon_1 + \varepsilon_2) + \frac{\alpha_2}{4\pi} (\varepsilon_1 + \varepsilon_2)^2 \right] b_{\varepsilon_1 r}^\dagger b_{\varepsilon_2 r}, \\ \mathcal{H}_{\text{int}} &= \sum_{r < r'} \int_{\varepsilon_{1-4}} \left[\frac{\phi_1}{\pi\nu} + \frac{\phi_2}{4\pi\nu} \sum_{j=1}^4 \varepsilon_j \right] : b_{\varepsilon_1 r}^\dagger b_{\varepsilon_2 r} b_{\varepsilon_3 r'}^\dagger b_{\varepsilon_4 r'} :. \end{aligned} \quad (3.8)$$

The PH symmetric version of Eq. (3.8) was originally proposed by Nozieres [20] which is commonly known as Nozieres FL theory. In Eq. (3.8) the density of states per species for a one dimensional channel is represented by the symbol ν . The scattering (elastic) effects in the FL are accounted for by the Hamiltonian \mathcal{H}_{el} , where α_1 and α_2 are the first and second generations of Nozieres FL coefficients respectively. The four fermions term represents the interaction part of the Hamiltonian \mathcal{H}_{int} which is expressed in terms of FL parameters ϕ_1 and ϕ_2 . These FL parameters are related to the associated Kondo temperature of the corresponding $SU(N)$ impurity. The FL parameters characterizing the scattering effects are connected to those of interaction effects by the relation, $\alpha_1 = (N-1)\phi_1$ and $\alpha_2 = (N-1)\phi_2/4$. In addition the Bethe ansatz provides further link between α_1 and α_2 [106, 107],

$$\frac{\alpha_2}{\alpha_1^2} = \frac{N-2}{N-1} \frac{\Gamma(1/N) \tan(\pi/N)}{\sqrt{\pi} \Gamma(\frac{1}{2} + \frac{1}{N})} \cot \left[\frac{m\pi}{N} \right]. \quad (3.9)$$

Where $\Gamma(x)$ is the Euler's gamma-function. Therefore the low energy FL Hamiltonian Eq. (3.8) is completely specified by only one FL parameter, say α_1 . We make a connection of α_1 with the corresponding Kondo temperature such that $T_K^{\text{SU}(N)} = 1/\alpha_1$, the N -dependence in FL parameters is implicit. Note that we have retained upto the four fermions term in Eq. (3.8), the higher-order terms produce the current correction beyond cubic order in applied bias and temperature gradient which is beyond the scope of present work.

It is then a straightforward procedure to proceed with the calculation of physical observables by treating the scattering Hamiltonian \mathcal{H}_{el} and interaction part \mathcal{H}_{int} perturbatively. However, in the spirit of Nozieres phenomenology, the scattering effects are fully described by an energy-dependent phase shift $\delta_{\text{r}}^{\text{el}}(\varepsilon)$. The Kondo singlet acts as the scatterer for the incoming electrons from the leads. The outgoing and incoming electrons then differ from each other by the elastic phase shift $\delta_{\text{r}}^{\text{el}}(\varepsilon)$. The Nozieres FL parameters α_1 and α_2 are the first and second order coefficients in the Taylor-series expansion of elastic phase shift. While the scattering effects are easily accounted for by the elastic phase-shift, the perturbative treatment of \mathcal{H}_{int} produces complicated self-energy diagrams. This complication can be simplified a bit by including the Hartree contribution of self-energy in the elastic phase shift [106, 107]. Then the Taylor expansion of phase shift reads

$$\begin{aligned} \delta_{\text{r}}(\varepsilon) = & \delta_0 + \alpha_1\varepsilon + \alpha_2\varepsilon^2 - \sum_{\text{r}' \neq \text{r}} \left[\phi_1 \int_{-\infty}^{\infty} d\varepsilon \delta n_{\text{r}'}(\varepsilon) \right. \\ & \left. + \frac{\phi_2}{2} \left(\varepsilon \int_{-\infty}^{\infty} d\varepsilon \delta n_{\text{r}'}(\varepsilon) + \int_{-\infty}^{\infty} d\varepsilon \varepsilon \delta n_{\text{r}'}(\varepsilon) \right) \right]. \end{aligned} \quad (3.10)$$

Here the zero-energy phase shift of $\text{SU}(N)$ Kondo impurity with m electrons is

$$\delta_0 = \frac{m\pi}{N}. \quad (3.11)$$

In Eq. (3.10) we used the definition of the actual FL quasi-particle distribution relative to the Fermi-energy ε_{F} as $\delta n_{\text{r}}(\varepsilon) \equiv n_{\text{r}}(\varepsilon) - \Theta(\varepsilon_{\text{F}} - \varepsilon) = \langle b_{\text{kr}}^{\dagger} b_{\text{kr}} \rangle - \Theta(\varepsilon_{\text{F}} - \varepsilon)$, Θ being the step function. Using Eq. (3.4) we expressed the average $\langle b_{\text{kr}}^{\dagger} b_{\text{kr}} \rangle$ in terms of the equilibrium Fermi-distribution functions $f_{\gamma}(\varepsilon) = \left[1 + \exp\left(\frac{\varepsilon - \mu_{\gamma}}{T_{\gamma}}\right) \right]^{-1}$ of the left and right reservoirs; $\langle b_{\text{kr}}^{\dagger} b_{\text{kr}} \rangle = \cos^2 \theta f_{\text{L}} + \sin^2 \theta f_{\text{R}}$. In the following discussion, we chose the Fermi-level such that

$$\int_{-\infty}^{\infty} d\varepsilon \delta n_{\text{r}}(\varepsilon) = 0. \quad (3.12)$$

This equation is always satisfied as far as the condition $\mu_{\text{L}} \cos^2 \theta + \mu_{\text{R}} \sin^2 \theta = \varepsilon_{\text{F}}$ is full-filled. We then made the following specification for the chemical potentials of the reservoirs,

$$\mu_{\text{L}} = e\Delta V \sin^2 \theta \equiv \frac{e\Delta V}{2} (1 - \mathcal{C}), \quad (3.13)$$

$$\mu_{\text{R}} = -e\Delta V \cos^2 \theta \equiv -\frac{e\Delta V}{2} (1 + \mathcal{C}), \quad (3.14)$$

to make $\varepsilon_{\text{F}}=0$. It is also noted that the details related to the choice of the temperatures in the reservoirs do not affect the necessary condition to satisfy the Eq. (3.12). To be more general, we do not yet impose any restriction on the choice of T_{L} and T_{R} . Using these specification of chemical potentials and temperatures of the reservoirs, the straightforward integration of phase shift expression Eq. (3.10) leads

$$\delta_{\text{r}}(\varepsilon) = \delta_0 + \alpha_1\varepsilon + \alpha_2(\varepsilon^2 - \mathcal{A}). \quad (3.15)$$

To obtain Eq. (3.15) we used the FL identity $\alpha_2 = (N-1)\phi_2/4$ and the new definition,

$$\mathcal{A} = \frac{1}{6} \left[(\pi T_{\text{L}})^2 (1 + \mathcal{C}) + (\pi T_{\text{R}})^2 (1 - \mathcal{C}) + \frac{3}{2} (1 - \mathcal{C}^2) (e\Delta V)^2 \right].$$

In the following section the scattering effects in addition to the Hartree contribution to the self energy correction will be accounted for by the Eq. (3.15). To obtain the self energy correction beyond Hartree contribution we will be treating the interaction Hamiltonian \mathcal{H}_{int} perturbatively with the small parameters $(e\Delta V, T_L, T_R) / T_K^{\text{SU}(N)}$.

3.3 Current Calculation

Using the basis of scattering states that includes the elastic effects and Hartree term, we cast the charge current expression into the form [2, 106]

$$\hat{I} = \frac{e}{2h\nu} \sum_{\mathbf{r}} \sin 2\theta \left[a_{\mathbf{r}}^{\dagger}(x) b_{\mathbf{r}}(x) - a_{\mathbf{r}}^{\dagger}(-x) \mathbb{S} b_{\mathbf{r}}(-x) + \text{H.c.} \right], \quad (3.16)$$

for $b_{\mathbf{r}}(x) = \sum_k b_{k\mathbf{r}} e^{ikx}$ and $\mathbb{S} b_{\mathbf{r}}(x) = \sum_k \mathbb{S}_k b_{k\mathbf{r}} e^{ikx}$. To write Eq. (3.16) we have also omitted the terms of the form $\sum_{\mathbf{r}, \mathbf{p}=\pm} \mathbf{p} a_{\mathbf{r}}^{\dagger}(\mathbf{p}x) a_{\mathbf{r}}(\mathbf{p}x)$ since they do not produce finite contribution to the mean current. In addition, we expressed $N \times N$ scattering matrix \mathbb{S}_k in terms of phase shift expression Eq. (3.15) such that $\mathbb{S}_k = \exp[2i\delta_{\mathbf{r}}(\varepsilon)]$. To compute the various observables from Eq. (3.16) we need the following averages directly obtained from the Glazman-Raikh rotation

$$\begin{pmatrix} \langle b_k^{\dagger} b_k \rangle \\ \langle a_k^{\dagger} a_k \rangle \\ \langle b_k^{\dagger} a_k \rangle \end{pmatrix} = \begin{pmatrix} \cos^2 \theta & \sin^2 \theta & 0 \\ \sin^2 \theta & \cos^2 \theta & 0 \\ \frac{\sin 2\theta}{2} & -\frac{\sin 2\theta}{2} & 0 \end{pmatrix} \begin{pmatrix} f_L(\varepsilon_k) \\ f_R(\varepsilon_k) \\ 0 \end{pmatrix}. \quad (3.17)$$

The average of Eq. (3.16) provides the elastic current (including the corresponding Hartree contribution) which have the compact form analogous to the Landauer-Büttiker expression

$$I_{\text{el}} = \frac{e}{h} \sum_{\mathbf{r}} \int_{-\infty}^{\infty} d\varepsilon \mathcal{T}_{\mathbf{r}}(\varepsilon) [f_L(\varepsilon) - f_R(\varepsilon)]. \quad (3.18)$$

The effective transmission coefficient $\mathcal{T}_{\mathbf{r}}(\varepsilon)$ is completely specified by the phase shift expression Eq. (3.15); $\mathcal{T}_{\mathbf{r}}(\varepsilon) \equiv (1 - \mathcal{C}^2) \sin^2[\delta_{\mathbf{r}}(\varepsilon)]$. To write $\mathcal{T}_{\mathbf{r}}(\varepsilon)$ into more tractable form, we perform its second-order Taylor expansion in energy,

$$\mathcal{T}_{\mathbf{r}}(\varepsilon) = (1 - \mathcal{C}^2) \left[\mathcal{T}_0 - \alpha_2 \mathcal{A} \sin 2\delta_0 + \alpha_1 \sin 2\delta_0 \varepsilon + (\alpha_1^2 \cos 2\delta_0 + \alpha_2 \sin 2\delta_0) \varepsilon^2 \right]. \quad (3.19)$$

Here $\mathcal{T}_0 = \sin^2 \delta_0$ is the zero energy transmission coefficient. Then it is trivial procedure to compute the elastic current by plugging in Eq. (3.19) into Eq. (3.18). The exact computation of Eq. (3.18) follows from the consideration of following integrals [2, 3],

$$\mathcal{K}_n = \int_{-\infty}^{\infty} \varepsilon^n [f_L(\varepsilon) - f_R(\varepsilon)] d\varepsilon, \quad n = 0, 1 \text{ and } 2. \quad (3.20)$$

Conventional way of calculating the integrals in Eq. (3.20) consists of Sommerfeld expansion of $\Delta f(\varepsilon) \equiv f_L(\varepsilon) - f_R(\varepsilon)$ in the small parameters $\Delta T \equiv T_L - T_R$ and ΔV . However, the Fourier-transform technique allows us to compute Eq. (3.20) exactly. Fourier transforming the function $\Delta f(\varepsilon)$ into real time reads,

$$\Delta f(t) = \frac{1}{2\pi} \int_{-\infty}^{\infty} d\varepsilon e^{-i\varepsilon t} \Delta f(\varepsilon). \quad (3.21)$$

Performing the n-times partial differentiation of Eq. (3.21) and taking the limit $t \rightarrow 0$ we get,

$$\frac{2\pi}{(-i)^n} \left. \frac{\partial^n \Delta f(t)}{\partial t^n} \right|_{t=0} = \int_{-\infty}^{\infty} d\varepsilon \varepsilon^n \Delta f(\varepsilon). \quad (3.22)$$

Fourier transformation of the Fermi distributions of left and right reservoirs allows us to write

$$\Delta f(t) = \frac{i}{2} \left[\frac{T_L e^{-i\mu_L t}}{\sinh(\pi T_L t)} - \frac{T_R e^{-i\mu_R t}}{\sinh(\pi T_R t)} \right]. \quad (3.23)$$

Plugging in Eq. (3.23) into Eq. (3.22) with the chemical potentials as specified in Eqs. (3.13) and (3.14) we obtain $\mathcal{K}_0 = e\Delta V$, $\mathcal{K}_1 = [(\pi T_L)^2 - (\pi T_R)^2 - 3\mathcal{C}(e\Delta V)^2] / 6$ and

$$\mathcal{K}_2 = \frac{e\Delta V}{3} \left[\frac{(e\Delta V)^2}{4} (1 + 3\mathcal{C}^2) + \frac{1 - \mathcal{C}}{2} (\pi T_L)^2 + \frac{1 + \mathcal{C}}{2} (\pi T_R)^2 \right].$$

For completeness we re-express the elastic current in terms of the integrals in Eq. (3.20) as

$$I_{\text{el}} = \frac{Ne(1 - \mathcal{C}^2)}{h} \left[(\mathcal{T}_0 - \alpha_2 \mathcal{A} \sin 2\delta_0) \mathcal{K}_0 + \alpha_1 \sin 2\delta_0 \mathcal{K}_1 + (\alpha_1^2 \cos 2\delta_0 + \alpha_2 \sin 2\delta_0) \mathcal{K}_2 \right]. \quad (3.24)$$

Now we turn to the discussion of inelastic effects leaving aside the Hartree contributions, which has been already accounted for by the phase shift expressed in Eq. (3.15). As we anticipated earlier, the perturbative treatment of \mathcal{H}_{int} imparts the interaction corrections to the charge current. This approach requires the expressions of non-interaction Green's functions (GFs) characterized by \mathcal{H}_0 . Making use of non-equilibrium calculations based on Keldysh approach [115], we obtained following four non-interaction GFs in Keldysh space

$$\begin{aligned} \mathcal{G}_{bb/aa}(k, \varepsilon) &= \frac{1}{\varepsilon - \varepsilon_k} \tau_z + i\pi \begin{pmatrix} F_{b/a} & F_{b/a+1} \\ F_{b/a-1} & F_{b/a} \end{pmatrix} \delta(\varepsilon - \varepsilon_k), \\ \mathcal{G}_{ba/ab}(k, \varepsilon) &= i\pi \begin{pmatrix} 1 & 1 \\ 1 & 1 \end{pmatrix} F_{ab} \delta(\varepsilon - \varepsilon_k). \end{aligned} \quad (3.25)$$

Here the parameters $F_{b/a}(\varepsilon)$ and $F_{ab}(\varepsilon_k)$ are expressed in terms of different populations; $F_b(\varepsilon_k) = 2\langle b_k^\dagger b_k \rangle - 1$, $F_a(\varepsilon_k) = 2\langle a_k^\dagger a_k \rangle - 1$ and $F_{ab} = 2\langle b_k^\dagger a_k \rangle$. The z-component of Pauli-matrix is represented by τ_z . However, in the flat-band limit only the off-diagonal parts of $\mathcal{G}_{bb}(k, \varepsilon)$, namely $\mathcal{G}_{bb}^{+-}(k, \varepsilon)$ and $\mathcal{G}_{bb}^{-+}(k, \varepsilon)$ produce the finite contribution to the charge current. The straightforward mathematical steps provide the following Fourier-transformed real-time GFs

$$\begin{aligned} \mathcal{G}_{bb}^{+-}(t) &= -\frac{\pi\nu}{2} \left[\frac{T_L(1 + \mathcal{C})e^{-i\mu_L t}}{\sinh(\pi T_L t)} + \frac{T_R(1 - \mathcal{C})e^{-i\mu_R t}}{\sinh(\pi T_R t)} \right], \\ \mathcal{G}_{ab/ba}(t) &= -\frac{\pi\nu}{2} \sqrt{1 - \mathcal{C}^2} \left[\frac{T_L e^{-i\mu_L t}}{\sinh(\pi T_L t)} - \frac{T_R e^{-i\mu_R t}}{\sinh(\pi T_R t)} \right]. \end{aligned} \quad (3.26)$$

The GFs $\mathcal{G}_{bb}^{+-}(t)$ and $\mathcal{G}_{bb}^{-+}(t)$ are connected by causality relations. In practice, the GFs expressed in Eqs. (3.25) and (3.26) are sufficient for the calculation of charge current. To calculate the inelastic correction to the charge current we then apply the perturbation theory using Keldysh formalism [115],

$$\delta I_{\text{in}} = \langle T_C \hat{I}(t) e^{-i \int dt' \mathcal{H}_{\text{int}}(t')} \rangle, \quad (3.27)$$

where C denotes the double-side $\eta=\pm$ Keldysh contour and T_C is corresponding time-ordering operator. We used the expression of charge current operator Eq. (3.16) and interaction Hamiltonian \mathcal{H}_{int} into Eq. (3.27) to obtain the interaction correction to the charge current

$$\delta I_{\text{in}} = \frac{N(N-1)}{h} e\pi (1-C^2) \cos 2\delta_0 \int_{-\infty}^{\infty} \frac{d\varepsilon}{2\pi} (\Sigma^{-+} - \Sigma^{+-})(\varepsilon) i\pi\nu \Delta f(\varepsilon). \quad (3.28)$$

To arrived from Eq. (3.27) to Eq. (3.28) we have already subtracted the diverging terms, which amounts to the renormalization of FL coefficients (see Ref. [106] for detail). The self-energies in Eq. (3.28) are expressed in real-time as

$$\Sigma^{\eta_1\eta_2}(t) = \left(\frac{\phi_1}{\pi\nu^2}\right)^2 \sum_{k_{1-3}} \left[\mathcal{G}_{bb}^{\eta_1\eta_2}(k_1, t) \mathcal{G}_{bb}^{\eta_2\eta_1}(k_2, -t) \mathcal{G}_{bb}^{\eta_1\eta_2}(k_3, t) \right]. \quad (3.29)$$

To compute the self-energies, now we specify the temperatures of the left and right reservoirs $T_{\text{R}}=T$ and $T_{\text{L}}=T+\Delta T$ with $\Delta T>0$. In practice one can numerically solve for the self-energy using the GFs of Eq. (3.26). However, it is manageable to find the analytical expression of the self energy difference to the first order in ΔT and second order in $e\Delta V$ which reads

$$(\Sigma^{-+} - \Sigma^{+-})(\varepsilon) = \frac{\phi_1^2}{i\pi\nu} \left[\frac{3}{4} (e\Delta V)^2 (1-C^2) + \varepsilon^2 + (\pi T)^2 + \frac{\Delta T}{T} (\pi T)^2 (1+C) \right]. \quad (3.30)$$

To arrive from Eq. (3.29) to Eq. (3.30) we came across the integral of the form,

$$\mathcal{Z}(a, T) = \int_{-\infty}^{\infty} \frac{e^{iat}}{\sinh^3(\pi T t)} dt. \quad (3.31)$$

The singularity of the integral in Eq. (3.31) is removed by shifting the time contour by $i\eta$, $\eta \rightarrow 0$ in the complex plane. We chose the rectangular contour enclosing the singularity at $t=0$ and use the Cauchy's residue theorem to arrive at the result,

$$\mathcal{Z}(a, T) = -i\pi \frac{a^2 + (\pi T)^2}{(\pi T)^2} \frac{1}{\exp(a/T) + 1}. \quad (3.32)$$

Since the self-energy difference Eq. (3.30) contains all possible terms up to the linear response, plugging it into Eq. (3.28) provides interaction correction up to the quadratic order in ΔT and ΔV . To make interaction contributions to the charge current more symmetrical with that of elastic effects, we write

$$\delta I_{\text{in}} = \frac{Ne(1-C^2)}{h} \frac{1}{2} \frac{1}{N-1} \cos 2\delta_0 \alpha_1^2 \left[\mathcal{K}_2 + \left(\frac{\Delta T}{T} (\pi T)^2 (1+C) + (\pi T)^2 \right) \mathcal{K}_0 \right]. \quad (3.33)$$

This equation correctly reproduces the interaction correction up to the quadratic response with the coefficients $\mathcal{K}_{0,2}$ given in Eq. (3.20). Using Eq. (3.24) and (3.33), the charge current is given by

$$I_c = I_{\text{el}} + \delta I_{\text{int}}. \quad (3.34)$$

Alternatively the charge current of a $\text{SU}(N)$ Kondo impurity is directly expressible in terms of effective transmission coefficient $\text{T}_r^{\text{eff}} \equiv \mathcal{T}_r(\varepsilon, T, \Delta V, \Delta T)$,

$$I_c = \frac{e}{h} \sum_r^N \int_{-\infty}^{\infty} d\varepsilon \text{T}_r^{\text{eff}} [f_{\text{L}}(\varepsilon) - f_{\text{R}}(\varepsilon)]. \quad (3.35)$$

The effective transmission coefficient can be directly read from the Eqs. (3.18) and (3.28), which for isothermal condition $\Delta T = 0$ is given by the relation

$$\begin{aligned} \left. \frac{T_r^{\text{eff}}(\varepsilon)}{1-\mathcal{C}^2} \right|_{\Delta T=0} &= \mathcal{T}_0 - \sin 2\delta_0 \alpha_2 \left[\frac{(\pi T)^2}{3} + \frac{(e\Delta V)^2}{4}(1-\mathcal{C}^2) \right] \\ &+ \sin 2\delta_0 \alpha_1 \varepsilon + (\cos 2\delta_0 \alpha_1^2 + \sin 2\delta_0 \alpha_2) \varepsilon^2 \\ &+ \frac{1}{2(N-1)} \cos 2\delta_0 \left[\varepsilon^2 + (\pi T)^2 + \frac{3}{4}(e\Delta V)^2(1-\mathcal{C}^2) \right] \alpha_1^2. \end{aligned} \quad (3.36)$$

The Peltier coefficient is defined as the ratio of heat current to the charge current at isothermal condition. Therefore, the effective transmission coefficient Eq. (3.36) plays a fundamental role for the characterization of the Peltier coefficient of a strongly coupled $SU(N)$ Kondo impurity as will be discussed in the following section. The thermoelectric characterization of a generic nano device usually involves two reciprocal processes, namely, the Seebeck effects and the Peltier effects [116, 117]. While the Seebeck effect quantifies the generation of the voltage driven by the temperature difference at zero charge current condition, the heating or cooling of a junction in the presence of finite charge current is accounted for by Peltier effect. Though the linear response measurements of these two effects are related by the Kelvin relation, the non-linearly drives them to behave quite differently. In the following section we discuss our results for the measure of Seebeck and Peltier effects in the strong-coupling regime of an asymmetrically coupled $SU(N)$ Kondo impurity.

3.4 Seebeck effects

The non-linear Seebeck effect is quantified by the Seebeck coefficient defined as the ratio of thermovoltage developed under the condition of zero charge current, $\Delta V_{\text{th}} \equiv \Delta V|_{I_c=0}$, to the applied temperature gradient [66, 118],

$$\mathcal{S} \equiv - \left. \frac{\Delta V_{\text{th}}}{T_L - T_R} \right|_{I_c=0}. \quad (3.37)$$

In fact, the Seebeck coefficient Eq. (3.37) contains additional information than the electrical and thermal conductance measurements [116]. While the electrical conductance depends merely on the density of states at the Fermi level, Seebeck coefficient reveals its slope [62]. In addition, the Seebeck coefficient provides the useful informations related to the average energy of charge carriers contributing to the transport processes [119]. We characterize the Seebeck coefficient of a $SU(N)$ Kondo impurity by defining the dimensionless form of charge current considering up to the quadratic responses in voltage bias and temperature gradient,

$$\mathcal{J}(N, m) \equiv \frac{I_c(N, m)}{G_0(N)T_K^{\text{SU}(N)}} = \mathcal{L}_1^1 \Delta \bar{V} + \mathcal{L}_2^1 \Delta \bar{T} + \mathcal{L}_1^2 \Delta \bar{V}^2 + \mathcal{L}_2^2 \Delta \bar{T}^2 + \mathcal{L}_{12}^{11} \Delta \bar{V} \Delta \bar{T}. \quad (3.38)$$

The maximum conductance of $SU(N)$ Kondo impurity in the presence of asymmetry is expressed by the relation $G_0(N) = (1 - \mathcal{C}^2) Ne^2/h$. From now we specify the electronic charge $e=-1$ and the convention $\Delta V > 0$ and $\Delta T > 0$. The quantities written in over-line letters represent that they are normalized with corresponding Kondo temperature, for instance, $\bar{T} \equiv T/T_K^{\text{SU}(N)}$ and similarly the

others. From Eq. (3.24) and (3.33) we obtained the transport coefficients \mathcal{L}_j^i and \mathcal{L}_{12}^{11} , $i, j = 1, 2$ for the SU(N) Kondo impurity,

$$\begin{aligned}\mathcal{L}_1^1 &= \left[\sin^2 \left(\frac{\pi m}{N} \right) + \frac{1}{3} \frac{N+1}{N-1} \cos \left(\frac{2\pi m}{N} \right) (\pi \bar{T})^2 \right], \\ \mathcal{L}_2^1 &= -\frac{\pi^2}{3} \bar{T} \sin \left(\frac{2\pi m}{N} \right), \quad \mathcal{L}_1^2 = \frac{1}{2} \mathcal{C} \sin \left(\frac{2\pi m}{N} \right), \\ \mathcal{L}_2^2 &= -\frac{\pi^2}{6} \sin \left(\frac{2\pi m}{N} \right), \\ \mathcal{L}_{12}^{11} &= -\frac{\pi^2}{3} \bar{T} \left[\mathcal{B} \cos \left(\frac{2\pi m}{N} \right) + 2\mathcal{C} \mathcal{A} \sin \left(\frac{2\pi m}{N} \right) \right].\end{aligned}\quad (3.39)$$

The coefficients \mathcal{A} , see Eq. (3.9), and \mathcal{B} are defined as

$$\mathcal{A} \equiv \alpha_2 / \alpha_1^2, \quad \mathcal{B} \equiv \frac{\mathcal{C}(N-2) - N - 1}{N-1}.\quad (3.40)$$

From Eq. (3.39) it is seen that the transport coefficients accounting for the linear and quadratic correction in temperature gradient are connected by the relation $\mathcal{L}_2^1 = 2\bar{T}\mathcal{L}_2^2$. It is apparent that, merely the asymmetry of the junction is responsible to have the quadratic correction in voltage bias. For half-filled SU(N) Kondo effects, we observe that $\mathcal{L}_2^1 = \mathcal{L}_1^2 = \mathcal{L}_2^2 = 0$, therefore, corresponding thermoelectric properties are governed by only two coefficients \mathcal{L}_1^1 and \mathcal{L}_{12}^{11} . This fact explains that the half-filled SU(N) Kondo impurity do not offers finite thermo-power even in quadratic-response level of calculations. Another important conclusion can be drawn from Eq. (3.39) is as follows; for the perfectly symmetrical quarter-filled SU(N) Kondo correlated systems, the combine effects of temperature gradient and voltage bias tend to vanish $\mathcal{L}_{12}^{11}|_{\mathcal{C}=0}(N, N/4)=0$. Furthermore, the coefficients characterizing the voltage response do not acquire the temperature correction. These facts should make the non-linear thermoelectric measurement of beyond half-filled SU(4) systems as a trivial procedure. To have more insights of the thermoelectric production in SU(N) Kondo systems, we solve the zero current condition of the Eq. (3.38) to get the thermo-voltage upto the quadratic terms in $\Delta\bar{T}$,

$$-\Delta\bar{V}_{\text{th}} = \mathcal{S}^{\text{LR}} \Delta\bar{T} + \delta\mathcal{S}(\Delta\bar{T})^2 + \mathcal{O}(\Delta\bar{T})^3.\quad (3.41)$$

The Seebeck coefficient \mathcal{S} as defined in Eq. (3.37) then takes the form,

$$\mathcal{S} = \mathcal{S}^{\text{LR}} + \delta\mathcal{S}\Delta\bar{T} + \mathcal{O}(\Delta\bar{T})^2.\quad (3.42)$$

Here \mathcal{S}^{LR} is the linear response Seebeck coefficient and its first order $\Delta\bar{T}$ correction is defined by $\delta\mathcal{S}$,

$$\mathcal{S}^{\text{LR}} \equiv \frac{\mathcal{L}_2^1}{\mathcal{L}_1^1},\quad (3.43)$$

$$\delta\mathcal{S} \equiv \left[\frac{\mathcal{L}_2^2}{\mathcal{L}_1^1} - \frac{\mathcal{L}_2^1 \mathcal{L}_{12}^{11}}{(\mathcal{L}_1^1)^2} + \frac{(\mathcal{L}_2^1)^2 \mathcal{L}_1^2}{(\mathcal{L}_1^1)^3} \right].\quad (3.44)$$

The transport coefficients defining the linear response Seebeck coefficient \mathcal{S}^{LR} are independent of asymmetry parameter \mathcal{C} . However, the first order correction $\delta\mathcal{S}$ bears the strong dependences on the asymmetry parameter via the transport coefficients \mathcal{L}_1^2 and \mathcal{L}_{12}^{11} . In addition, for the symmetrical

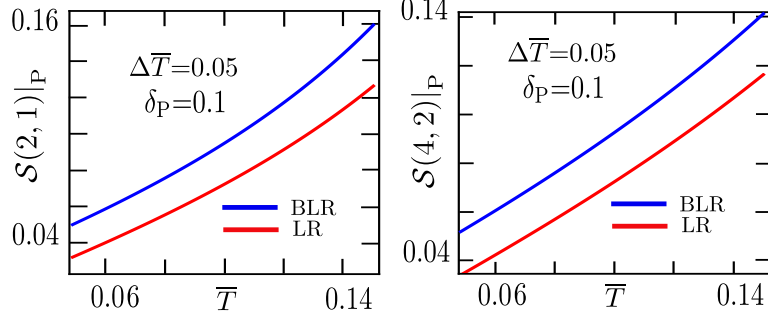


Figure 3.2: Linear (LR) and non linear (BLR) Seebeck coefficients with PH symmetric SU(2) and SU(4) Kondo effects for fixed value of the potential scattering δ_P .

setups, we use the Eq. (3.39) to express the correction factor $\delta\mathcal{S}$ entirely in terms of linear-response coefficients,

$$\delta\mathcal{S}|_{\mathcal{C}=0} = \frac{\mathcal{S}^{\text{LR}}}{\bar{T}} \left[\frac{\sin^2\left(\frac{\pi m}{N}\right)}{\mathcal{L}_1^1} - \frac{1}{2} \right]. \quad (3.45)$$

To study the effects of coupling asymmetry on the thermoelectric transport properties, we categorize the SU(N) Kondo impurity into two broad classes, namely, half-filled (PH symmetric) and beyond half-filled and discuss them separately.

3.4.1 PH symmetric SU(N) Kondo effects

As we anticipated earlier that for the half-filled SU(N) Kondo effects the transport coefficients satisfy the relation $\mathcal{L}_2^1 = \mathcal{L}_1^2 = \mathcal{L}_2^2 = 0$, therefore, corresponding thermoelectric properties are derived solely from the coefficients \mathcal{L}_1^1 and \mathcal{L}_{12}^{11} . The non-zero transport coefficients of PH symmetric SU(N) Kondo effects are summarized below,

$$\mathcal{L}_1^1(N, N/2) = \left[1 - \frac{1}{3} \frac{N+1}{N-1} (\pi\bar{T})^2 \right], \quad (3.46)$$

$$\mathcal{L}_{12}^{11}(N, N/2) = \frac{1}{3\bar{T}} \left[\frac{\mathcal{C}(N-2) - N - 1}{N-1} \right] (\pi\bar{T})^2. \quad (3.47)$$

While for the conventional SU(2) Kondo effects the parameter \mathcal{C} does not affect the cross-coefficient, the corresponding measurement in exotic SU($N > 2$) PH symmetric systems depends on the coupling asymmetry. However, the PH symmetry of the Kondo impurity realized in QDs is exact only if the dot is tuned to the middle of Coulomb valley [120]. This indicates the possibility of breaking the underlying PH symmetry. This weakly broken PH symmetry of Kondo correlated systems is accounted for by re-normalizing the reference phase shifts such that [121–123],

$$\delta_0 \rightarrow \tilde{\delta}_0 = \delta_0 + \delta_P, \quad \delta_0 \gg \delta_P. \quad (3.48)$$

This potential scattering provides the repulsive interactions which breaks the Kondo singlet and contributes to inelastic processes [124]. The first order transport coefficients in Eq. (3.39) for PH

symmetric Kondo correlated systems with an account of the potential scattering effects are then given by

$$\begin{aligned}\mathcal{L}_1^1(N, N/2)|_{\text{P}} &= \cos^2 \delta_{\text{P}} \left[1 - \frac{(\pi\bar{T})^2}{3} \frac{N+1}{N-1} \frac{2 \cos 2\delta_{\text{P}}}{1 + \cos 2\delta_{\text{P}}} \right], \\ \mathcal{L}_2^1(N, N/2)|_{\text{P}} &= \cos^2 \delta_{\text{P}} \left[\frac{(\pi\bar{T})^2}{3\bar{T}} \frac{2 \sin 2\delta_{\text{P}}}{1 + \cos 2\delta_{\text{P}}} \right].\end{aligned}\quad (3.49)$$

Eq. (3.49) allows us to compute the linear response Seebeck coefficient of PH symmetric $SU(N)$ Kondo effects with small potential scattering,

$$\mathcal{S}^{\text{LR}}(N, N/2)|_{\text{P}} = \frac{2}{3} \frac{1}{\bar{T}} \frac{(\pi\bar{T})^2}{1 - \frac{(\pi\bar{T})^2}{3} \frac{N+1}{N-1}} \delta_{\text{P}} + \mathcal{O}(\delta_{\text{P}})^3. \quad (3.50)$$

Note that due to the numerical factor $(N+1)/(N-1)$ in the denominator of Eq. (3.50), among PH symmetric generalizations of $SU(N)$ the $SU(2)$ Kondo correlated systems offer highest value of the linear response Seebeck coefficient in the presence of finite potential scattering. Plugging the Eq. (3.48) into the transport coefficients Eq. (3.39) and using them into Eq. (3.44), we get the first order correction to the Seebeck coefficient upto the linear order in δ_{P} ,

$$\delta\mathcal{S}(N, N/2)|_{\text{P}} = \frac{\pi^2}{3} \frac{1 - \frac{(\pi\bar{T})^2}{3} \left(\frac{N+1}{N-1} + 2\mathcal{B} \right)}{\left[1 - \frac{(\pi\bar{T})^2}{3} \frac{N+1}{N-1} \right]^2} \delta_{\text{P}} + \mathcal{O}(\delta_{\text{P}})^3. \quad (3.51)$$

For $SU(2)$ Kondo effects the correction Eq. (3.51) is independent of the asymmetry parameter due to the fact that $\mathcal{B}|_{N=2} = -3$. However for $SU(4)$ and other PH symmetric version of $SU(N)$, the first order correction to the Seebeck effect is weakly asymmetry dependent via the coefficient $\mathcal{B}(\mathcal{C})$. The linear and non linear Seebeck coefficient with PH symmetric $SU(2)$ and $SU(4)$ Kondo effects are shown in Fig. 3.2 with the choice of potential scattering term $\delta_{\text{P}} = 0.1$ and temperature gradient $\Delta\bar{T} = 0.05$. These significant enhancement of BLR Seebeck coefficients with respect to the corresponding LR contribution becomes more pronounced at relatively high reference temperature and large temperature drop across the junction.

3.4.2 Beyond half-filled $SU(N)$ Kondo effects

The Kondo correlated systems with $N > 2$ provide the realization of paradigmatic PH-asymmetric setups. First we start from the $SU(3)$ Kondo effects. The $SU(3)$ Kondo effect can occur either with single electron or two electrons. Since the $SU(3)$ Kondo systems do not offer the PH symmetric analog, they are expected to possess the good thermoelectric performance. The physics of $SU(3)$ Kondo effect with one and two electrons is related with each other by PH symmetry transformation. Therefore, we discuss the single electron $SU(3)$ Kondo systems, which will ultimately provide the corresponding informations of two electron case. For single electron $SU(3)$ Kondo effects the

transport coefficients in Eq. (3.39) are simplified as

$$\begin{aligned}\mathcal{L}_1^1(3,1) &= \frac{3}{4} \left[1 - \frac{4}{9}(\pi\bar{T})^2 \right], \quad \mathcal{L}_2^1(3,1) = -\frac{\pi^2\bar{T}}{2\sqrt{3}}, \\ \mathcal{L}_1^2(3,1) &= \mathcal{C} \frac{\sqrt{3}}{4}, \quad \mathcal{L}_2^2(3,1) = -\frac{\pi^2}{4\sqrt{3}}, \\ \mathcal{L}_{12}^{11}(3,1) &= -\frac{\pi^2}{3}\bar{T} \left[\frac{\mathcal{C}}{4} \left(1 - 2\sqrt{\frac{3}{\pi}} \frac{\Gamma[1/3]}{\Gamma[5/6]} \right) - 1 \right].\end{aligned}\quad (3.52)$$

Therefore while the cross coefficient $\mathcal{L}_{12}^{11}(3,1)$ is weakly asymmetry dependent, the coefficient $\mathcal{L}_1^2(3,1)$ is strongly influenced by \mathcal{C} . Since all the transport coefficients in Eq. (3.52) are non-zero, one can solve the zero-current equation to get the thermo-voltage developed in SU(3) Kondo effects. Now we turn to the discussion of SU(4) Kondo effects out of PH symmetric situation. The SU(4) Kondo effects can accommodate up to three electrons. While the two electron case suffers from the PH symmetry, the single and three electron SU(4) systems are regarded to have good thermoelectric performance. Furthermore, the single electron and three electron systems are related to each other by the PH symmetry transformation. Therefore we discuss in details the thermoelectric of single electron SU(4) Kondo effects. The corresponding transport coefficients are obtained as

$$\begin{aligned}\mathcal{L}_1^1(4,1) &= \frac{1}{2}, \quad \mathcal{L}_2^1(4,1) = -\frac{\pi^2}{3}\bar{T}, \quad \mathcal{L}_1^2(4,1) = \frac{\mathcal{C}}{2}, \\ \mathcal{L}_2^2(4,1) &= -\frac{\pi^2}{6}, \quad \mathcal{L}_{12}^{11}(4,1) = -\frac{4\pi^2\mathcal{C}\bar{T}}{9\sqrt{\pi}} \frac{\Gamma[1/4]}{\Gamma[3/4]}.\end{aligned}\quad (3.53)$$

The cross coefficient $\mathcal{L}_{12}^{11}(4,1) \simeq -7.32\mathcal{C}\bar{T}$ is very large as compared to other coefficients for relatively large asymmetry parameter. In addition the other coefficient $\mathcal{L}_1^2(4,1)$ is also strongly asymmetry dependent. Presence of these coefficients is solely manifested by the finite asymmetry of the junction. Therefore we argue that measuring this cross coefficient would be useful while identifying the asymmetry of the junction in addition to its physical implications. Just from the structure of Eq. (3.53), it is seen that the thermoelectric transport properties of beyond half-filled SU(4) Kondo effects can be easily manipulated by tuning the junction asymmetry. It appears that the effect of asymmetry becomes more pronounced in relatively high temperature gradient regime. The asymmetry parameter \mathcal{C} mainly causes to shift the zero-current line either upward or downward with respect to the perfectly symmetric setup. As shown in Fig. 3.3 the positive value of the asymmetry parameter increases the thermo-voltage, while the opposite effects are apparent for the corresponding negative values. In addition, the beyond linear response contribution always overshoots the corresponding linear response value irrespective of the coupling asymmetry.

3.4.3 Paradigmatic SU(4) Kondo effects

The cosine factor $\cos 2\delta_0$ in front of the expression of the inelastic current dramatically modifies the low energy transport behavior of SU(N) Kondo effects. In case of the SU(N) systems with m electrons satisfying the specific combination such that $m/N=(2n+1)/4$, $n=0$ and 1 , the cosine factor $\cos 2\delta_0$ in Eq. (3.33) amounts to nullify the whole expression. For these specific systems, the non-Hartree contribution to the self-energy becomes zero but the corresponding Hartree contribution

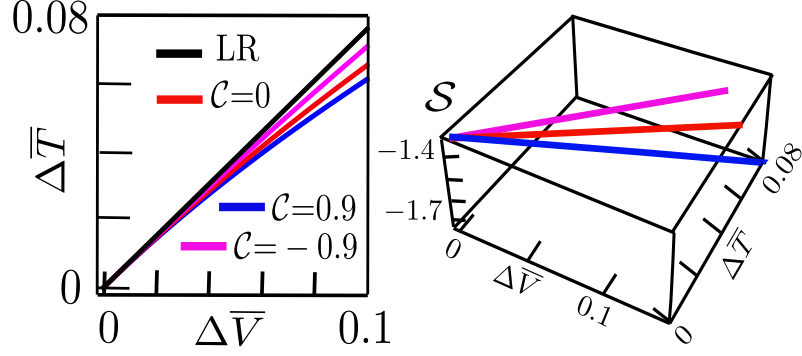


Figure 3.3: Left panel: Plot of asymmetry dependent zero current lines in PH asymmetric SU(4) Kondo effects within the quadratic response level of calculations as a function of applied voltage bias and temperature gradient at reference temperature $\bar{T} = 0.2$. Right panel: Corresponding Seebeck coefficients for given asymmetry parameter.

remains finite. In addition, for PH symmetric SU(N) Kondo effects the Hartree contribution vanishes and non-Hartree contribution becomes finite. On one hand, the PH asymmetric SU(4) Kondo impurity have good thermoelectric properties, on the other hand these systems offer vanishing non-Hartree contribution to the self-energy. Since the Hartree contributions can be straightforwardly accounted for by including it in phase shift, the beyond-half filled SU(4) systems can be exactly solved within cubic response and even beyond. This paradigmatic simplification is also applicable for some SU(12) generalizations. From Eq. (3.24) we obtained two non-zero cubic response coefficients $\mathcal{L}_1^3(4, 1)$ and $\mathcal{L}_{12}^{12}(4, 1)$ contributing to the charge current of beyond-half filled SU(4) Kondo impurity as

$$\mathcal{J}(4, 1)|_{\text{cubic}} = \mathcal{L}_1^3(4, 1)(\Delta\bar{V})^3 + \mathcal{L}_{12}^{12}(4, 1)\Delta\bar{V}(\Delta\bar{T})^2.$$

Here the transport coefficients are

$$\mathcal{L}_1^3(4, 1) = -\frac{1-3\mathcal{C}^2}{9\sqrt{\pi}} \frac{\Gamma[1/4]}{\Gamma[3/4]}, \quad \mathcal{L}_{12}^{12}(4, 1) = -\mathcal{C} \frac{2\pi^2}{9\sqrt{\pi}} \frac{\Gamma[1/4]}{\Gamma[3/4]}.$$

These equations show that for the perfectly symmetrical single electron SU(4) Kondo setups, the effects of voltage bias and temperature gradient are not correlated even in cubic response level of calculations. Therefore, only the presence of junction asymmetry can result the combine interplay of voltage bias and temperature gradient. The effects of asymmetry parameter on the Seebeck coefficient in cubic response level of calculations have been presented in Fig. 3.4 with an example of single electron SU(4) Kondo effects. From Fig. 3.4 it is seen that with the proper choice (positive value) of asymmetry parameter \mathcal{C} the non-linear Seebeck coefficient gets significantly enhanced over the corresponding perfectly symmetrical coupling. This effect is associated with the fact that the transmission coefficient Eq. (3.19) is strongly asymmetry dependent when the beyond linear response is considered.

At the end of this section we want to mention that the nonlinearly has been also studied by generalizing the definition of Seebeck coefficient with constant current condition [125–127] such

that

$$\bar{S}(N, m) = \frac{\partial \mathcal{J}(N, m)}{\partial \Delta \bar{T}} \bigg/ \frac{\partial \mathcal{J}(N, m)}{\partial \Delta \bar{V}}. \quad (3.54)$$

In the linear response level of calculation the response coefficient defined in Eq. (3.54) coincides with the Seebeck coefficient given by Eq. (3.37). Though their behaviors in non-linear regime is quite different, it has been argued that the coefficient \bar{S} is indeed experimentally accessible [125] and can provide an important ingredient that could be useful for the temperature sensing application. These effects have been already studied in conventional SU(2) Kondo regime accounting for the linear response of temperature gradient and finite voltage bias [125, 126]. Our result expressed in Eq. (3.39) paved a straightforward way of extending their study with an account of strong non-linearity in more exotic Kondo correlated system.

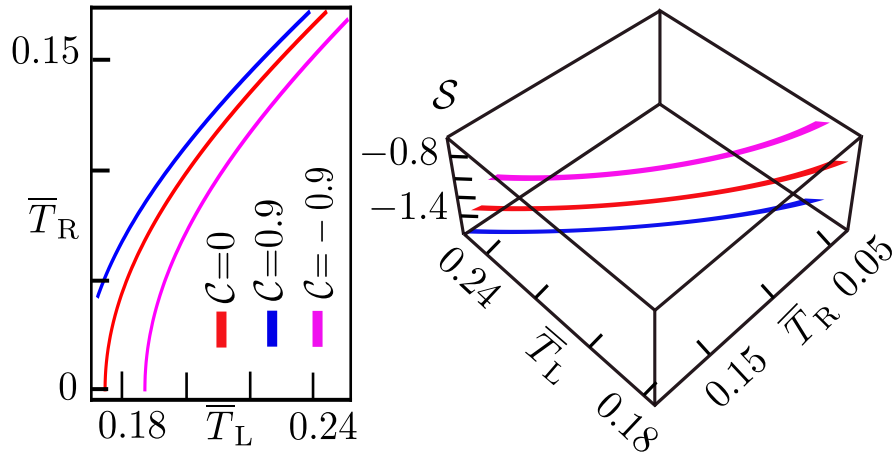


Figure 3.4: Left panel: Lines of zero charge currents in a single electron SU(4) Kondo impurity within cubic response level of calculations. The temperatures of left and right reservoirs (normalized with corresponding Kondo temperature) are varied for given asymmetry parameter at fixed voltage drop $\Delta \bar{V}=0.1$. Right panel: The Seebeck coefficient as a function of asymmetry parameter with beyond half-filled SU(4) Kondo effects.

3.4.4 Possible resolution of the thermovoltage offset observed in experiment

In linear response level of calculation, the Eq. (3.39) results in the charge current

$$I_c = G(T)\Delta V + G_{12}(T)\Delta T, \quad (3.55)$$

with G and G_{12} being the electrical conductance and thermo-electric coefficient respectively,

$$G(T) = \left[\sin^2 \left(\frac{\pi m}{N} \right) + \frac{1}{3} \frac{N+1}{N-1} \cos \left(\frac{2\pi m}{N} \right) (\pi \bar{T})^2 \right], \quad (3.56)$$

$$G_{12}(T) = - \left[\frac{\pi^2}{3} \bar{T} \sin \left(\frac{2\pi m}{N} \right) \right]. \quad (3.57)$$

As we anticipated earlier and also seen from Eq. (3.57), the thermo-electric coefficient $G_{12}(T)$ vanishes for the PHS variants of SU(N) Kondo effects such as the conventional SU(2) Kondo effect.

This effect is responsible also for the nullification of the thermopower (differential thermopower) of PH symmetric Kondo effects. This observation results in the following interesting questions:

- i) Does the non-differential thermopower (beyond linear response) of PHS Kondo effects also vanishes?
- ii) What causes to have the experimentally observed finite thermoelectric response at the apparent PH symmetric point [32]?

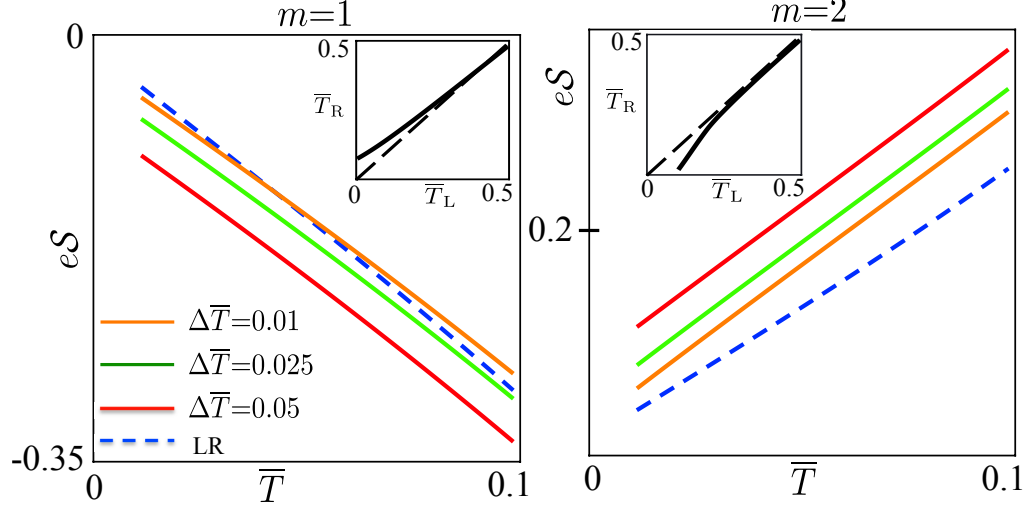


Figure 3.5: Main frame: Thermopower \mathcal{S} of a SU(4) Kondo impurity with $m=1$ and $m=2$ electrons as a function of the reference temperature $\bar{T}=\bar{T}_R$ where the blue dashed curve shows the differential \mathcal{S} (linear response) and the solid curves correspond to \mathcal{S} defined under zero-current condition including upto the cubic response on the voltage bias and temperature gradient. Insert: evolution of the zero current steady state as a function of the temperatures of L-R reservoirs at finite voltage bias $e\Delta\bar{V}=0.02$. For this plot we fixed the potential scattering at $\delta_p=0.3$ and asymmetry parameter $\mathcal{C}=0$. All of the parameters in this figure have been chosen so as to have the close matching with the experiment [32].

The model geometry under consideration resembles the experimental setup in Ref. [32]. The temperature of the drain reservoir (R) is taken as the reference temperature of the system. The temperature of the source reservoir (L) is controlled by the Joule heat released due to the finite current flowing along the lead [32]. Thus, the temperature drop ΔT is fixed for all measurements. The bias voltage ΔV is applied between the source and the drain in order to stop the thermo-current as shown in Fig. 3.1.

The thermopower *measurements* [32] refer however *not* to the differential Seebeck effects. Since there were no independent measurements of T_L and T_R , the temperature drop was estimated from the Joule heat. It appeared that the ΔT was finite and *not* fulfilling the condition $|\Delta T| \ll T_R$. To demonstrate the significance of non-linear effects associated with finite temperature drop we show on Fig. 3.5 the thermopower of SU(4) model computed by two different methods: i) the dashed blue line stands for the differential thermopower $\mathcal{S}(T)=G_{12}/G$ where G_{12} is obtained at zero voltage drop while G is calculated at equal temperatures of the leads; ii) the solid lines

corresponds to $\mathcal{S} = -\Delta V / \Delta T$ resembling the experimental situation in [32]: the temperature drop is fixed $\Delta T / T_K = 0.05$ (red) 0.025 (green) 0.01 (orange) and the thermo-voltage is obtained from the zero current condition. As one can see, at small reference temperatures “finite ΔT ” thermopower always *overshoots* the differential \mathcal{S} . The effect is more pronounced in PH symmetric regime. The offset can be easily understood on trivial example of SU(4) $m=1$ and $\delta_P=0$. In that case the inelastic contribution to the current vanishes and the non-linear effect is $\propto (\Delta T)^2$. Therefore, the offset is linear in ΔT and can be used as a measure of the temperature drop. This observation can explain the thermo-voltage offset observed in the experiment [32] in the Kondo limit of SU(2) quantum impurity (PHS regime). According to our calculations this offset is associated with a non-linear ΔT dependence of the current at low reference temperatures (see Fig. 3.5 inserts). We suggest to check this statement experimentally by performing Seebeck effect measurements varying the temperature in the “hot” lead.

3.5 Peltier effects

Peltier effect describes the generation of a heat current I_h due to the charge current I_c driven in a circuit under isothermal condition $T_L = T_R$ by an applied voltage bias $e\Delta V$ [128]. The Peltier coefficient Π^γ associated with the γ reservoir is defined as

$$\Pi^\gamma = \left. \frac{I_h^\gamma}{I_c} \right|_{T_L = T_R}. \quad (3.58)$$

This coefficient imparts valuable informations on the characterization of how good a material is for thermoelectric solid-state refrigeration or power generation. While the linear response Peltier coefficient Π_0 is related to the corresponding Seebeck coefficient \mathcal{S}^{LR} via the Kelvin relation $\Pi_0 = T\mathcal{S}^{\text{LR}}$, their behavior in non-linear regime is quite different [129–131]. Since the Peltier heat is measured under the isothermal condition, its computation is straightforward using the effective transmission coefficient given in Eq. (3.36) to compute the heat current following out of the left reservoir,

$$I_h^L|_{\Delta T=0} = \frac{1}{h} \sum_r^N \int_{-\infty}^{\infty} d\varepsilon (\varepsilon - \mu_L) T_r^{\text{eff}} [f_L(\varepsilon) - f_R(\varepsilon)].$$

For the propose of demonstration we consider the perfectly symmetrical setup with $\mathcal{C}=0$ and write the heat current up to the cubic order in ΔV as

$$\mathcal{I}_h \equiv \frac{I_h^L}{\frac{Ne^2}{h} \left(T_K^{\text{SU}(N)}\right)^2} = \mathcal{M}_1 \Delta \bar{V} + \mathcal{M}_2 (\Delta \bar{V})^2 + \mathcal{M}_3 (\Delta \bar{V})^3. \quad (3.59)$$

Here the heat-transport coefficients $\mathcal{M}_{1,2,3}$ (with $e = -1$) are given as

$$\mathcal{M}_1|_{\mathcal{C}=0} = -\frac{(\pi \bar{T})^2}{3} \sin 2\delta_0, \quad (3.60)$$

$$\mathcal{M}_2|_{\mathcal{C}=0} = -\frac{1}{2} \sin^2 \delta_0, \quad (3.61)$$

$$\mathcal{M}_3|_{\mathcal{C}=0} = -\frac{1}{12} \sin 2\delta_0. \quad (3.62)$$

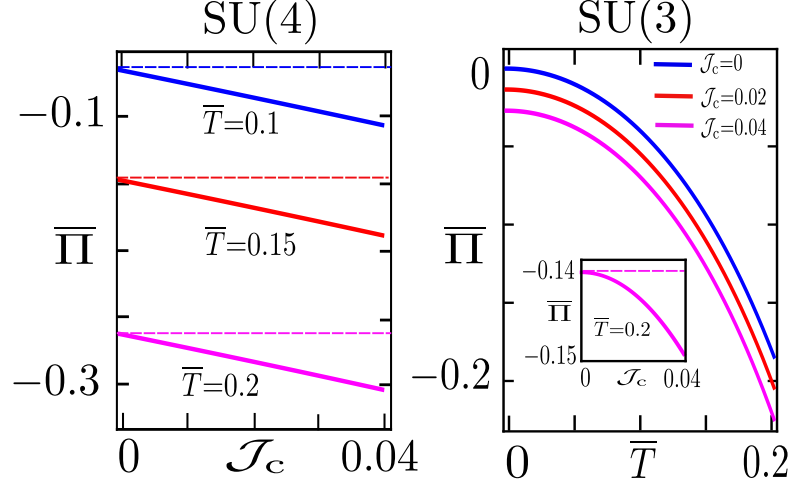


Figure 3.6: Peltier coefficients of beyond half-filled $SU(N)$ Kondo effects. Right panel: The correction to the linear response Peltier coefficient for single electron $SU(4)$ Kondo effect according to the Eq. (3.68). The dotted line represents the Peltier coefficients associated with the linear response contribution which is independent of charge current. Left panel: Variation of Peltier coefficient of single electron $SU(3)$ Kondo effect with normalized reference temperature \bar{T} . Inset shows the Peltier coefficient at fixed \bar{T} with varying normalized charge current.

Note that the transport coefficients $\mathcal{M}_{1,2,3}$ are obtained by constraining the heat current Eq. (3.59) within cubic order in energy, namely the terms of the form $\propto T^2(\Delta V)^2$ has been neglected. Similarly upto the cubic order in ΔV the charge current calculated under the isothermal condition is

$$\mathcal{J}_c \equiv \frac{I_c}{\frac{Ne^2}{h} T_K^{SU(N)}} = \mathcal{L}_1^1 \Delta \bar{V} + \mathcal{L}_1^2 \Delta \bar{V}^2 + \mathcal{L}_1^3 \Delta \bar{V}^3. \quad (3.63)$$

While the coefficient \mathcal{L}_1^2 vanishes for symmetrical setup, the first and third order response coefficients $\mathcal{L}_1^{1,3}$ are given by

$$\mathcal{L}_1^1|_{c=0} = \left[\sin^2 \delta_0 + \frac{1}{3} \frac{N+1}{N-1} \cos 2\delta_0 (\pi \bar{T})^2 \right], \quad (3.64)$$

$$\mathcal{L}_1^3|_{c=0} = \left[\frac{1}{12} \frac{N+4}{N-1} \cos 2\delta_0 - \frac{\mathcal{A}}{6} \sin 2\delta_0 \right]. \quad (3.65)$$

We then proceed with the calculation of the dimensionless Peltier coefficient defined by

$$\bar{\Pi} \equiv \Pi^L / T_K^{SU(N)} = \mathcal{I}_h / \mathcal{J}_c. \quad (3.66)$$

Inverting the normalized charge current Eq. (3.63) we get

$$\Delta \bar{V}|_{c=0} = \frac{1}{\mathcal{L}_1^1} \mathcal{J}_c - \frac{\mathcal{L}_1^3}{(\mathcal{L}_1^1)^4} \mathcal{J}_c^3 + \dots \quad (3.67)$$

Plugging in the expression of $\Delta \bar{V}$ from Eq. (3.67) into the expression of normalized heat current Eq. (3.59) and using the Eq. (3.66), we get the expression of dimensionless form of Peltier coefficient

$$\bar{\Pi}|_{c=0} = \bar{\Pi}_0 + \frac{\mathcal{M}_2}{(\mathcal{L}_1^1)^2} \mathcal{J}_c + \frac{\mathcal{L}_1^1 \mathcal{M}_3 - \mathcal{L}_1^3 \mathcal{M}_1}{(\mathcal{L}_1^1)^4} \mathcal{J}_c^2 + \dots \quad (3.68)$$

Here we defined the dimensionless form of linear response Peltier coefficient as $\bar{\Pi}_0 = \mathcal{M}_1/\mathcal{L}_1^1$. As presented in Eqs. (3.60)–(3.62), the heat transport coefficient \mathcal{M}_1 get nullified for PH symmetric SU(N) Kondo impurity thereby vanishes the corresponding linear response Peltier coefficient $\bar{\Pi}_0|_{\text{PH}} = 0$. Since the coefficient \mathcal{M}_2 is non-zero even for the PH symmetric systems, the first order correction to the Peltier coefficient remain finite for all the variants of SU(N) Kondo effects. Interestingly PH symmetric setups do not offer the second order correction to the Peltier coefficient, only the odd-order corrections remain finite. This indicates the poor rectification performance of half-filled Kondo impurity as compared to the corresponding beyond half-filled setups. The Peltier coefficients of single electron SU(3) and SU(4) Kondo effects as given in Eq. (3.68) are shown in Fig. 3.6. It is seen from Fig. 3.6 that the non-linear correction to the Peltier coefficients for SU(4) Kondo effects are very significant. Appreciable non-linear correction are also apparent for SU(3) Kondo effects. Finite value of asymmetry parameter $\mathcal{C} \neq 0$ amounts to produce the second order term in the voltage expression Eq. (3.67) and renormalizes the coefficient in its third order correction. These effects tend to modify the first and second order correction to the Peltier coefficient Eq. (3.68) without affecting the zeroth order term $\bar{\Pi}_0$. Therefore role of coupling asymmetry toward the enhancement of Peltier coefficient is similar to that for Seebeck coefficient as discussed earlier. In addition, Eq. (3.36) would be sufficient to explore the correction to the Wiedemann-Franz law [132], connecting electronic and thermal conductivities, associated with the non-linear effects in SU(N) Kondo effects.

3.6 Summary

We developed a theoretical framework based on the local Fermi-liquid theory in combination with the out of equilibrium Keldysh approach to study the thermoelectric transport in the strong-coupling regime of a SU(N) Kondo impurity. Two reciprocal measurements of thermoelectricity, namely, the Seebeck and Peltier effects are investigated in strongly non-linear regime. We demonstrated the importance of non-linearity in thermoelectric characterization by considering experimentally studied SU(2) and SU(4) Kondo effects in QDs and CNTs. We observed that the finite temperature gradient thermopower (non-differential) always overshoots the corresponding differential one in all studied SU(N) Kondo variants. This effect is likely to be sufficient for the resolution of the experimental puzzle on the observation of finite thermopower on PH symmetric point of SU(2) Kondo impurity. The local Fermi-liquid theory of thermoelectricity presented in this chapter also accounts for the effects associated with the coupling asymmetry. While in linear response the Seebeck and Peltier coefficients and hence the thermopower are independent of coupling asymmetry, the fundamental role of coupling asymmetry towards the enhancement of thermopower of a SU(N) Kondo setup is explored. The presented analytical expressions of asymmetry dependent transport coefficients for general SU(N) Kondo effects allow us to make a close connection of our findings with the experimentally studied SU(2) and SU(4) Kondo effects in complex QDs nano structures. Heat and charge transport with theoretically proposed SU(3) Kondo effects is discussed in detail. Application of developed theoretical framework for the investigation of thermoelectric properties of more exotic Kondo problems such as multi-stage [2, 3] and multi-terminal Kondo screening appears to be the valid avenues for future research.

Chapter 4

Two-color Fermi liquid theory for transport through a multilevel Kondo impurity

In this chapter we investigate the charge current through the two-stage Kondo effect and analyze various transport properties. The content of this chapter has been previously published as:

D. B. Karki, Christophe Mora, Jan von Delft, and Mikhail N. Kiselev,
Two-color Fermi-liquid theory for transport through a multilevel Kondo impurity,
[Phys. Rev. B **97**, 195403 \(2018\)](#) [Selected as Editors' Suggestion].

4.1 Background

It is almost four decades since the seminal work of Nozieres and Blandin (NB) [22] about the Kondo effect in *real* metals. The concept of the Kondo effect studied for impurity spin $S=1/2$ interacting with a single orbital channel $\mathcal{K}=1$ of conduction electrons [7, 16–18, 20, 23, 39–41] was extended in [22] for arbitrary spin S and arbitrary number of channels \mathcal{K} . A detailed classification of possible ground states corresponding to the under-screened $\mathcal{K}<2S$, fully screened $\mathcal{K}=2S$ and overscreened $\mathcal{K}>2S$ Kondo effect has been given in [26, 42, 43]. Furthermore, it has been argued that in real metals the spin-1/2 single-channel Kondo effect is unlikely to be sufficient for the complete description of the physics of a magnetic impurity in a non-magnetic host [29, 47–52]. In many cases truncation of the impurity spectrum to one level is not possible and besides there are several orbitals of conduction-electrons which interact with the higher spin $S>1/2$ of the localized magnetic impurity [10], giving rise to the phenomenon of multi-channel Kondo screening [24, 53]. In the fully screened case the conduction electrons completely screen the impurity spin to form a singlet ground state [44]. As a result, the low-energy physics is described by a local Fermi-

Liquid (FL) theory [20, 22]. In the under-screened Kondo effect there exist not enough conducting channels to provide complete screening [45, 46]. Thus, there is a finite concentration of impurities with a residual spin contributing to the thermodynamic and transport properties. In contrast to the underscreened and fully-screened cases, the physics of the overscreened Kondo effect is not described by the FL paradigm resulting in dramatic change of the thermodynamic and transport behaviour [10].

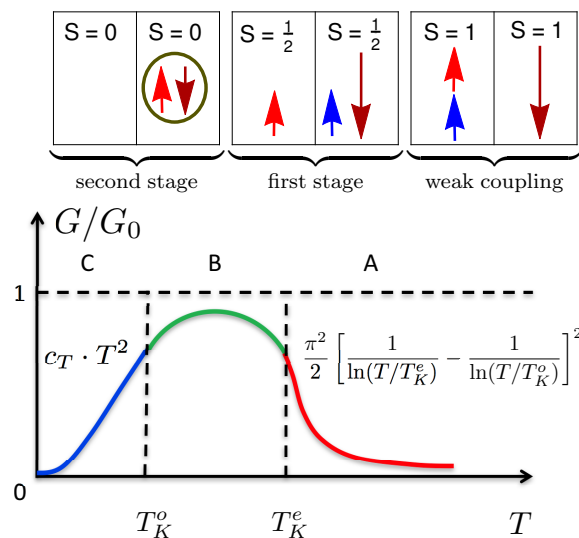


Figure 4.1: (Color online) Cartoon for non-monotonic behaviour of the differential conductance G/G_0 ($G_0 = 2e^2/h$ is the conductance quantum) as a function of temperature resulting from a two-stage Kondo effect. There are three characteristic regimes: (A) weak, (B) intermediate and (C) strong coupling. Crossover energy scales T_K^e and T_K^o are defined in the Section 4.2. In the weak coupling (A)-regime the screening is absent (see top panel) and the transport coefficients are fully described by the perturbation theory [29]. In the intermediate regime (B), the Kondo impurity is partially screened (see the first stage at the top panel); the residual interaction of electrons with the under-screened spin is antiferromagnetic [22]. The description of the FL transport coefficients in the strong coupling regime (C) at the second stage of the screening is the central result of this chapter.

The simplest realization of the multi-channel fully screened Kondo effect is given by the model of a $S=1$ localized impurity screened by two conduction electron-channels. It has been predicted [29] that in spite of the FL universality class of the model, the transport properties of such FL are highly non-trivial. In particular, the screening develops in two stages (see Fig. 4.1), resulting in non-monotonic behaviour of the transport coefficients (see review [29] for details).

The interest in the Kondo effect revived during the last two decades due to progress in fabrication of nano-structures [8]. Usually in nanosized objects such as quantum dots (QDs), carbon nanotubes (CNTs), quantum point contacts (QPCs) etc., Kondo physics can be engineered by fine-tuning the external parameters (e.g. electric and magnetic fields) and develops in the presence of several different channels of the conduction electrons coupled to the impurity. Thus,

it was timely [8, 29, 49, 133–136] to uncover parallels between the Kondo physics in real metals and the Kondo effect in real quantum devices. The challenge of studying multi-channel Kondo physics [22, 24] was further revived in connection with possibilities to measure quantum transport in nano-structures experimentally [35, 73, 137–140] inspiring also many new theoretical suggestions [26, 45, 89, 141–143].

Unlike the $S=1/2$, $\mathcal{K}=1$ Kondo effect (1CK), the two-channel $S=1$ Kondo problem suffers from lack of universality for its observables [22]. The reason is that certain symmetries (e.g. conformal symmetry) present in 1CK are generally absent in the two-channel $S=1$ model. This creates a major obstacle for constructing a complete theoretical description in the low-energy sector of the problem. Such a description should, in particular, account for a consistent treatment of the Kondo resonance [24] appearing in both orbital channels. The interplay between two resonance phenomena, being the central reason for the non-monotonicity of transport coefficients [29], has remained a challenging problem for many years [45, 89].

A sketch of the temperature dependence of the differential electric conductance is shown on Fig. 4.1. The most intriguing result is that the differential conductance vanishes at both high and low temperatures, demonstrating the existence of two characteristic energy scales (see detailed discussion below). These two energy scales are responsible for a two-stage screening of $S=1$ impurity. Following [45, 89] we will refer to the $S=1$, $\mathcal{K}=2$ Kondo phenomenon as the two-stage Kondo effect (2SK).

While both the weak (A) and intermediate (B) coupling regimes are well-described by the perturbation theory [29], the most challenging and intriguing question is the study of strong-coupling regime (C) where both scattering channels are close to the resonance scattering. Indeed, the theoretical understanding of the regime C (in- and out-of-equilibrium) constitutes a long-standing problem that has remained open for more than a decade. Consequently, one would like to have a theory for the leading dependence of the electric current I and differential conductance $G=\partial I/\partial V$ on magnetic field (B), temperature (T) and voltage (V),

$$G(B, T, V)/G_0 = c_B B^2 + c_T (\pi T)^2 + c_V V^2.$$

Here $G_0=2e^2/h$ is unitary conductance. Computation of these parameters c_B , c_T and c_V using a local FL theory and to show how are these related constitute the main message of this work. In this chapter we develop a full-fledged theory of the two-stage Kondo model at small but finite temperature, magnetic field and bias voltage to explain the charge transport (current, conductance) behavior in the strong-coupling regime of the 2SK effect.

4.2 Theoretical formulation

We consider a multi-level quantum dot sandwiched between two external leads α ($=L, R$) as shown in Fig. 4.2. The generic Hamiltonian is defined by the Anderson model

$$H = \sum_{k\alpha\sigma} (\xi_k + \varepsilon_\sigma^Z) c_{\alpha k\sigma}^\dagger c_{\alpha k\sigma} + \sum_{\alpha k i\sigma} t_{\alpha i} c_{\alpha k\sigma}^\dagger d_{i\sigma} + \text{H.c.} \\ + \sum_{i\sigma} (\varepsilon_i + \varepsilon_\sigma^Z) d_{i\sigma}^\dagger d_{i\sigma} + E_c \hat{N}^2 - \mathcal{J} \hat{\mathbf{S}}^2, \quad (4.1)$$

where c_α stands for the Fermi-liquid quasiparticles of the source (L) and the drain (R) leads, $\xi_k = \varepsilon_k - \mu$ is the energy of conduction electrons with respect to the chemical potential μ , and spin $\sigma = \uparrow (+), \downarrow (-)$ and $\varepsilon_\sigma^Z = -\sigma B/2$. The operator $d_{i\sigma}$ describes electrons with spin σ in the i -th orbital state of the quantum dot and $t_{\alpha i}$ are the tunneling matrix elements, as shown in Fig. 4.2. Here $\varepsilon_i + \varepsilon_\sigma^Z$ is the energy of the electron in i -th orbital level of the dot in the presence of a Zeeman field B , E_c is the charging energy (Hubbard interaction in the Coulomb blockade regime [144]), $\mathcal{J} \ll E_c$ is an exchange integral accounting for Hund's rule [89] and $\hat{N} = \sum_{i\sigma} d_{i\sigma}^\dagger d_{i\sigma}$ is the total number of electrons in the dot. We assume that the dot is occupied by two electrons, and thus the expectation value of \hat{N} is $\bar{n}_d = 2$ and the total spin $S = 1$ (see Fig. 4.2). By applying a Schrieffer-Wolff (SW) transformation [112] to the Hamiltonian Eq. (4.1) we eliminated the charge fluctuations between two orbitals of the quantum dot and project out the effective Hamiltonian, written in the L - R basis, onto the spin-1 sector of the model [29, 89]:

$$H_{\text{eff}} = \sum_{k\alpha\sigma} \xi_k c_{\alpha k\sigma}^\dagger c_{\alpha k\sigma} + \sum_{\alpha\alpha'} J_{\alpha\alpha'} [\mathbf{s}_{\alpha\alpha'} \cdot \mathbf{S}], \quad (4.2)$$

with $\alpha, \alpha' = L, R$, $B=0$ and

$$\mathbf{s}_{\alpha\alpha'} = \frac{1}{2} \sum_{kk'\sigma_1\sigma_2} c_{\alpha k\sigma_1}^\dagger \boldsymbol{\tau}_{\sigma_1\sigma_2} c_{\alpha' k'\sigma_2}, \quad (4.3)$$

$$\mathbf{S} = \frac{1}{2} \sum_{i\sigma_1\sigma_2} d_{i\sigma_1}^\dagger \boldsymbol{\tau}_{\sigma_1\sigma_2} d_{i\sigma_2}, \quad (4.4)$$

$$J_{\alpha\alpha'} = \frac{2}{E_c} \begin{pmatrix} |t_{L1}|^2 + |t_{L2}|^2 & t_{L2}^* t_{R2} + t_{L1}^* t_{R1} \\ t_{L2} t_{R2}^* + t_{L1} t_{R1}^* & |t_{R2}|^2 + |t_{R1}|^2 \end{pmatrix}, \quad (4.5)$$

where we use the short-hand notation $\boldsymbol{\tau}_{\sigma_i\sigma_j} \equiv \boldsymbol{\tau}_{\sigma_i\sigma_j}$ for the Pauli matrices.

The determinant of the matrix $J_{\alpha\alpha'}$ in Eq. (4.5) is non-zero provided that $t_{L2}t_{R1} \neq t_{L1}t_{R2}$. Therefore, one may assume without loss of generality that both eigenvalues of the matrix $J_{\alpha\alpha'}$ are non-zero and, hence, both scattering channels interact with the dot. There are, however, two important cases deserving an additional discussion. The first limiting case is achieved when two eigenvalues of $J_{\alpha\alpha'}$ are equal and the matrix $J_{\alpha\alpha'}$ is proportional to the unit matrix in any basis of electron states of the leads. As a result, the net current through impurity vanishes at any temperature, voltage and magnetic field [89] (see Fig. 4.1 which shows that the differential conductance vanishes when symmetry between channels emerges). This is due to destructive interference between two paths [89] (Fig. 4.2) occurring when e.g. $t_{L1}=t_{L2}=t_{R1}=t$, $t_{R2}=-t$. Precise calculations done later in this chapter highlight the role of destructive interference effects and quantify how the

current goes to zero in the vicinity of the symmetry point. The second limiting case is associated with constructive interference between two paths (Fig. 4.2) when $t_{L1}=t_{L2}=t_{R1}=t_{R2}=t$. In that case the determinant of the matrix $J_{\alpha\alpha'}$ in Eq. (4.5) and thus also one of the eigenvalues of $J_{\alpha\alpha'}$, is zero. As a result, the corresponding channel is completely decoupled from the impurity. The model then describes the under-screened $S=1$ single-channel Kondo effect.

Applying the Glazman-Raikh rotation [111] $b_{e/o}^\dagger=(c_L^\dagger\pm c_R^\dagger)/\sqrt{2}$ to the effective Hamiltonian Eq. (4.2) we re-write the Kondo Hamiltonian in the diagonal basis¹, introducing two coupling constants J_e, J_o

$$\mathcal{H}_{\text{eff}} = \sum_a (H_0^a + J_a \mathbf{s}_a \cdot \mathbf{S}). \quad (4.6)$$

In writing Eq. (4.6) we assigned the generalized index “ a ” to represent the even and odd channels ($a=e, o$). $H_0^a = \sum_{ak\sigma} (\varepsilon_k - \mu) b_{ak\sigma}^\dagger b_{ak\sigma}$ is the non-interacting Hamiltonian of channel a in the rotated basis. The spin density operators in the new basis are: $\mathbf{s}_a = 1/2 \sum_{kk'\sigma_1\sigma_2} b_{ak\sigma_1}^\dagger \boldsymbol{\tau}_{\sigma_1\sigma_2} b_{ak'\sigma_2}$. For equal leads-dot coupling, the J_a are of the order of t^2/E_c . The interaction between even and odd channels is generated by the next non-vanishing order of Schrieffer-Wolff transformation

$$H_{eo} = -J_{eo} \mathbf{s}_e \cdot \mathbf{s}_o, \quad (4.7)$$

where J_{eo} is estimated as $J_{eo} \sim J_e J_o / \max[E_c, \mu]$. As a result this term is irrelevant in the weak coupling regime. However, we note that the sign of J_{eo} is positive, indicating the ferromagnetic coupling between channels necessary for the complete screening of the $S = 1$ impurity [22] (see Fig. 4.1).

The Hamiltonian (4.6) describes the weak coupling limit of the two-stage Kondo model. The coupling constants J_e and J_o flow to the strong coupling fixed point (see details of the renormalization group (RG) analysis [18, 41, 146] in Appendix 4.A.1). In the leading-log (one loop RG) approximation, the two channels do not talk to each other. As a result, two effective energy scales emerge, referred as Kondo temperatures, $T_K^a = D \exp(-1/(2N_F J_a))$ (D is a bandwidth and N_F is 3-dimensional electron’s density of states in the leads). These act as crossover energies, separating three regimes: the weak-coupling regime, $T \gg \max[T_K^a]$ (see Appendix 4.A.1); the intermediate regime, $\min[T_K^a] \ll T \ll \max[T_K^a]$ characterized by an incomplete screening (see Fig. 4.1) when one conduction channels (even) falls into a strong coupling regime while the other channel (odd) still remains at the weak coupling (see Appendix 4.A.2); and the strong-coupling regime, $T \ll \min[T_K^a]$. In the following section we discuss the description of the strong coupling regime by a local Fermi-liquid paradigm.

4.3 Fermi-Liquid Hamiltonian

¹For the sake of simplicity we assume certain symmetry in the dot-leads junction. Namely, the new basis diagonalizing the Hamiltonian Eq. (4.2) corresponds to symmetric (even) and anti-symmetric (odd) combinations of the states in the L-R leads. The effects of coupling asymmetry can straightforwardly be accounted by using methods developed in Ref. [106, 107]

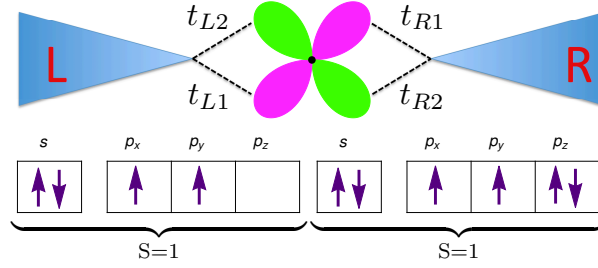


Figure 4.2: (Color online) Cartoon of some possible realization of a multi-orbital Anderson model setup: two degenerate p -orbitals (magenta and green) of a quantum dot are occupied by one electron each forming a triplet $S=1$ state in accordance with the Hund’s rule [145] (see lower panel). The third p -orbital (not shown) is either empty or doubly occupied. Two limiting cases are important: i) totally constructive interference $t_{L1}=t_{L2}=t_{R1}=t_{R2}=t$; ii) totally destructive interference $t_{L1}=t_{L2}=t_{R1}=t$, $t_{R2}=-t$. Besides, if $t_{L2}=t_{R2}=0$, only one orbital is coupled to the leads, resulting in the 1CK model. If $t_{L2}=t_{R1}=0$, each orbital is coupled to a “dedicated lead” and the net current through the dot is zero.

The RG analysis of the Hamiltonian (4.6) (see Appendix 4.A.1 for details) shows that the 2SK model has a unique strong coupling fixed point corresponding to complete screening of the impurity spin. This strong-coupling fixed point is of the FL-universality class. In order to account for existence of two different Kondo couplings in the odd and even channels and the inter-channel interaction, we conjecture that the strong-coupling fixed point Hamiltonian contains three leading irrelevant operators:

$$H = - \sum_{aa'} \lambda_{aa'} : \mathbf{s}_a(0) \cdot \mathbf{s}_{a'}(0) :, \quad (4.8)$$

with $\lambda_{ee}=\lambda_e$, $\lambda_{oo}=\lambda_o$ and $\lambda_{eo}=\lambda_{oe}$. The notation $: \dots :$ corresponds to a normal ordering where all divergences originating from bringing two spin currents \mathbf{s}_a close to each other are subtracted. The conjecture (4.8) is in the spirit of Affleck’s ideas [24] of defining leading irrelevant operators of minimal operator dimension being simultaneously (i) local, (ii) independent of the impurity spin operator \mathbf{S} , (iii) rotationally invariant and (iv) independent of the local charge density. We do not assume any additional (SO(3) or SU(2)) symmetry in the channel subspace except at the symmetry-protected point $\lambda_e=\lambda_o=\lambda_{eo}=\lambda$. At this symmetry point a new conservation law for the total spin current [24] emerges and the Hamiltonian reads as

$$H = -\lambda : \mathbf{S}(0) \cdot \mathbf{S}(0) :, \quad \mathbf{S} = \mathbf{s}_e + \mathbf{s}_o.$$

This symmetric point is obtained with the condition $J_e=J_o$ in H_{eff} , see Eq. (4.6). Under this condition, as has been discussed in the previous section, the net current through the impurity is zero due to totally destructive interference. This symmetry protects the zero-current state at any temperature, magnetic and/or electric field (see Fig. 4.2).

Applying the point-splitting procedure [24, 147] to the Hamiltonian Eq. (4.8), we get $H =$

$H_e + H_o + H_{eo}$ with

$$\begin{aligned} H_a &= -\frac{3}{4}i\lambda_a \sum_{\sigma} \left[b_{a\sigma}^{\dagger} \frac{d}{dx} b_{a\sigma} - \left(\frac{d}{dx} b_{a\sigma}^{\dagger} \right) b_{a\sigma} \right] + \frac{3}{2}\lambda_a \rho_{a\uparrow} \rho_{a\downarrow}, \\ H_{eo} &= -\lambda_{eo} [:\mathbf{s}_e(0) \cdot \mathbf{s}_o(0) + \mathbf{s}_o(0) \cdot \mathbf{s}_e(0):]. \end{aligned} \quad (4.9)$$

The Hamiltonian Eq. (4.9) accounts for two copies of the $s=1/2$ Kondo model at strong coupling with an additional ferromagnetic interaction between the channels providing complete screening at $T=0$.

An alternative derivation of the strong-coupling Hamiltonian (4.9) can be obtained, following Refs. [107, 148, 149], with the most general form of the low-energy FL Hamiltonian. For the two-stage Kondo problem corresponding to the particle-hole symmetric limit of the two-orbital-level Anderson model, it is given by $H = H_0 + H_{\alpha} + H_{\phi} + H_{\Phi}$ with

$$\begin{aligned} H_0 &= \sum_{a\sigma} \int_{\varepsilon} \nu (\varepsilon + \varepsilon_{\sigma}^Z) b_{a\varepsilon\sigma}^{\dagger} b_{a\varepsilon\sigma} \\ H_{\alpha} &= -\sum_{a\sigma} \int_{\varepsilon_{1-2}} \frac{\alpha_a}{2\pi} (\varepsilon_1 + \varepsilon_2) b_{a\varepsilon_1\sigma}^{\dagger} b_{a\varepsilon_2\sigma} \\ H_{\phi} &= \sum_a \int_{\varepsilon_{1-4}} \frac{\phi_a}{\pi\nu} :b_{a\varepsilon_1\uparrow}^{\dagger} b_{a\varepsilon_2\uparrow} b_{a\varepsilon_3\downarrow}^{\dagger} b_{a\varepsilon_4\downarrow}: \\ H_{\Phi} &= -\sum_{\sigma_{1-4}} \int_{\varepsilon_{1-4}} \frac{\Phi}{2\pi\nu} :b_{\varepsilon_1\sigma_1}^{\dagger} \tau_{\sigma_{12}} b_{\varepsilon_2\sigma_2} b_{\varepsilon_3\sigma_3}^{\dagger} \tau_{\sigma_{34}} b_{\varepsilon_4\sigma_4}:, \end{aligned} \quad (4.10)$$

where $\nu=1/(2\pi\hbar v_F)$ is the density of states per species for a one-dimensional channel. In Eq. (4.10) H_{α} describes energy-dependent elastic scattering [24]. The inter and intra-channel quasiparticle interactions responsible for the inelastic effects are described by H_{Φ} and H_{ϕ} respectively. The particle-hole symmetry of the problem forbids to have any second-generation of FL-parameters [107] in Eq. (4.10). Therefore, the Hamiltonian Eq. (4.10) constitutes a minimal model for the description of a local Fermi-liquid with two interacting resonance channels. The direct comparison of the above FL-Hamiltonian with the strong-coupling Hamiltonian Eq. (4.9) provides the relation between the FL-coefficients at PH symmetry, namely $\alpha_a=\phi_a$. The Kondo floating argument (see [107]) recovers this relation. As a result we have three independent FL-coefficients α_e , α_o and Φ which can be obtained from three independent measurements of the response functions. The FL-coefficients in Eq. (4.10) are related to the leading irrelevant coupling parameters λ 's in Eq. (4.9) as

$$\alpha_a = \phi_a = \frac{3\lambda_a\pi}{2} \quad \text{and} \quad \Phi = \pi\lambda_{eo}, \quad (4.11)$$

The symmetry point $\lambda_e=\lambda_o=\lambda_{eo}=\lambda$ constrains $\alpha_e=\alpha_o=3\Phi/2$ in the Hamiltonian Eq. (4.10).

To fix three independent FL parameters in (4.10) in terms of physical observables, three equations are needed. Two equations are provided by specifying the spin susceptibilities of two orthogonal channels. The remaining necessary equation can be obtained by considering the impurity contribution to specific heat. It is proportional to an impurity-induced change in the total density of states per spin [10], $\nu_{a\sigma}^{\text{imp}}(\varepsilon)=\frac{1}{\pi}\partial_{\varepsilon}\delta_{\sigma}^a(\varepsilon)$, where $\delta_{\sigma}^a(\varepsilon)$ are energy dependent scattering phases in

odd and even channels (see the next Section for more details)

$$\frac{C^{\text{imp}}}{C_{\text{bulk}}} = \frac{\sum_{a\sigma} \frac{1}{\pi} \partial_\varepsilon \delta_\sigma^a(\varepsilon)|_{\varepsilon=0}}{4\nu} = \frac{\alpha_e + \alpha_o}{2\pi\nu}. \quad (4.12)$$

The quantum impurity contributions to the spin susceptibilities of the odd and even channels (see details in [147]) are given by

$$\frac{\chi_e^{\text{imp}}}{\chi_{\text{bulk}}} = \frac{\alpha_e + \Phi/2}{\pi\nu}, \quad \frac{\chi_o^{\text{imp}}}{\chi_{\text{bulk}}} = \frac{\alpha_o + \Phi/2}{\pi\nu}. \quad (4.13)$$

The equations (4.12-4.13) fully determine three FL parameters α_e , α_o and Φ in (4.10). Total spin susceptibility $\chi^{\text{imp}} = \chi_e^{\text{imp}} + \chi_o^{\text{imp}}$ together with the impurity specific heat (4.12) defines the Wilson ratio, $R = (\chi^{\text{imp}}/\chi_{\text{bulk}})/(C^{\text{imp}}/C_{\text{bulk}})$ [24, 150] which measures the ratio of the total specific heat to the contribution originating from the spin degrees of freedom

$$R = 2 \left[\frac{\alpha_e + \alpha_o + \Phi}{\alpha_e + \alpha_o} \right] = 2 \left[1 + \frac{2}{3} \frac{\lambda_{eo}}{\lambda_e + \lambda_o} \right]. \quad (4.14)$$

For $\lambda_e = \lambda_o = \lambda_{eo}$, Eq. (4.14) reproduces the value $R=8/3$ known for the two-channel, fully screened $S=1$ Kondo model [25]. If however $\lambda_{eo}=0$ we get $R=2$, in agreement with the text-book result for two not necessarily identical but independent replicas of the single channel Kondo model.

4.4 Charge Current

The current operator at position x is expressed in terms of first-quantized operators ψ attributed to the linear combinations of the Fermi operators in the leads

$$\hat{I}(x) = \frac{e\hbar}{2mi} \sum_{\sigma} \left[\psi_{\sigma}^{\dagger}(x) \partial_x \psi_{\sigma}(x) - \partial_x \psi_{\sigma}^{\dagger}(x) \psi_{\sigma}(x) \right]. \quad (4.15)$$

In the present case both types of quasi-particles $b_{a\sigma}$ ($a=e, o$) interact with the dot. Besides, both scattering phases (e/o) are close to their resonance value $\delta_{0,\sigma}^{e/o} = \pi/2$. This is in striking contrast to the single channel Kondo model, where one of the eigenvalues of the 2×2 matrix of $J_{\alpha\alpha'}$ in Eq. (4.5) is zero, and hence the corresponding degree of freedom is completely decoupled in the interacting regime. For the sake of simplicity, we are going to consider the 2SK problem in the absence of an orbital magnetic field so that magnetic flux is zero. However, our results can be easily generalized for the case of finite orbital magnetic field. In this section we obtain an expression of charge current operator for the two-stage Kondo problem following the spirit of seminal works [106, 107, 151, 152]. The principal idea behind the non-equilibrium calculations is to choose a basis of scattering states for the expansion of the current operator Eq.(4.15). The scattering states in the first quantization representation are expressed as

$$\psi_{ek\sigma}(x) = \frac{1}{\sqrt{2}} \begin{cases} [e^{i(k_F+k)x} - S_{e,\sigma}(k)e^{-i(k_F+k)x}] & x < 0 \\ [e^{-i(k_F+k)x} - S_{e,\sigma}(k)e^{i(k_F+k)x}] & x > 0 \end{cases}$$

$$\psi_{ok\sigma}(x) = \frac{1}{\sqrt{2}} \begin{cases} [e^{i(k_F+k)x} - S_{o,\sigma}(k)e^{-i(k_F+k)x}] & x < 0 \\ [-e^{-i(k_F+k)x} + S_{o,\sigma}(k)e^{i(k_F+k)x}] & x > 0 \end{cases}$$

The phase shifts in even/odd channels are defined through the corresponding S -matrix via the relation $S_{a,\sigma}(k)=e^{2i\delta_\sigma^\alpha(\epsilon_k)}$. Proceeding to second quantization, we project the operator $\psi_\sigma(x)$ over the eigenstates $\psi_{ek\sigma}(x)$ and $\psi_{ok\sigma}(x)$, choosing $x < 0$ far from the dot, to arrive at the expression

$$\psi_\sigma(x)=\frac{1}{\sqrt{2}}\sum_{k\sigma}\left[\left(e^{i(k_F+k)}-S_{e,\sigma}(k)e^{-i(k_F+k)}\right)b_{ek\sigma}+\left(e^{i(k_F+k)}-S_{o,\sigma}(k)e^{-i(k_F+k)}\right)b_{ok\sigma}\right]. \quad (4.16)$$

Substituting Eq. (4.16) into Eq. (4.15) and using

$$b_{a\sigma}(x)=\sum_k b_{ak\sigma}e^{ikx}, \quad S b_{a\sigma}(x)=\sum_k S(k)b_{ak\sigma}e^{ikx},$$

we obtain an expression for the current for symmetrical dot-leads coupling,



Figure 4.3: Left panel: Feynman codex used for the representation of different Greens functions: blue (red) line (in the black and white printout the colors are different by intensity of gray (red is more intensive)) for Green function of even (odd) channel $G_{e(o)}$ and the mixed line for the mixed Green function G_{eo} (see definition in Section 4.4.2). Right panel: two-particle elastic vertices for even and odd channels. Crosses denote energy-dependent scattering.

$$\hat{I}(x)=\frac{e}{2h\nu}\sum_{\sigma}\left[b_{o\sigma}^\dagger(x)b_{e\sigma}(x)-b_{o\sigma}^\dagger(-x)\mathcal{S}b_{e\sigma}(-x)+\text{H.c.}\right], \quad (4.17)$$

where $\mathcal{S}=S_o^*S_e$. There are two contributions to the charge current, coming from elastic and inelastic processes. The elastic effects are characterized by the energy-dependent phase-shifts, the inelastic ones are due to the interaction of Fermi-liquid quasi-particles. In the following section we outline the elastic and inelastic current contribution of two-stage Kondo model Eq. (4.10).

4.4.1 Elastic current

We assume that the left and right scattering states are in thermal equilibrium at temperature $T_L=T_R=T$ and at the chemical potentials μ_R and $\mu_L=\mu_R+eV$. The population of states reads $2\langle b_{ak\sigma}^\dagger b_{ak'\sigma}\rangle=\delta_{kk'}[f_L(\epsilon_k)+f_R(\epsilon_k)]$ and $2\langle b_{ak\sigma}^\dagger b_{\bar{a}k'\sigma}\rangle=\delta_{kk'}[f_L(\epsilon_k)-f_R(\epsilon_k)]=\delta_{kk'}\Delta f(\epsilon_k)$, with $f_{L/R}(\epsilon_k)=f(\epsilon_k-\mu_{L/R})$ and $f(\epsilon_k)=(1+\exp[\epsilon_k/T])^{-1}$ is the Fermi distribution function. The zero temperature conductance in the absence of bias voltage is [29]

$$G(T=0, B\neq 0, V=0)/G_0=B^2(\alpha_e-\alpha_o)^2. \quad (4.18)$$

The elastic current in the absence of Zeeman field B is the expectation value of the current operator Eq. (4.17). Taking the expectation value of Eq. (4.17) reproduces the Landauer-Büttiker equation [59]

$$I_{\text{el}}=\frac{2e}{h}\int_{-\infty}^{\infty}d\epsilon T(\epsilon)\Delta f(\epsilon), \quad (4.19)$$

where the energy dependent transmission coefficient, $T(\varepsilon) = \frac{1}{2} \sum_{\sigma} \sin^2(\delta_{\sigma}^e(\varepsilon) - \delta_{\sigma}^o(\varepsilon))$ and $\Delta f(\varepsilon) = f_L(\varepsilon) - f_R(\varepsilon)$. Diagrammatically (see Ref. [24] and Ref. [147] for details), the elastic corrections to the current can be reabsorbed into a Taylor expansion for the energy-dependent phase shifts through the purely elastic contributions to quasi-particles self-energies [24]. That is the scattering phase-shifts can be read off [24] via the real part of the retarded self-energies $\Sigma_{a,\sigma}^R(\varepsilon)$ (see Fig. 4.3) as

$$\delta_{\sigma}^a(\varepsilon) = -\pi\nu \text{Re}\Sigma_{a,\sigma}^R(\varepsilon) = \pi/2 + \alpha_a \varepsilon. \quad (4.20)$$

The Kondo temperatures of the two-channels in the strong-coupling limit are defined as

$$T_K^a = \frac{1}{\alpha_a}. \quad (4.21)$$

This definition is consistent with Nozieres-Blandin [22] and identical to that used in [147], however, is differ by the coefficient $\pi/4$ from the spin-susceptibility based definition [149]. The elastic phase-shifts in the presence of the finite Zeeman field B bears the form [29] (see schematic behaviour of $\delta_{\downarrow}^a(B)$ in Fig. 4.4)

$$\delta_{\sigma}^a(B) = \pi/2 - (\alpha_a + \phi_a + \Phi)\bar{\sigma}B/2. \quad (4.22)$$

Finally, we expand Eq. (4.19) up to second order in α_a to get the elastic contribution to the current

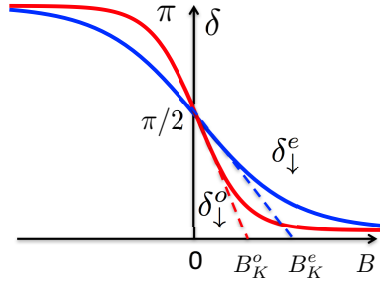


Figure 4.4: Schematic behaviour of the even (blue) and odd (red) scattering phases at $\sigma = \downarrow$ as a function of the Zeeman magnetic field. Both phases approach the resonance value $\pi/2$ at zero field. The tangential lines illustrate corresponding energy scales inversely proportional to the spin susceptibilities (4.13) in the even/odd channels, $B_K^a = \pi/(2\alpha_a + \Phi)$ (see also Eqs.(4.20)-(4.22)).

[151],

$$\frac{I_{\text{el}}}{2e^2V/h} = \left[B^2 + \frac{(eV)^2}{12} + \frac{(\pi T)^2}{3} \right] (\alpha_e - \alpha_o)^2. \quad (4.23)$$

The B^2 elastic term is attributed to the Zeeman field in Eq. (4.1). Note that we do not consider the orbital effects assuming that the magnetic field is applied parallel to the plane of the electron gas. The expression Eq. (4.23) remarkably highlights the absence of a linear response at $T=0$, $B=0$, due to the vanishing of conductance when both scattering phases achieve the resonance value $\pi/2$. The current is exactly zero at the symmetry point $\alpha_e = \alpha_o$ [29] due to the diagonal form of S -matrix characterized by two equal eigen values and therefore proportional to the unit matrix.

4.4.2 Inelastic current

To calculate the inelastic contribution to the current we apply the perturbation theory using Keldysh formalism [115],

$$\delta I_{\text{in}} = \langle T_C \hat{I}(t) e^{-i \int dt' H_{\text{int}}(t')} \rangle, \quad (4.24)$$

where $H_{\text{int}} = H_\phi + H_\Phi$ and C denotes the double-side $\eta = \pm$ Keldysh contour. Here T_C is corresponding time-ordering operator. The average is performed with the Hamiltonian H_0 . The effects associated with quadratic Hamiltonian H_α are already accounted in I_{el} . Therefore, to obtain the second-order correction to the inelastic current we proceed by considering $H_{\text{int}} = H_\phi + H_\Phi$, with the Feynman diagrammatic codex as shown in Fig. 4.5.

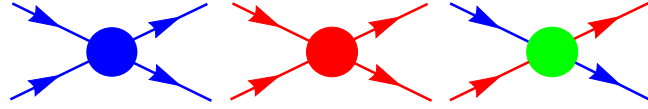


Figure 4.5: Feynman diagrammatic codex used for the calculation of inelastic current. Blue (red) circles denote the density-density intra-channel interaction in even (odd) channel respectively (see Eq. 4.10). Green circle denotes the inter-channel spin-spin interaction Eq. 4.10.

The perturbative expansion of Eq. (4.24) in $(B, T, eV) \ll T_K^0$ starts with the second-order contribution [24] and is illustrated by Feynman diagrams of four types (see Fig. 4.6). The type-1 and type-2 diagrams contain only one mixed Green's function, GF (dashed line) proportional to $\Delta f(t) \sim eV$, where $\Delta f(t)$ is the Fourier transform of $\Delta f(\varepsilon)$ defined in Eq. (4.73). Therefore, both diagrams fully define the linear-response contribution to the inelastic current, but also contain some non-linear $\propto (eV)^3$ contributions. The type-1 diagram contains the mixed GF directly connected to the current vertex (Fig. 4.6) and can be expressed in terms of single-particle self-energies. The type-2 diagram contains the mixed GF completely detached from the current vertex and therefore can not be absorbed into self-energies. We will refer to this topology of Feynman diagram as a vertex correction. Note, that the second-order Feynman diagrams containing two (and also four) mixed GF are forbidden due to PH symmetry of the problem. The type-3 and type-4 diagrams contain three mixed GF's and therefore contribute only to the non-linear response being proportional to $(eV)^3$. The type-3 diagram, similarly to the type-1 diagram, can be absorbed into the single-particle self-energies. The type-4 diagram, similarly to the type-2 diagram is contributing to the vertex corrections. This classification can be straightforwardly extended to higher order perturbation corrections for the current operator. Moreover, the diagrammatic series will have similar structure also for the Hamiltonians without particle-hole symmetry where more vertices are needed to account for different types of interactions. A similar classification can also be done for current-current (noise) correlation functions. The mathematical details of the computation of the diagrammatic contribution of current correction diagrams type-1, type-2, type-3 and type-4 as shown in Fig. 4.6 proceed as follows:

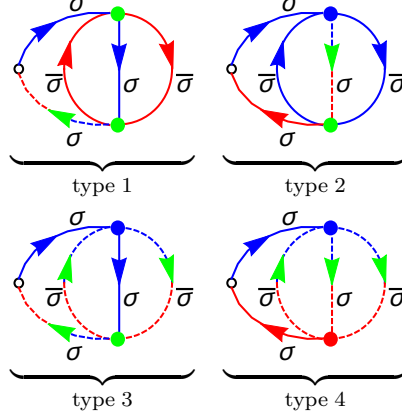


Figure 4.6: Examples of four different types of Feynman diagrams contributing to the inelastic current. The open circle represents the current vertex. The other notations have been defined in Fig. 4.3 and Fig. 4.5.

Evaluation of type-1 diagram

The straightforward calculation of the Keldysh GFs at $x = 0$ takes the form (see Refs. [1, 106] for details)

$$G_{aa}(k, \varepsilon) = \frac{1}{\varepsilon - \varepsilon_k} \tau_z + i\pi \begin{pmatrix} F_0 & F_0 + 1 \\ F_0 - 1 & F_0 \end{pmatrix} \delta(\varepsilon - \varepsilon_k),$$

$$\mathcal{G}_{ba/ab}(k, \varepsilon) = i\pi \begin{pmatrix} 1 & 1 \\ 1 & 1 \end{pmatrix} \Delta f(k, \varepsilon) \delta(\varepsilon - \varepsilon_k), \quad (4.25)$$

where $F_0 = f_L + f_R - 1$ and the Pauli matrix $\tau_z = \begin{pmatrix} 1 & 0 \\ 0 & -1 \end{pmatrix}$. The current contribution proportional to Φ^2 corresponding to the diagram of type-1 as shown in Fig. 4.6 is given by [106]

$$\delta I_{\text{int}}^{\Phi^2} = \frac{e}{\nu \hbar} \sum_{\eta_1, \eta_2} \eta_1 \eta_2 \times \mathcal{Y}_1^{\eta_1, \eta_2}, \quad (4.26)$$

with

$$\mathcal{Y}_1^{\eta_1, \eta_2} = \int \frac{d\varepsilon}{2\pi} [i\mathcal{S} G_{ee}^{+\eta_1}(-x, \varepsilon) \Sigma^{\eta_1 \eta_2}(\varepsilon) G_{eo}^{\eta_2 -}(x, \varepsilon) + \text{c.c.}],$$

where $\mathcal{S} = S_o^* S_e$, $\eta_{1/2}$ are the Keldysh branch indices which takes the value of + or -. The self-energy $\Sigma^{\eta_1 \eta_2}$ in real time is

$$\Sigma^{\eta_1 \eta_2}(t) = \left(\frac{\Phi}{\pi \nu^2} \right)^2 \sum_{k_1, k_2, k_3} G_{ee}^{\eta_1 \eta_2}(k_1, t) G_{ee}^{\eta_2 \eta_1}(k_2, -t) G_{ee}^{\eta_1 \eta_2}(k_3, t). \quad (4.27)$$

Using Eq. (4.25) we express the diagonal and mixed GFs in real space as

$$G_{aa}^{\eta_1 \eta_2}(\alpha x, \varepsilon) = i\pi \nu e^{i\alpha \varepsilon x / v_f} \left[F_0 + \begin{cases} \eta_1, & \text{if } \alpha = 1 \\ -\eta_2, & \text{if } \alpha = -1 \end{cases} \right],$$

$$G_{a\bar{a}}^{\eta_1 \eta_2}(x, \varepsilon) = i\pi \nu e^{i\varepsilon x / v_f} \Delta f(\varepsilon), \quad (4.28)$$

The expression of corresponding GFs in real time is obtained by writing the Fourier transform of $(F_0(\varepsilon) \pm 1)$ as follows:

$$= \int \frac{d\varepsilon}{2\pi} (F_0(\varepsilon) \pm 1) e^{-i\varepsilon t} = \frac{i}{2\pi} \left[\pm \frac{\pi T}{\sinh(\pi T t)} (e^{-i\mu_L t} + e^{-i\mu_R t}) - 2 \frac{e^{\pm i D t}}{t} \right]. \quad (4.29)$$

Summing Eq. (4.26) over η_1 and η_2 using Eq. (4.28) results in two terms involving $\Sigma^{++} - \Sigma^{--}$ and $\Sigma^{-+} - \Sigma^{+-}$. The first term produces the contribution which is proportional to model cut-off D , which can be eliminated by introducing the counter terms in the Hamiltonian Eq. (4.68). In rest of the calculation we consider only the contribution which is finite for $D \rightarrow \infty$. As a result we get

$$\delta I_{\text{int}}^{\Phi^2} = \frac{2e\pi}{h} \int \frac{d\varepsilon}{2\pi} (\Sigma^{-+}(\varepsilon) - \Sigma^{+-}(\varepsilon)) i\pi\nu \Delta f(\varepsilon). \quad (4.30)$$

In Eq. (4.30) we used $\mathcal{S} + \mathcal{S}^* = 2 \cos(\delta_{0,\sigma}^e - \delta_{0,\sigma}^o) = 2$ with $\delta_{0,\sigma}^e = \delta_{0,\sigma}^o = \pi/2$. Fourier transformation of Eq. (4.30) into real time takes the form

$$\delta I_{\text{int}}^{\Phi^2} = \frac{2e\pi}{h} \int dt (\Sigma^{-+}(t) - \Sigma^{+-}(t)) i\pi\nu \Delta f(-t). \quad (4.31)$$

From Eq. (4.29) the required Greens function in real time are

$$G_{aa}^{+-}(t) = -\pi\nu T \frac{\cos(\frac{eV}{2}t)}{\sinh(\pi T t)}, \quad (4.32)$$

$$G_{eo}(t) = i\pi\nu T \frac{\sin(\frac{eV}{2}t)}{\sinh(\pi T t)}. \quad (4.33)$$

The Greens function $G_{aa}^{-+}(t)$ is related with that of $G_{aa}^{+-}(t)$ by causality identity. The self-energies in Eq. (4.31) are accessible by using above Greens functions Eqs. (4.32) and (4.33) into self energy Eq. (4.27). Then Eq. (4.31) results in

$$\delta I_{\text{int}}^{\Phi^2} = \frac{2e\pi}{h} \left(\frac{\phi_e}{\pi\nu^2} \right)^2 \times 2i(\pi\nu T)^4 \int dt \frac{\cos^3(\frac{eV}{2}t) \sin(\frac{eV}{2}t)}{\sinh^4(\pi T t)}. \quad (4.34)$$

The integral Eq. (4.34) is calculated in Appendix 4.E. Hence the interaction correction to the current corresponding to the type-1 diagrams shown in Fig. 4.6 is

$$\frac{\delta I_{\text{type-1}}^{\Phi^2}}{2e^2 V/h} = \left[A_V^{(1)} (eV)^2 + A_T^{(1)} (\pi T)^2 \right] \Phi^2, \quad (4.35)$$

where $A_V^{(1)} = 5/12$ and $A_T^{(1)} = 2/3$. Alternatively, for the calculation of the integral Eq. (4.30) one can proceed with scattering T-matrix formalism. The single particle self energy difference associated with the diagram of type-1 is expressed in terms of inelastic T-matrix to obtain [1, 29]

$$\Sigma^{-+}(\varepsilon) - \Sigma^{+-}(\varepsilon) = \frac{\Phi^2}{i\pi\nu} \left[\frac{3}{4} (eV)^2 + \varepsilon^2 + (\pi T)^2 \right]. \quad (4.36)$$

Using this self-energy difference and following the same way as we computed elastic current in Appendix 4.C, one easily get the final expression for the current correction contributed by the diagram of type-1.

Evaluation of type-2 diagram

The diagrammatic contribution of the type-2 diagram shown in Fig. 4.6 proportional to $\phi_e \Phi$ given by

$$\delta I_{\text{int}}^{\phi_e \Phi} = \frac{e}{\nu h} \mathcal{J} = \frac{e}{\nu h} \sum_{\eta_1, \eta_2} \eta_1 \eta_2 \mathcal{Y}_2^{\eta_1, \eta_2}, \quad (4.37)$$

with

$$\mathcal{Y}_2^{\eta_1, \eta_2} = \int \frac{d\varepsilon}{2\pi} [i\mathcal{S} G_{ee}^{+\eta_1}(-x, \varepsilon) \Lambda_1^{\eta_1 \eta_2}(\varepsilon) G_{oo}^{\eta_2-}(x, \varepsilon) + \text{c.c.}].$$

The self energy part Λ_1 in real time is expressed as

$$\Lambda_1^{\eta_1 \eta_2}(t) = \frac{\phi_e \Phi}{(\pi\nu^2)^2} \sum_{k_1, k_2, k_3} G_{ee}^{\eta_1 \eta_2}(k_1, t) G_{ee}^{\eta_2 \eta_1}(k_2, -t) G_{eo}^{\eta_1 \eta_2}(k_3, t). \quad (4.38)$$

Now using Eq. (4.28) into Eq. (4.37) followed by the summation over Keldysh indices, we get

$$\mathcal{J} = 2i\mathcal{S}(\pi\nu)^2 \int dt [(F_0 + 1)(t) \Lambda_1^{-+}(-t) - (F_0 - 1)(t) \Lambda_1^{+-}(-t)] + \text{c.c.} \quad (4.39)$$

Let us define the Greens function as $G_{ee}^{+/-+}(t) = G_{oo}^{+/-+}(t) \equiv G^{+/-+}(t)$. Then we write

$$i\pi\nu(F_0 \pm 1)(t) = G^{+/-+}(t), \quad (4.40)$$

where $(F_0 \pm 1)(t)$ is a shorthand notation for the Fourier transform of $F_0(\varepsilon) \pm 1$ defined by (4.29). Hence, Eq. (4.39) takes the form

$$\mathcal{J} = 2\mathcal{S}\pi\nu \int dt [G^{+-}(t) \Lambda_1^{-+}(-t) - G^{-+}(t) \Lambda_1^{+-}(-t)] + \text{c.c.} \quad (4.41)$$

Now the self energies in Eq. (4.38) cast the compact form

$$\Lambda_1^{\eta_1 \eta_2}(-t) = \frac{\phi_e \Phi}{(\pi\nu^2)^2} G^{\eta_1 \eta_2}(-t) G^{\eta_2 \eta_1}(t) G_{eo}(-t). \quad (4.42)$$

Then the Eq. (4.41) becomes

$$\mathcal{J} = 4\mathcal{S}\pi\nu \frac{\phi_e \Phi}{(\pi\nu^2)^2} \int dt [G^{+-}(t)]^3 G_{eo}(t) + \text{c.c.} \quad (4.43)$$

Using the explicit expressions of the Greens functions Eqs. (4.32) and (4.33) together with Eq. (4.43) leads to

$$\mathcal{J} = -4i(\pi\nu)^2 \mathcal{S}T(\pi\nu T)^3 \frac{\phi_e \Phi}{(\pi\nu^2)^2} \int dt \frac{\cos^3(\frac{eV}{2}t) \sin(\frac{eV}{2}t)}{\sinh^4(\pi Tt)}. \quad (4.44)$$

Substituting the value of integral given by Eq. (4.89) into Eq. (4.44) and using Eq. (4.37) we get

$$\frac{\delta I_{\text{type-2}}^{\phi_e \Phi}}{2e^2 V/h} = [A_V^{(2)}(eV)^2 + A_T^{(2)}(\pi T)^2] \phi_e \Phi, \quad (4.45)$$

where $A_V^{(2)} = -5/6$ and $A_T^{(2)} = -4/3$.

Evaluation of type-3 diagram

Here we calculate the contribution to the current given by the diagram which consists of the self energy with two mixed Greens functions and one diagonal Greens function (type-3 diagram). The diagram shown in Fig. 4.6 describes correction proportional to $\phi_e\Phi$ and is given by

$$\delta I_{\text{int}}^{\phi_e\Phi} = \frac{e}{\nu h} \sum_{\eta_1, \eta_2} \eta_1 \eta_2 \mathcal{Y}_3^{\eta_1, \eta_2}, \quad (4.46)$$

with

$$\mathcal{Y}_3^{\eta_1, \eta_2} = \int \frac{d\varepsilon}{2\pi} [i\mathcal{S}G_{ee}^{+\eta_1}(-x, \varepsilon)\Lambda_2^{\eta_1\eta_2}(\varepsilon)G_{eo}^{\eta_2-}(x, \varepsilon) + \text{c.c.}].$$

The self-energy $\Lambda_2^{\eta_1\eta_2}$ in real time is

$$\Lambda_2^{\eta_1\eta_2}(t) = \frac{\phi_e\Phi}{(\pi\nu^2)^2} \sum_{k_1, k_2, k_3} G_{eo}^{\eta_1\eta_2}(k_1, t)G_{oe}^{\eta_2\eta_1}(k_2, -t)G_{ee}^{\eta_1\eta_2}(k_3, t). \quad (4.47)$$

Summing Eq. (4.46) over η_1 and η_2 using Eq. (4.28), we get

$$\delta I_{\text{int}}^{\phi_e\Phi} = -\frac{e}{\nu h} \times \pi\nu\mathcal{S} \int \frac{d\varepsilon}{2\pi} (\Lambda_2^{-+}(\varepsilon) - \Lambda_2^{+-}(\varepsilon)) i\pi\nu\Delta f(\varepsilon) + \text{c.c.} \quad (4.48)$$

The Fourier transformation of Eq. (4.48) into real time gives

$$\delta I_{\text{int}}^{\phi_e\Phi} = -\frac{e}{\nu h} \times \pi\nu\mathcal{S} \int dt (\Lambda_2^{-+}(t) - \Lambda_2^{+-}(t)) i\pi\nu\Delta f(-t) + \text{c.c.} \quad (4.49)$$

Using the expressions of Greens functions in real time Eq. (4.32) and Eq. (4.33) allows to bring the interaction correction to the current Eq. (4.49) to a compact form

$$\delta I_{\text{int}}^{\phi_e\Phi} = \frac{2e\pi}{h} \times 2i(\pi\nu T)^4 \frac{\phi_e\Phi}{(\pi\nu^2)^2} \int dt \frac{\cos(\frac{eV}{2}t) \sin^3(\frac{eV}{2}t)}{\sinh^4(\pi Tt)}. \quad (4.50)$$

Using Eq. (4.92) into Eq. (4.50) we get

$$\frac{\delta I_{\text{type-3}}^{\phi_e\Phi}}{2e^2V/h} = [A_V^{(3)}(eV)^2 + A_T^{(3)}(\pi T)^2] \phi_e\Phi,$$

where $A_V^{(3)} = -1/4$ and $A_T^{(3)} = 0$.

Evaluation of type-4 diagram

In this Section we calculate the diagrammatic contribution of the $\phi_e\phi_o$ current diagrams (type-4 diagram) shown in Fig. 4.6. Similar to type-2 diagram calculation, the current correction reads

$$\delta I_{\text{int}}^{\phi_e\phi_o} = \frac{e}{\nu h} \mathcal{L} = \frac{e}{\nu h} \sum_{\eta_1, \eta_2} \eta_1 \eta_2 \mathcal{Y}_4^{\eta_1, \eta_2}, \quad (4.51)$$

with

$$\mathcal{Y}_4^{\eta_1, \eta_2} = \int \frac{d\varepsilon}{2\pi} [i\mathcal{S}G_{ee}^{+\eta_1}(-x, \varepsilon)\Lambda_3^{\eta_1\eta_2}(\varepsilon)G_{oo}^{\eta_2-}(x, \varepsilon) + \text{c.c.}]. \quad (4.52)$$

The self-energy part $\Lambda_3^{\eta_1\eta_2}$ is given by the expression

$$\Lambda_3^{\eta_1\eta_2}(t) = \frac{\phi_e\phi_o}{(\pi\nu^2)^2} \sum_{k_1, k_2, k_3} G_{oe}^{\eta_1\eta_2}(k_1, t) G_{eo}^{\eta_2\eta_1}(k_2, -t) G_{eo}^{\eta_1\eta_2}(k_3, t). \quad (4.53)$$

Now substituting Eq. (4.28) into Eq. (4.52) followed by the summation over Keldysh indices, we get

$$\mathcal{L} = 2i\mathcal{S}(\pi\nu)^2 \int dt [(F_0 + 1)(t)\Lambda_3^{-+}(-t) - (F_0 - 1)(t)\Lambda_3^{+-}(-t)] + \text{c.c.} \quad (4.54)$$

Plugging in Eq. (4.40) into Eq. (4.54) results

$$\mathcal{L} = 2\mathcal{S}\pi\nu \int dt [G^{+-}(t)\Lambda_3^{-+}(-t) - G^{-+}(t)\Lambda_3^{+-}(-t)] + \text{c.c.} \quad (4.55)$$

The self-energy Eq. (4.55) takes the form

$$\Lambda_3^{-+}(-t) = \frac{\phi_e\phi_o}{(\pi\nu^2)^2} [G_{eo}(t)]^3 = \Lambda_3^{+-}(-t). \quad (4.56)$$

Hence combining Eq. (4.32) and Eq. (4.33) we bring the required integral Eq. (4.55) to the form

$$\mathcal{L} = -\frac{\phi_e\phi_o}{(\pi\nu^2)^2} \times 4i\mathcal{S}\pi\nu(\pi\nu T)^4 \int dt \frac{\cos(\frac{eV}{2}t) \sin^3(\frac{eV}{2}t)}{\sinh^4(\pi Tt)} + \text{c.c.} \quad (4.57)$$

The integral in Eq. (4.57) is given by Eq. (4.92). Hence plugging in Eq. (4.57) into Eq. (4.51) we obtain the current correction:

$$\frac{\delta I_{\text{type-4}}^{\phi_e\phi_o}}{2e^2V/h} = [A_V^{(4)}(eV)^2 + A_T^{(4)}(\pi T)^2] \phi_e\phi_o, \quad (4.58)$$

where $A_V^{(4)} = 1/2$ and $A_T^{(4)} = 0$. As we discussed above, all the current diagrams are of the form of type-1, type-2, type-3 and type-4. However, same type of diagrams may contain different numbers of fermionic loops and also different spin combinations. In addition, there is the renormalization factor of $-\frac{1}{2}$ in H_Φ , which has to be accounted for the diagrams containing at least one Φ vertex. Same type of diagrams containing at least one Φ vertex with different spin combination have the different weight factor because of product of Pauli matrices in H_Φ . Each fermionic loop in the diagrams results in extra (-1) multiplier in the corresponding weight factor. These facts will be accounted for by assigning the weight to the given current diagram (e.g. as shown in Fig. 4.7, Fig. 4.8 and Fig. 4.9). However, in these equations proper weight factors which emerge from (i) the number of closed fermionic loops, (ii) SU(2) algebra of Pauli matrices and (iii) additional factors originating from the definition of the FL constants in the Hamiltonian (the extra factor of $-1/2$ in H_Φ) are still missing and are accounted for separately. As a result our final expression for the second-order perturbative interaction corrections to the current is given by (see Appendix 4.D)

$$\begin{aligned} \frac{\delta I_{\text{in}}}{2e^2V/h} &= \left[\frac{2}{3}(\phi_e^2 + \phi_o^2) + 3\Phi^2 - 2(\phi_e + \phi_o)\Phi \right] (\pi T)^2 \\ &+ \left[\frac{5}{12}(\phi_e^2 + \phi_o^2) + 3\Phi^2 - 2(\phi_e + \phi_o)\Phi \right. \\ &\left. + \frac{1}{2}\phi_e\phi_o \right] (eV)^2. \end{aligned} \quad (4.59)$$

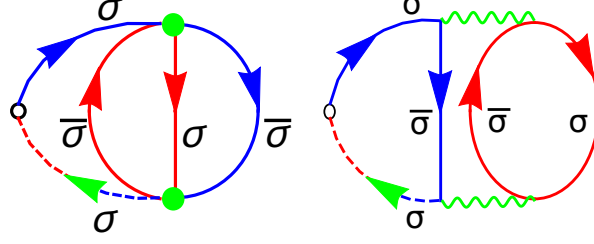


Figure 4.7: The Φ^2 type-1 diagram (Left panel) and the corresponding diagram with the splitting of local Φ vertices (Right panel). In the diagram the upper Φ vertex consist in the Pauli matrices product $\tau_{\sigma\bar{\sigma}} \cdot \tau_{\bar{\sigma}\sigma} = 2$. Similarly the lower Φ vertex contain the product of $\tau_{\bar{\sigma}\sigma} \cdot \tau_{\sigma\bar{\sigma}} = 2$. The diagram contains an even number of fermionic loops (two) and hence no extra negative sign occur due to the fermionic loop. Each Φ vertex has the renormalization factor of $-\frac{1}{2}$. Hence the overall weight factor of this diagram is $\frac{1}{4} \times 4$ as will be seen in Fig. 11 and Fig. 12 given in the Appendix.

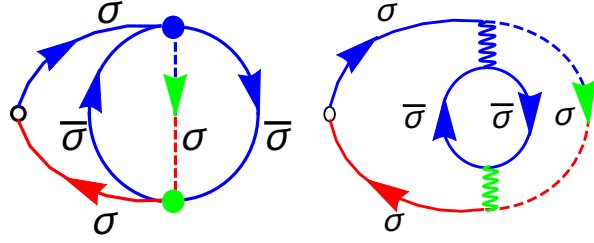


Figure 4.8: The $\phi_e \Phi$ type-2 current correction diagram (Left panel) and the corresponding diagram with the splitting of local Φ vertices (Right panel). In the diagram the Φ vertex consist in the Pauli matrices product $\tau_{\sigma\sigma} \cdot \tau_{\bar{\sigma}\bar{\sigma}} = -1$. The diagram contain an even number of fermionic loops (two) and hence no extra negative sign occur due to the fermionic loop. The Φ vertex has the renormalization factor of $-\frac{1}{2}$. Hence the overall weight factor of this diagram is $-\frac{1}{2} \times (-1)$ as will be seen in Fig. 11 and Fig. 12.

The first term $\propto (\pi T)^2$ in Eq. (4.59) is the linear response result given by type-1 and type-2 diagrams. The second term (surviving also at $T = 0$) is the non-linear response contribution arising from all type 1-4 diagrams. The inelastic current Eq. (4.59) vanishes at the symmetry point. Moreover the linear response and the non-linear response contributions vanish at the symmetry point independently. Also the elastic and inelastic currents approach zero separately when the system is fine-tuned to the symmetry point. These properties will be reproduced in arbitrary order of perturbation theory.

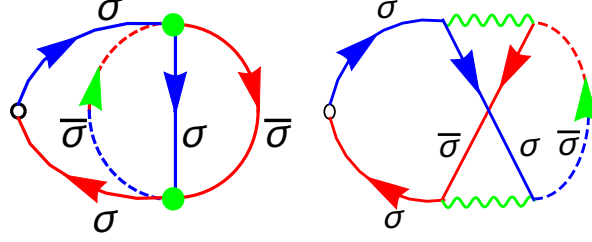


Figure 4.9: The Φ^2 type-2 current correction diagram (Left panel) and the corresponding diagram with the splitting of local Φ vertices (Right panel). In the diagram the upper Φ vertex consist in the Pauli matrices product $\tau_{\sigma\sigma} \cdot \tau_{\bar{\sigma}\bar{\sigma}} = -1$. Similarly the lower Φ vertex contain the product of $\tau_{\bar{\sigma}\sigma} \cdot \tau_{\sigma\bar{\sigma}} = 2$. The diagram contain no fermionic loops and hence no extra negative sign occur due to the fermionic loop. Each Φ vertex has the renormalization factor of $-\frac{1}{2}$. Hence the overall weight factor of this diagram is $\frac{1}{4} \times (-2)$ as will be seen in Fig. 11 and Fig. 12

4.5 Transport properties

The total current consists of the sum of elastic and inelastic parts which upon using the FL-identity $\alpha_a = \phi_a$ takes the form

$$\begin{aligned} \frac{\delta I}{2e^2 V/h} &= [(\pi T)^2 + (eV)^2] 3\left(\Phi - \frac{2}{3}\alpha_e\right)\left(\Phi - \frac{2}{3}\alpha_o\right) \\ &+ \left[B^2 + (\pi T)^2 + \frac{1}{2}(eV)^2\right] (\alpha_e - \alpha_o)^2. \end{aligned} \quad (4.60)$$

This Eq. (4.60) constitutes the main result of this work where the second term describes universal behaviour [29] scaled with $(1/T_K^e - 1/T_K^o)^2$, while the first one, containing an extra dependence on the ratio T_K^o/T_K^e accounts for the non-universality associated with the lack of conformal symmetry away from the symmetry-protected points. The Eq. (4.60) demonstrates the magnetic field B , temperature T and voltage V behaviour of the charge current characteristic for the Fermi-liquid systems. Therefore, following [147] we introduce general FL constants as follows:

$$\frac{1}{G_0} \frac{\partial I}{\partial V} = c_B B^2 + c_T (\pi T)^2 + c_V (eV)^2. \quad (4.61)$$

$$\frac{c_T}{c_B} = 1 + 3\mathcal{F}, \quad \frac{c_V}{c_B} = \frac{3}{2} + 9\mathcal{F}. \quad (4.62)$$

Here the parameter

$$\mathcal{F} = \frac{(\Phi - \frac{2}{3}\alpha_e)(\Phi - \frac{2}{3}\alpha_o)}{(\alpha_e - \alpha_o)^2} = \frac{4(\lambda_{eo} - \lambda_e)(\lambda_{eo} - \lambda_o)}{9(\lambda_e - \lambda_o)^2}. \quad (4.63)$$

The parameter \mathcal{F} vanishes in the limit of strong asymmetry, $\lambda_{eo} \ll \lambda_e \ll \lambda_o$ in which the ratios

$$c_T/c_B|_{\lambda_{eo} \ll \lambda_e \ll \lambda_o} = 1, \quad c_V/c_B|_{\lambda_{eo} \ll \lambda_e \ll \lambda_o} = 3/2 \quad (4.64)$$

correspond to the universality class of the single-channel Kondo model [29, 49].

On the other hand, near the symmetry point $\lambda_e=\lambda_o=\lambda_{eo}$, the function \mathcal{F} evidently depends sensitively on the precise manner in which the symmetry point is approached. In fact, *a priori* it appears unclear whether \mathcal{F} even reaches a well-defined value at this point. To clarify this, additional information on the parameters λ_e , λ_o and λ_{eo} is required.

In full generality, the three parameters λ_e , λ_o and λ_{eo} of the FL theory are independent from each other. Nonetheless, we are considering here a specific Hamiltonian Eq. (4.6) with only two independent parameters J_e and J_o , which implies that λ_{eo} is in fact a function of λ_e and λ_o . Although the corresponding functional form is not known, it can be deduced in the vicinity of the symmetric point $\lambda_e=\lambda_o=\lambda_{eo}$ from the following argument: the obvious $e \leftrightarrow o$ symmetry imposes that the Wilson ratio $R=8/3$ is an extremum at the symmetric point (see Fig. 4.10), or else said, that its derivative with respect to the channel imbalance ratio λ_o/λ_e vanishes. The only expression compatible with this requirement and the $e \leftrightarrow o$ symmetry is $\lambda_{eo}=(\lambda_e+\lambda_o)/2$, valid in the immediate vicinity of the symmetry point. Inserting this dependence in Eq. (4.63) predicts $\lim_{\lambda_e \rightarrow \lambda_o} \mathcal{F} = -1/9$ at the symmetric point, and

$$c_T/c_B|_{\lambda_{eo}=\lambda_e=\lambda_o} = 2/3, \quad c_V/c_B|_{\lambda_{eo}=\lambda_e=\lambda_o} = 1/2. \quad (4.65)$$

To summarize, under the assumption that the Wilson ratio is maximal at the symmetry point, we have arrived at the following conclusion: as the degree of asymmetry is reduced, i.e. the ratios λ_e/λ_o and λ_{eo}/λ_e increased from 0 to 1, the ratios of Fermi liquid coefficients c_T/c_B and c_V/c_B decrease from the maximal values of Eq. (4.64), to the minimal values of Eq. (4.65), characteristic of the 1CK and 2SK fixed points, respectively.

4.6 Summary

We constructed a Fermi-liquid theory of a two-channel, two-stage Kondo model when both scattering channels are close to the resonance. This theory completely describes the transport in in- and out-of-equilibrium situation of the 2SK model. The elastic and inelastic contributions to the charge current through the 2SK model have been calculated using the full-fledged non-equilibrium Keldysh formalism for arbitrary relation between two Kondo energy scales. While computing the current correction, we performed the full classification of the Feynman diagrams for the many-body perturbation theory on the Keldysh contour. We demonstrated the cancellation of the charge current at the symmetry protected point. The linear response and beyond linear response contributions to the current vanish separately at the symmetry point. Moreover, the independent cancellation of the elastic and inelastic currents at the symmetry protected point was verified. The theoretical method developed in the chapter provides a tool for both quantitative and qualitative description of charge transport in the framework of the two-stage Kondo problem. In particular, the two ratios of FL constants, c_T/c_B and c_V/c_B , quantify the ‘‘amount’’ of interaction between two channels. The interaction is strongest at the symmetry protected point due to strong coupling of the channels.

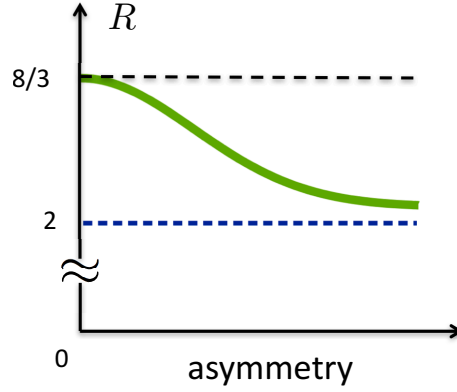


Figure 4.10: Cartoon sketching the evolution of the Wilson ratio as a function of increasing “asymmetry”, meaning that the ratios λ_e/λ_o and λ_{eo}/λ_e both decrease from 1 at the left to 0 at the right. When $\lambda_e=\lambda_o=\lambda_{eo}$, meaning that the even and odd Kondo temperatures coincide, the total spin current is conserved [24] and $R=8/3$ [25]. In the limit of extremely (exponentially) strong channel asymmetry of 2SK model, the (C) regime shown on Fig. 4.1 shrinks to zero. As a result, the 1CK universality class appears and Wilson Ratio is $R=2$ [25]. The behaviour of the Wilson ratio between these two limits is presumably monotonic, since the 2SK model has no other strong coupling fixed points.

The interaction is weakest at single-channel Kondo limit where the odd channel is completely decoupled from the even channel. While we illustrated the general theory of two resonance scattering channels by the two-stage Kondo problem, the formalism discussed in the chapter is applicable for a broad class of models describing quantum transport through nano-structures [153, 154] and behaviour of strongly correlated systems [31].

As an outlook, the approach presented in this chapter can be applied to the calculation of current-current correlation functions (charge noise) of the 2SK problem and, by computing higher cumulants of the current, to studying the full-counting statistics [155, 156]. It is straightforward to extend the presented ideas for generic Anderson-type models away from the particle-hole symmetric point [157–159], and generalize it for the $SU(N)$ Kondo impurity [1] and multi-terminal (multi-stage) as well as multi-dot setup. The general method developed in this chapter is not limited by its application to charge transport through quantum impurity, it can be equally applied to detailed description of the thermo-electric phenomena on the nano-scale [1, 4, 5].

Appendices

4.A Overview of flow from weak to strong coupling

4.A.1 Weak coupling regime

We assume that at sufficiently high temperatures (a precise definition of this condition is given below) the even and odd channels do not talk to each other. As a consequence, we renormalise the coupling between channels and impurity spins ignoring the cross-channel interaction. Performing Anderson’s poor man’s scaling procedure [146] to the even and odd channels independently we obtain the system of two decoupled renormalization group (RG) equations:

$$\frac{dJ_e}{d\Lambda} = 2N_F J_e^2, \quad \frac{dJ_o}{d\Lambda} = 2N_F J_o^2, \quad (4.66)$$

where N_F is the 3D-density of states in the leads. The parameter $\Lambda = \ln\left(\frac{D}{\epsilon}\right)$ depends on the ultraviolet cutoff of the problem (conduction bandwidth D). Note that the RG Eqs. (4.66) are decoupled only in one-loop approximation (equivalent to a summation of so-called parquet diagrams). The solution of these RG equations defines two characteristic energy scales, namely $T_K^e = D \exp(-1/(2N_F J_e))$, which are the Kondo temperatures in the even and odd channels respectively. The second loop corrections to RG couple the equations, generating the cross-term $\propto -J_{eo} \mathbf{s}_e \cdot \mathbf{s}_o$ with $J_{eo} \sim N_F J_e \cdot J_o$. This emergent term flows under RG and becomes one of the leading irrelevant operators of the strong coupling fixed point (the others are $:\mathbf{s}_e \cdot \mathbf{s}_e:$ and $:\mathbf{s}_o \cdot \mathbf{s}_o:$, see Eq.4.8). In addition, the second-loop corrections to RG lead to a renormalization of the pre-exponential factor in the definition of the Kondo temperatures.

Summarizing, we see that the $S=1$, $\mathcal{K}=2$ fully screened Kondo model has a unique strong coupling fixed point, where couplings J_e and J_o diverge in the RG flow. This strong coupling fixed point falls into the FL universality class. The weak coupling regime is therefore defined as $(B, T, eV) \gg (T_K^e, T_K^o)$. Since the interaction between the even channel and local impurity spin corresponds to the maximal eigenvalue of the matrix Eq. (4.5), we will assume below that the condition $T_K^e \geq T_K^o$ holds for any given B, T and eV and, we thus define $T_K^{\min} = T_K^o$. The differential conductance decreases monotonically with increasing temperature in the weak-coupling regime (see Fig. 4.1) being fully described by the perturbation theory [29] in $[1/\ln(T/T_K^e), 1/\ln(T/T_K^o)] \ll 1$.

4.A.2 Intermediate coupling regime

Next we consider the intermediate coupling regime $T_K^o \leq (B, T, eV) \leq T_K^e$ depicted as the characteristic hump in Fig. 4.1. Since the solution of one-loop RG Eqs. (4.66) is given with logarithmic accuracy, we assume without loss of generality that T_K^e and T_K^o are of the same order of magnitude unless a very strong (exponential) channel asymmetry is considered. Therefore, the “hump regime” is typically very small and the hump does not have enough room to be formed. The intermediate regime is characterized by an incomplete screening (see Fig. 4.1) when one conduction channels

(even) falls into a strong coupling regime while the other channel (odd) still remains at the weak coupling. Then the strong-coupling Hamiltonian for the even channel is derived along the lines of Affleck-Ludwig paper Ref. [24] and is given by:

$$H_{\text{even}} = H_0^e + \frac{3}{2} \lambda_e \rho_{e\uparrow} \rho_{e\downarrow} - \frac{3}{4v_F} \lambda_e \sum_{kk'\sigma} (\varepsilon_k + \varepsilon'_k) b_{ek\sigma}^\dagger b_{ek'\sigma}, \quad (4.67)$$

where the b -operators describe Fermi-liquid excitations, $\rho_{e\sigma}(x=0) = \sum_{kk'} b_{ek\sigma}^\dagger b_{ek'\sigma}$ and $\lambda_e \propto 1/T_K^e$ is the leading irrelevant coupling constant [24].

The weak-coupling part of the remaining Hamiltonian is described by a $s_{\text{imp}}=1/2$ Kondo-impurity Hamiltonian $H_{\text{odd}} = J_o \mathbf{s}_o \cdot \mathbf{s}_{\text{imp}}$. Here we have already taken into account that the impurity spin is partially screened by the even channel during the first stage process of the Kondo effect. We remind that the coupling between the even and odd channels is facilitated by a *ferromagnetic* interaction which emerges, being however irrelevant in the intermediate coupling regime. Thus, the differential conductance does reach a maximum $G/G_0 \approx 1$ with a characteristic hump [49], [89] at the intermediate coupling regime. Corresponding corrections (deviation of the conductance at the top of the hump from the unitary limit $G_0 = 2e^2/h$) can be calculated with logarithmic accuracy $|\delta G/G_0| \propto 1/\ln^2(T_K^e/T_K^o)$ [22], [146] (see also review [29] and [89] for details).

4.B Counterterms

We proceed with the calculation of the corrections to the current by eliminating the dependence on the cutoff parameter D by adding the counter terms in the Hamiltonian [24, 106]

$$H_c = -\frac{1}{2\pi\nu} \sum_a \sum_{kk'\sigma} (\delta\alpha_a + \delta\Phi) (\varepsilon_k + \varepsilon_{k'}) : b_{ak\sigma}^\dagger b_{ak'\sigma} :, \quad (4.68)$$

so that we consider only the contribution which remain finite for $D \rightarrow \infty$. The Eq. (4.68) corresponds to the renormalization of leading irrelevant coupling constant α_a such that $\alpha_a \rightarrow \alpha_a + \delta\alpha_a + \delta\Phi$ with

$$\delta\alpha_a = -\alpha_a \phi_a \frac{6D}{\pi} \log\left(\frac{4}{3}\right). \quad (4.69)$$

$$\delta\Phi = -\Phi^2 \frac{9D}{\pi} \log\left(\frac{4}{3}\right). \quad (4.70)$$

During the calculation of the interaction correction we neglected those terms which produce the contribution proportional to the cutoff D [for example, $\propto \int \frac{d\varepsilon}{2\pi} (\Sigma^{++}(\varepsilon) - \Sigma^{--}(\varepsilon)) i\pi\nu \Delta f(\varepsilon)$]. This renormalization of leading irrelevant coupling constant Eq. (4.68) exactly cancel these terms.

4.C Elastic current

To get the elastic current Eq. (4.23), we start from the Landauer-Büttiker formula Eq. (4.19)

$$I_{\text{el}} = \frac{2e}{h} \int_{-\infty}^{\infty} d\varepsilon T(\varepsilon) \Delta f(\varepsilon), \quad (4.71)$$

where the energy dependent transmission coefficient, $T(\varepsilon) = \frac{1}{2} \sum_{\sigma} \sin^2(\delta_{\sigma}^e(\varepsilon) - \delta_{\sigma}^o(\varepsilon))$ and $\Delta f(\varepsilon) = f_L(\varepsilon) - f_R(\varepsilon)$. Taylor expanding the phase shifts to the first order in energy and retaining only upto second order in energy terms in the $T(\varepsilon)$, we arrive at the expression

$$I_{\text{el}} = \frac{2e}{h} (\alpha_e - \alpha_o)^2 \int_{-\infty}^{\infty} d\varepsilon \varepsilon^2 \Delta f(\varepsilon). \quad (4.72)$$

To compute the integral Eq. (4.72) we use the property of the Fourier transform. For the given function $\Delta f(\varepsilon)$, the Fourier transform is defined as

$$\Delta f(t) = \frac{1}{2\pi} \int_{-\infty}^{\infty} e^{-i\varepsilon t} \Delta f(\varepsilon) d\varepsilon. \quad (4.73)$$

Taking n -th derivative of Eq. (4.73) at $t = 0$ we get

$$\int_{-\infty}^{\infty} \varepsilon^n \Delta f(\varepsilon) d\varepsilon = \frac{2\pi}{(-i)^n} \partial_t^n [\Delta f(t)]|_{t=0}. \quad (4.74)$$

Substituting Eq. (4.74) for $n = 2$ into Eq. (4.72), the elastic current cast into the form

$$I_{\text{el}} = \frac{2e}{h} (\alpha_e - \alpha_o)^2 (-2\pi) \partial_t^2 [\Delta f(t)]|_{t=0}. \quad (4.75)$$

The Fourier transform of $\Delta f(\varepsilon)$ for $\mu_{L/R} = \pm eV/2$ is defined by

$$\Delta f(t) = T \frac{\sin(\frac{eVt}{2})}{\sinh(\pi Tt)}. \quad (4.76)$$

Using Eq. (4.76) into Eq.(4.75), we can easily arrive at the expression Eq. (4.23) for the elastic current at finite temperature T , finite bias voltage V and finite in-plane (Zeeman) magnetic field B (assuming $(T, eV, B) \ll T_K^o$)

$$\frac{I_{\text{el}}}{2e^2V/h} = \left[B^2 + \frac{(eV)^2}{12} + \frac{(\pi T)^2}{3} \right] (\alpha_e - \alpha_o)^2. \quad (4.77)$$

4.D Net electric current

Here we present the detail of the computation of total electric current (sum of elastic and inelastic parts) given by Eq. (4.60). We discuss the total current in linear-response (LR) and beyond linear-response (BLR) regime separately. The elastic part is given by Eq. (4.23) and the inelastic part which is composed of the four types of diagrams is expressed by Eq. (4.59).

4.D.1 Linear Response (LR)

As discussed in the main text, both elastic and inelastic processes contribute to the LR current. The LR contribution of the elastic part is expressed by Eq. (4.23). The diagrams of type-1 and type-2 has the finite linear response contribution to the inelastic current. As detailed in Fig. 11,

we have the expression of total linear response current

$$\begin{aligned}
 \frac{\delta I^{\text{LR}}}{2e^2V/h} \frac{1}{(\pi T)^2} &= \underbrace{\left[\frac{1}{3} (\alpha_e - \alpha_o)^2 \right]}_{\text{LR elastic part}} + \\
 &\underbrace{\left[A_T^{(1)}(\phi_e^2 + \phi_o^2) + 3A_T^{(1)}\Phi^2 + \frac{3A_T^{(2)}}{2}(\phi_e + \phi_o)\Phi - \frac{3A_T^{(2)}}{4}\Phi^2 \right]}_{\text{LR inelastic part (type-1 and type-2 diagrams)}} \\
 &= \left[\frac{1}{3} (\alpha_e - \alpha_o)^2 + \frac{2}{3}(\phi_e^2 + \phi_o^2) - 2(\phi_e + \phi_o)\Phi + 3\Phi^2 \right] \\
 &= \left[(\alpha_e - \alpha_o)^2 + 3\left(\Phi - \frac{2}{3}\alpha_e\right)\left(\Phi - \frac{2}{3}\alpha_o\right) \right]. \tag{4.78}
 \end{aligned}$$

At the symmetry point the linear response contribution to the current given by the Eq. (4.78) exactly vanishes.

4.D.2 Beyond Linear Response (BLR)

The BLR contribution of the elastic part is expressed by Eq. (4.23). The diagrams of type-3 and type-4 produce the finite contribution to the inelastic current only beyond the LR regime. In addition to the LR contribution, the type-1 and type-2 diagrams also contribute to non-linear response. As detailed in Fig. 12, the total non-linear current is

$$\begin{aligned}
 \frac{\delta I^{\text{BLR}}}{2e^2V/h} \frac{1}{(eV)^2} &= \underbrace{\left[\frac{1}{12} (\alpha_e - \alpha_o)^2 \right]}_{\text{BLR elastic part}} \\
 &+ \underbrace{\left[A_V^{(1)}(\phi_e^2 + \phi_o^2) + 3A_V^{(1)}\Phi^2 + \frac{3A_V^{(2)}}{2}(\phi_e + \phi_o)\Phi - \frac{3A_V^{(2)}}{4}\Phi^2 \right]}_{\text{BLR inelastic part (type-1 and type-2 diagrams)}} \\
 &+ \underbrace{\left[A_V^{(4)}\phi_e\phi_o + 3A_V^{(3)}(\phi_e + \phi_o)\Phi + \frac{3}{2}(A_V^{(4)} - A_V^{(3)})\Phi^2 \right]}_{\text{BLR inelastic part (type-3 and type-4 diagrams)}} \\
 &= \left[\frac{1}{12} (\alpha_e - \alpha_o)^2 + \frac{5}{12}(\phi_e^2 + \phi_o^2) - \frac{5}{4}(\phi_e + \phi_o)\Phi \right. \\
 &\quad \left. + \frac{15}{8}\Phi^2 + \frac{1}{2}\phi_e\phi_o - \frac{3}{4}(\phi_e + \phi_o)\Phi + \frac{9}{8}\Phi^2 \right] \\
 &= \left[\frac{1}{2}(\alpha_e - \alpha_o)^2 + 3\left(\Phi - \frac{2}{3}\alpha_e\right)\left(\Phi - \frac{2}{3}\alpha_o\right) \right]. \tag{4.79}
 \end{aligned}$$

The BLR contribution to the current expressed by Eq. (4.79) goes to zero at the symmetry point $\alpha_e = \alpha_o = 3\Phi/2$.

The sum of the LR and BLR contributions results in Eq. (4.60). For completeness

$$\begin{aligned}
 \frac{\delta I}{2e^2V/h} &= 3 \left[(\pi T)^2 + (eV)^2 \right] \left(\Phi - \frac{2}{3}\alpha_e \right) \left(\Phi - \frac{2}{3}\alpha_o \right) \\
 &\quad + \left[(\pi T)^2 + \frac{1}{2}(eV)^2 \right] (\alpha_e - \alpha_o)^2. \tag{4.80}
 \end{aligned}$$

$$\begin{aligned}
 \delta I_{\text{in}}^{\phi^2} &= \left[\text{type-1} \right] + \delta I_{\text{in}}^{\phi_o^2} \\
 &= \frac{2e^2V}{h} \left[A_V^{(1)}(eV)^2 + A_T^{(1)}(\pi T)^2 \right] (\phi_e^2 + \phi_o^2) \\
 \delta I_{\text{in}}^{\Phi^2} &= +\frac{1}{4} \left[\text{type-1} \right] \\
 &\quad + \frac{1}{4} \left[\text{type-1} \right] \\
 &\quad + \frac{1}{4} \left[\text{type-2} \right] \\
 &= \frac{6e^2V}{h} \left[\left(A_V^{(1)} - \frac{A_V^{(2)}}{4} \right) (eV)^2 + \left(A_T^{(1)} - \frac{A_T^{(2)}}{4} \right) (\pi T)^2 \right] \Phi^2 \\
 \delta I_{\text{in}}^{\phi_a\Phi} &= -\frac{1}{2} \left[\text{type-2} \right] + \delta I_{\text{in}}^{\phi_o\Phi} \\
 &= \frac{3e^2V}{h} \left[A_V^{(2)}(eV)^2 + A_T^{(2)}(\pi T)^2 \right] (\phi_e + \phi_o) \Phi
 \end{aligned}$$

Figure 11: (Color online) Feynman diagrams of type-1 and type-2 contributing to the charge current both in the linear response and beyond the linear response regime. The coefficients computed in the Sec 4.4.2 and Sec 4.4.2 take the following values: $A_T^{(1)}=2/3$, $A_T^{(2)}=-4/3$, $A_V^{(1)}=5/12$, $A_V^{(2)}=-5/6$.

$$\begin{aligned}
 \delta I_{\text{in}}^{\Phi^2} &= \frac{1}{4} \left[\underbrace{\text{type-4}}_{\text{type-4}} + \underbrace{\text{type-3}}_{\text{type-3}} + \underbrace{\text{type-3}}_{\text{type-3}} \right] \\
 &= \frac{3e^2V}{h} \left[(A_V^{(4)} - A_V^{(3)})(eV)^2 + (A_T^{(4)} - A_T^{(3)})(\pi T)^2 \right] \Phi^2 \\
 \delta I_{\text{in}}^{\phi_e \Phi} &= -\frac{1}{2} \left[\underbrace{\text{type-3}}_{\text{type-3}} \right] \\
 &\quad \left[\underbrace{\text{type-3}}_{\text{type-3}} \right] + \delta I_{\text{in}}^{\phi_o \Phi} \\
 &= \frac{6e^2V}{h} \left[A_V^{(3)}(eV)^2 + A_T^{(3)}(\pi T)^2 \right] (\phi_e + \phi_o) \Phi \\
 \delta I_{\text{in}}^{\phi_e \phi_o} &= \left[\underbrace{\text{type-4}}_{\text{type-4}} \right] = \frac{2e^2V}{h} \left[A_V^{(4)}(eV)^2 + A_T^{(4)}(\pi T)^2 \right] \phi_e \phi_o
 \end{aligned}$$

Figure 12: (Color online) Feynman diagrams of type-3 and type-4 contributing to the charge current beyond the linear response. The coefficients computed in the Sec 4.4.2 and Sec 4.4.2 take the following values: $A_T^{(3)} = A_T^{(4)} = 0$, $A_V^{(3)} = -1/4$, $A_V^{(4)} = 1/2$.

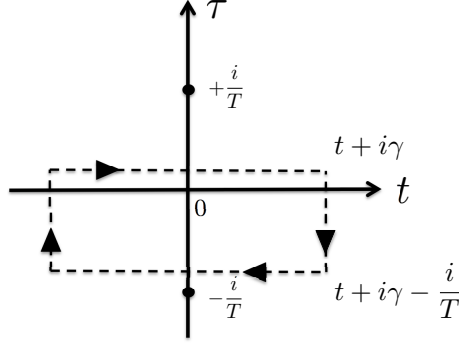


Figure 13: The contour of the integration for the integral Eq. (4.81) with negative shift.

This equation represents in a simple and transparent form contribution of the three FL constants to the charge transport.

4.E Calculation of integrals

In this section we calculate two integrals that we used for the calculation of current correction contributed by four types of diagram. The first integral to calculate is

$$\mathcal{I}_1 = \int_{-\infty}^{\infty} \frac{\cos^3(\frac{eV}{2}t) \sin(\frac{eV}{2}t)}{\sinh^4(\pi Tt)} dt. \quad (4.81)$$

The singularity of the integral in Eq. (4.81) is removed by shifting the time contour by $i\gamma$ in the complex plane as shown in Fig. 13. The point splitting parameter γ is chosen to satisfy the conditions $\gamma D \gg 1$ and $\gamma T \ll 1$, $\gamma eV \ll 1$, where, D is the band cutoff. Then the Eq.(4.81) can be written as

$$\begin{aligned} \mathcal{I}_1^+ &= \int_{-\infty+i\gamma}^{\infty+i\gamma} \frac{\cos^3(at) \sin(at)}{\sinh^4(\pi Tt)} dt \\ &= -\frac{i}{16} [\mathcal{Z}(4a, T) - \mathcal{Z}(-4a, T) + 2\mathcal{Z}(2a, T) - 2\mathcal{Z}(-2a, T)]. \end{aligned} \quad (4.82)$$

In Eq. (4.82), $a=eV/2$ and we introduced the short hand notation,

$$\mathcal{Z}(a, T) = \int_{-\infty+i\gamma}^{\infty+i\gamma} \frac{e^{iat}}{\sinh^4(\pi Tt)} dt = \int_{-\infty+i\gamma}^{\infty+i\gamma} h(a, T; t) dt. \quad (4.83)$$

The poles of the integrand $h(a, T; t)$ in Eq. (4.83) are

$$\pi Tt = \pm im\pi \Rightarrow t = \pm \frac{im}{T}, \quad m = 0, \pm 1, \pm 2, \pm 3... \quad (4.84)$$

The integration of $h(a, T; t)$ over the rectangular contour Fig. 13 shifted by i/T upon using the Cauchy residue theorem results

$$\begin{aligned} \mathcal{Z}(a, T) &= \int_{-\infty+i\gamma}^{\infty+i\gamma} \frac{e^{ia(t-\frac{i}{T})}}{\sinh^4(\pi T(t-\frac{i}{T}))} dt \\ &\quad - 2\pi i \times \text{Res}[h(a, T; t)]|_{t=0}, \end{aligned} \quad (4.85)$$

where ‘‘Res’’ stands for the residue. By expanding the sinh function in Eq. (4.85) we get

$$\mathcal{Z}(a, T) \left(1 - e^{\frac{a}{T}}\right) = -2\pi i \times \text{Res}[h(a, T; t)]|_{t=0}. \quad (4.86)$$

By using the standard formula for the calculation of the residue, we express the Eq. (4.86) into the form

$$\mathcal{Z}(a, T) = -\frac{2\pi (a^3 + 4a(\pi T)^2)}{6(\pi T)^4} \times \frac{1}{1 - e^{\frac{a}{T}}}. \quad (4.87)$$

Use of Eq. (4.87) into Eq. (4.82) gives the required integral

$$\mathcal{I}_1^+ = \frac{i\pi}{(\pi T)^4} \frac{eV}{2} \left[\frac{5}{12}(eV)^2 + \frac{2}{3}(\pi T)^2 \right]. \quad (4.88)$$

Choosing the contour with the negative shift results in the integral \mathcal{I}_1^- such that $\mathcal{I}_1^- = -\mathcal{I}_1^+$. As a result

$$\mathcal{I}_1^\pm(V, T) = \pm \frac{i\pi}{(\pi T)^4} \frac{eV}{2} \left[\frac{5}{12}(eV)^2 + \frac{2}{3}(\pi T)^2 \right]. \quad (4.89)$$

The second integral that we are going to compute is

$$\mathcal{I}_2 = \int_{-\infty}^{\infty} \frac{\cos(\frac{eV}{2}t) \sin^3(\frac{eV}{2}t)}{\sinh^4(\pi T t)} dt. \quad (4.90)$$

In the same way and using the same notations as for the first integral, Eq. (4.90) reads

$$\begin{aligned} \mathcal{I}_2^+ &= \frac{i}{16} [\mathcal{Z}(4a, T) - \mathcal{Z}(-4a, T) - 2\mathcal{Z}(2a, T) + 2\mathcal{Z}(-2a, T)] \\ &= -\frac{i\pi}{(\pi T)^4} \left(\frac{eV}{2}\right)^3. \end{aligned} \quad (4.91)$$

Similar to Eq. (4.89), the integral \mathcal{I}_2 takes the form

$$\mathcal{I}_2^\pm(V, T) = \mp \frac{i\pi}{(\pi T)^4} \left(\frac{eV}{2}\right)^3. \quad (4.92)$$

For the calculations of all diagrams we used the corresponding results of contour integration with positive shift.

Chapter 5

Full counting statistics of the two-stage Kondo effect

In this chapter we develop a method of full counting statistics applicable to the multi-stage Kondo paradigm. The content of this chapter has been previously published as:

D. B. Karki and Mikhail N. Kiselev,
Full counting statistics of the two-stage kondo effect,
[Phys. Rev. B **98**, 165443 \(2018\)](#).

5.1 Background

Quantized charge in nanoscale systems results in large current fluctuations [160]. Besides, thermal fluctuations are ubiquitous at finite temperature. These fluctuations are prevalently measured by charge current and its noise, the first and second cumulant of fluctuating current [59]. The study of noise in a generic nanodevice provides underlying transport informations that cannot be inferred from the average current measurements [59, 155, 156, 160–164]. In particular, noise measurement imparts an effective way of probing the dynamics of charge transfer [59, 164]. Moreover, noise has revealed the nature of quasi-particle interactions and different types of entanglements associated with the system [165–167]. In addition to first and second cumulant of the fluctuating current, the fundamental relevance of higher order cumulants to describe the transport processes in nanostructure has been also demonstrated [165, 168–175].

The method of full counting statistics (FCS) furnishes an elegant way to scrutinize an *arbitrary* (n -th) order cumulant of current through a nanodevice [155, 161, 162]. The probabilistic interpretation of charge transport is at the core of FCS theory. The primary object of FCS is the moment generating function (MGF) for the probability distribution function (PDF) of transferred charges within a given time interval [155, 161, 162]. The moments of PDF of order $n \geq 2$ charac-

terize the current fluctuations. The FCS scheme permits in this way a transparent study of the quantum transport in various nanostructures. Notably, FCS of the normal metal-superconductor hybrid structures, superconducting weak links, tunnel junctions, chaotic cavities, entangled electrons, spin-correlated systems, charge shuttles, nanoelectromechanical systems are most striking examples [176–183].

In nanoscale transport studies, an archetype of electronic device consists of an impurity sandwiched between two reservoirs of conduction electrons [59, 160]. The artificial atom, molecule, quantum dot (QD), carbon nano tube (CNT) etc., plays the role of an impurity. Given their low tunneling rate, the QDs represents archetypal setups for the study of a highly accurate FCS [184], the main concern of present work. The transport through the QD depends strongly on the associated number of electronic levels, while the orbitals of the impurity play the major role to define the underlying transport characteristics [10]. Out of all the impurities-mediated transport processes, those with intrinsic magnetic moment; hence magnetic in nature, have attracted an ever increasing interests [10, 31]. One can expect variant transport fingerprints when such magnetic impurities exchange coupled to conduction electrons (for review see Ref. [26]).

In the low energy regime of transport measurements, the correlation between the localized spin of impurity and the spin of conduction electrons results in the well known many-body phenomenon, the Kondo screening effect [7]. The fundamental role of Kondo effect in enhancing and controlling the transport through a nanostructure is the acknowledged evidence [8, 20, 22, 24, 27, 28, 33–35, 73, 185, 186]. In a transport setup with two reservoirs (leads), the Kondo screening of the localized spin is caused by at most two conduction channels, the symmetric and anti-symmetric combination of electron states in the leads. The interplay between the number of conduction channels ($\mathcal{K}=1, 2$) and the effective spin of magnetic impurity ($\mathcal{S}\geq 1/2$) boosts up further the richness of Kondo physics. In the particular case of $\mathcal{K}=2\mathcal{S}$, the effective spin of impurity gets completely screened by the spin of conduction electrons. Such fully-screened Kondo effects are of immense interest given their low energy behavior described by a local Fermi-Liquid (FL) theory [20, 22, 24].

The Kondo screening involving only a single channel of conduction electrons ($\mathcal{K}=1$) and a spin half impurity ($\mathcal{S}=1/2$) forms the prototypical example of fully-screened Kondo effect. The magnetic impurities with only one orbital manifest the single channel Kondo (1CK) effect. Tremendous perseverance efforts [29, 106, 147, 151] has been devoted in understanding the transport behavior in paradigmatic 1CK schemes. Moreover, various seminal works [93–97, 187] paved the way to access the associated FCS in 1CK realm. Unlike the 1CK, the transport characteristics of a multi-orbital impurity has been less explored. In this facet, many orbitals of the conduction channels are involved in screening the impurity spin (multi-channel screening), which make the problem more obscure [49]. Several theoretical and experimental evidences [47–49, 188, 189] have been put fourth showing the relevance of multi-channel screening effect in a generic transport setup. The simplest multi-channel screening involves two conduction channels ($\mathcal{K}=2$) and $\mathcal{S}\geq 1/2$; general manifestation of a two leads geometry. In the present work we focus only on the particular case of multi-channel screening such that $\mathcal{K}=2\mathcal{S}$ in a two leads setup. Thus the $\mathcal{S}=1$ impurity interacting with two channels of conduction electrons forms the minimal description of multi-channel screening in FL

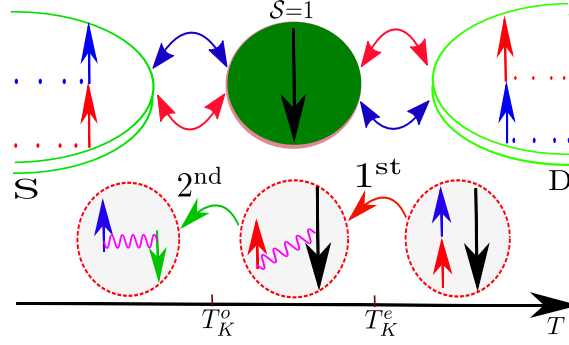


Figure 5.1: Upper panel: Schematic representation of a generic 2SK effect setup. The effective spin $\mathcal{S}=1$ impurity is tunnel-coupled with two external leads, the source S and the drain D. Lower panel: Flow diagram of 2SK model from weak to strong coupling. For the entries in the figure and their explanations see Sec. 5.2.

regime [2, 45].

Multi-orbital quantum impurity with effective spin $\mathcal{S}=1$ connected to two terminals can lead to a Kondo effect exhibiting two-stage screening [2]. The first-stage screening process constitutes an under-screened Kondo effect where the impurity spin is effectively reduced from $\mathcal{S}=1$ to $\mathcal{S}=1/2$. Subsequently, second-stage screening leads to complete screening of the impurity spin and the formation of a Kondo singlet. This feature of screening is called two-stage Kondo (2SK) effect [45, 49]. The low energy description of such 2SK effects is still governed by a local FL theory. Nonetheless, transport properties of such FL get modified in dramatic ways compared to 1CK [2]. The strong interplay between two conduction channels, both close to resonance scattering, causes aforesaid different transport features over 1CK. The lack of compatible cure of the two Kondo resonances makes the 2SK paradigm far from being trivial [45, 49, 89]. To analyze the equilibrium and non-equilibrium transport properties of a generic 2SK effect, a two-color local FL theory has been recently developed [2]. Here, the absence of zero-bias anomaly and non-monotonicity of FL transport coefficients are demonstrated as the hallmarks of 2SK effect.

These two traits of the 2SK effect, which are contrasting over 1CK, have raised many fascinating concerns. For instance, how these fingerprints can affect the higher cumulants of charge current, particularly the noise to signal ratio. This ratio is commonly known as the Fano factor (F). The zero temperature limit of F is of extreme experimental interest [106, 190]. In theoretical perspective, the method of FCS pertaining to the two resonance channels of conduction electrons has not been developed yet. In this chapter we aim to reveal the FCS for 2SK effect based on the local Fermi-liquid theory in combination with the non-equilibrium Keldysh framework.

5.2 Setup and model Hamiltonian

The cartoon representing the generic 2SK effect is as shown in upper panel of Fig. 5.1. The generic quantum impurity sandwiched between two conducting leads (the source S and the drain D) is described by the Anderson model with the Hamiltonian

$$H_A = \sum_{k\alpha\sigma} \xi_k c_{\alpha k\sigma}^\dagger c_{\alpha k\sigma} + \sum_{\alpha k i\sigma} t_{\alpha i} c_{\alpha k\sigma}^\dagger d_{i\sigma} + \text{H.c.} + \sum_{i\sigma} \varepsilon_i d_{i\sigma}^\dagger d_{i\sigma} + E_c \hat{N}^2 - \mathcal{J} \hat{S}^2. \quad (5.1)$$

The conducting leads are described by the first term of Eq. (5.1) such that the operator $c_{\alpha k\sigma}^\dagger$ creates an electron with momentum k and spin $\sigma = \uparrow (+), \downarrow (-)$ in the α ($\alpha = \text{S, D}$) lead. Here ξ_k is the energy of conduction electrons with respect to the chemical potential μ . The operator $d_{i\sigma}$ describes electrons with energy ε_i and spin σ in the i -th orbital state of the quantum impurity. The tunneling matrix elements are represented by $t_{\alpha i}$, the charging energy of the impurity (dot) is E_c and $\mathcal{J} \ll E_c$ is an exchange integral accounting for the Hund's rule [89]. The total number of electrons in the dot is given by an operator $\hat{N} = \sum_{i\sigma} d_{i\sigma}^\dagger d_{i\sigma}$. The two electrons in the dot ensures the expectation value of \hat{N} to be $\bar{n}_d = 2$ and the total spin $S = 1$. Application of the Schrieffer-Wolff transformation [112] to the Hamiltonian Eq. (5.1) results in the effective Kondo Hamiltonian for the spin-1 quantum impurity [29, 89].

To proceed with the calculation of FCS relevant to the setup in Fig. 5.1, we assume that the thermal equilibrium is maintained in source and drain, separately, at temperature T . The chemical potentials of source and drain electrodes are μ_S and μ_D respectively. The applied voltage bias across source and drain drives the impurity-leads system out-of-equilibrium. For the sake of simplicity, we consider symmetrically applied bias voltage such that $\mu_S - \mu_D = eV$, where e is the electronic charge. In this frame, the symmetrical (even, e) and anti-symmetrical (odd, o) combinations of electron operators in the two leads interact with the impurity. Assuming $c_{S/D}$ as an operator that annihilates an electron in the source/drain, the even/odd combinations of electron operators are $b_{e/o} = (c_S \pm c_D) / \sqrt{2}$. These states are also known as conduction channels. In Fig. 5.1, we used arrows with different color to show that the electrons form even and odd channels (\uparrow , electron forms channel- e and \uparrow , electron forms channel- o). Likewise, the interaction between even (odd) channel and impurity is represented by two-headed arrow with blue (red) color. In our convention, blue (red) color is generic for even (odd) channel.

In conventional 1CK effect the odd channel is completely decoupled from the impurity [20]. The interacting channel (even channel) is characterized by the Kondo temperature T_K^e . Depending upon the applied bias eV and the temperature T in particular setup, different coupling regimes come into play. Namely, $(eV, T) \leq T_K^e$, the strong-coupling regime and $(eV, T) \geq T_K^e$, the weak-coupling regime. Immense efforts, experimental inclusive of theory, have been paid for the transport description of 1CK effect in both of the above regimes (see Refs. [10, 29] for review).

In two-leads setup with a generic quantum impurity having more than one orbital, neither of the electron combinations remain decoupled from the impurity [45, 49]. Consequently, both of the conduction channels take part for the screening of localized spin of the impurity. In addition to T_K^e another energy scale characterizing the Kondo temperature of the odd channel, T_K^o become impor-

tant for the problem of 2SK effect. The interplay between two Kondo temperatures ($T_K^a, a=e, o$) makes the 2SK problem very reach then 1CK, but, at the same time quite difficult. Perturbation treatments of weak, $(eV, T) > \max(T_K^e, T_K^o)$ and intermediate, $T_K^o \leq (eV, T) \leq T_K^e$, coupling regimes have been formulated [45, 89]. In the intermediate regime the impurity spin get partially screened via first (1st)-stage of screening. Further decreasing the temperature and bias voltage down, to satisfy the condition $(eV, T) \ll \min(T_K^e, T_K^o)$, results in strong-coupling regime of 2SK effect. In this second (2nd)-stage the complete screening of impurity spin is achieved. These three coupling regimes are shown in lower panel of Fig. 5.1.

Furthermore, it has been argued [45, 49] that the most nontrivial part of 2SK effect is the strong-coupling regime, where both of the interacting channels are close to the resonance scattering. Since, the 2SK effect satisfies the identity $\mathcal{K}=2\mathcal{S}$, it offers the transport description in terms of a local FL. From now on, we focus only on the strong-coupling regime of 2SK effect. Owing to its low energy behavior as a local FL, we describes the strong-coupling regime of 2SK effect in the spirit of Nozieres FL theory [20, 24]. Accordingly, the Kondo singlet (Kondo cloud) acts as the scatterer for the incoming electrons from the leads. Outgoing and incoming electrons then differ from each other by the phase shifts $\delta_\sigma^a(\varepsilon)$. At low energy, $\varepsilon \ll \min(T_K^e, T_K^o)$, we expand the phase shifts in terms of phenomenological parameters to write [20]

$$\delta_\sigma^a(\varepsilon) = \delta_0^a + \alpha_a \varepsilon - \phi_a \delta N_\sigma^a + \Phi \sigma (\delta N_\uparrow^{\bar{a}} - \delta N_\downarrow^{\bar{a}}). \quad (5.2)$$

Here, $\delta_0^a = \pi/2$ are the resonance phase shifts considered to be the same for both channels and both spin components. Writing Eq. (5.2) we explicitly consider the particle-hole (PH) symmetric limit; $\sigma = \uparrow, \downarrow$ ($\bar{\sigma} = \downarrow, \uparrow$). First two terms of Eq. (5.2) represents the purely elastic effects associated with two channels. These are, equivalently, known as the scattering terms. The parameters α_a are the Nozieres FL coefficients characterizing the scattering. Although, for $\varepsilon=T=eV=0$ both channels are at resonance, the way phase shifts changes with energy is different in two channels. This consequence can be accounted for by defining the Kondo temperatures as [1, 147]

$$T_K^a = 1/\alpha_a. \quad (5.3)$$

For definiteness, we consider $T_K^o \leq T_K^e$ throughout the chapter.

The third and fourth terms of Eq. (5.2) are due to the finite inelastic effects. These are known as interaction terms. The parameters ϕ_a quantify the intra-channel interactions, and the inter-channel interaction is accounted for by Φ . The notation δN_σ^a is defined by,

$$\delta N_\sigma^a = \int_{-\infty}^{\infty} \left[\langle b_{a\varepsilon\sigma}^\dagger b_{a\varepsilon\sigma} \rangle_0 - \Theta(\varepsilon_F - \varepsilon) \right] d\varepsilon.$$

Here, ε_F , in the argument of step function Θ , is the Fermi energy. The average $\langle \dots \rangle_0$ is taken with respect to non-interacting Hamiltonian describing the free electrons in two channels,

$$H_0 = \nu \sum_{a\sigma} \int_{\varepsilon} \varepsilon b_{a\varepsilon\sigma}^\dagger b_{a\varepsilon\sigma}, \quad (5.4)$$

where, ν is the density of states per species for a one-dimensional channel. We see that the phase shifts expression, Eq. (5.2), consist of five FL parameters ($\alpha_e, \alpha_o, \phi_e, \phi_o$ and Φ). However, the

invariance of phase shifts under the shift of reference energy (the floating of the Kondo resonance [106]) recovers the FL identity $\alpha_a = \phi_a$. Thereupon, three independent FL parameters (α_e , α_o and Φ) completely describes the low energy sector of 2SK problem. With the specification of T_K^a in terms of α_a as in Eq. (5.3), we have only one FL parameter (Φ) to relate with the physical observables. The response functions measurements could provide the way to access the parameter Φ [2]. Therefore, all the phenomenological parameters in Eq. (5.2) are under control in an experiment.

The finding of seminal work [24] paved the way to formulate the Hamiltonian describing the scattering and interaction processes in Eq. (5.2). The PH symmetry of the problem demands the scattering terms to be represented by the Hamiltonian,

$$H_{\text{el}} = -\frac{\alpha_a}{2\pi} \sum_{a\sigma} \int_{\varepsilon_{1-2}} (\varepsilon_1 + \varepsilon_2) b_{a\varepsilon_1\sigma}^\dagger b_{a\varepsilon_2\sigma}. \quad (5.5)$$

Similarly, the intra-channel and inter-channel quasi-particles interactions are represented by the Hamiltonians H_ϕ and H_Φ respectively, $H_{\text{in}} = H_\phi + H_\Phi$ represents the total interactions associated with 2SK effect. Here,

$$H_\phi = \frac{\phi_a}{2\pi\nu} \sum_{a\sigma} \int_{\varepsilon_{1-4}} : \rho_{\varepsilon_1\varepsilon_2\sigma}^a \rho_{\varepsilon_3\varepsilon_4\bar{\sigma}}^a :, \quad (5.6)$$

$$H_\Phi = -\frac{\Phi}{2\pi\nu} \sum_{\sigma_{1-4}} \int_{\varepsilon_{1-4}} : S_{\varepsilon_1\varepsilon_2\sigma_1\sigma_2}^o S_{\varepsilon_3\varepsilon_4\sigma_3\sigma_4}^e : \dots \quad (5.7)$$

The colon, $: \dots :$, denotes the normal ordering. In Eqs. (5.6) and (5.7) we used the short-hand notations

$$\rho_{\varepsilon_1\varepsilon_2\sigma}^a \equiv b_{a\varepsilon_1\sigma}^\dagger b_{a\varepsilon_2\sigma}, \quad S_{\varepsilon_1\varepsilon_2\sigma_1\sigma_2}^a \equiv b_{a\varepsilon_1\sigma_1}^\dagger \tau_{\sigma_1\sigma_2} b_{a\varepsilon_2\sigma_2},$$

with $\tau_{\sigma_i\sigma_j}$ the elements of Pauli-matrices. The scattering and interaction parts of Hamiltonian given in Eqs. (5.5)–(5.7) are first-order in $1/T_K^a$. The two-leg vertex α_a and the four-leg vertices ϕ_a and Φ are shown in Fig. 5.2. In general the symmetry of the problem also allows one to construct the Hamiltonian with eight-leg vertex, for instance $\tilde{\mathcal{H}} \propto \tilde{\phi} (\rho_\sigma \rho_{\bar{\sigma}})^a (\rho_\sigma \rho_{\bar{\sigma}})^{\bar{a}}$. Note that in the present work we restrict ourselves to the second order correction to the CGF, thus the relevant terms are upto the $\mathcal{O}(T/T_K^a)^2$. Since the vertex $\tilde{\phi}$ is already second order in $1/T_K^a$, it does not contribute to the cumulants of charge current within second order perturbative calculation, hence has been neglected. Thus the Hamiltonian $H \equiv H_0 + H_{\text{el}} + H_{\text{in}}$ constitutes the minimal model Hamiltonian of a generic 2SK effect. This particular model has the channel symmetry at the point $\alpha_e = \alpha_o$ and $\alpha_a = 3/2\Phi$, where the conductance vanishes due to the destructive interference between two interacting channels [2]. It is worth noting that the effects of breaking PH symmetry can be accounted for by introducing extra first and second generation of FL coefficients into Eq. (5.2) in the spirit of Ref. [106]. The n -th generation of FL coefficients refers to the n -th order coefficients in the Taylor expansion of the scattering phase shifts with respect to the energy. Moreover for the description of FCS beyond PH symmetric point, the density-density inter-channel interaction should be added. The finite potential scattering amounts to renormalizes the resonance phase shifts in such a way that $\delta_0^a \rightarrow \delta_0^a + \delta_P^a$, $\delta_P^a \ll \delta_0^a$ [1].

5.3 Full counting statistics

The randomness of transferred charge (q) through a nanodevice during a measurement time (\mathcal{T}) is specified by the PDF, $\mathcal{P}(q)$. Then, the central object of FCS, the MGF is given by

$$\chi(\lambda) = \sum_q \mathcal{P}(q) e^{i\lambda q}. \quad (5.8)$$

Here, λ is the charge counting field. Following the spirit of pioneering works [93, 94], we conceal the 2SK many-body Hamiltonian into the MGF (see text below). The complete charge transferred statistics of 2SK effect is, then, obtained via cumulant generating function (CGF) $\ln \chi(\lambda)$. The n -th order differentiation of CGF with respect to the counting field, delivers the arbitrary moment (central) of charge current. Besides, the counting field, λ , is explicitly time dependent which takes different value in forward (\mathcal{C}_-) and backward (\mathcal{C}_+) Keldysh contour

$$\lambda(t) = \begin{cases} \lambda, & \text{if } 0 < t < \mathcal{T} \text{ and } t \in \mathcal{C}_- \\ -\lambda, & \text{if } 0 < t < \mathcal{T} \text{ and } t \in \mathcal{C}_+ \\ 0, & \text{else} \end{cases} \quad (5.9)$$

Here the Keldysh contour extends from $-\infty$ to \mathcal{T} and back to ∞ . Note that, in order to calculate the FCS, the current measurement device has to be included in the Hamiltonian description. Such terms in the Hamiltonian due to the measuring device can be eliminated by means of unitary transformation of the form $U \sim e^{-i\lambda(t)\hat{N}_\alpha}$, \hat{N}_α being the number operator of the electrons in α reservoir [94]. This transformation changes only the tunneling part of the Hamiltonian Eq. (5.1). Analogously, in the strong-coupling regime the charge measuring field causes the rotation of the even and odd electron states in the reservoirs such that [93]

$$b_a^\lambda = \cos(\lambda/4) b_a - i \sin(\lambda/4) b_{\bar{a}}. \quad (5.10)$$

Under this transformation the free part of Hamiltonian, H_0 , remains unchanged. Nevertheless, the Hamiltonian corresponding to the sum of scattering and interaction effects, \mathcal{H} ($\equiv H_{\text{el}} + H_{\text{in}}$), transforms to $\mathcal{H}^\lambda = \mathcal{H} + \lambda/4 \hat{I}_{\text{bs}}$. Here, we considered only the lowest order terms in counting field. The backscattering current, \hat{I}_{bs} , is given by the commutator $\hat{I}_{\text{bs}} = i[Q, H]$, where Q is the charge transferred operator across the junction $Q = 1/2 \sum_{k\sigma} (b_{ek\sigma}^\dagger b_{ok\sigma} + \text{H.c.})$. Since there are no zeroth order transmission processes in 2SK [2], the MGF is given by

$$\chi(\lambda) = \left\langle T_C \exp \left[-i \int_C \mathcal{H}^\lambda(t) dt \right] \right\rangle_0. \quad (5.11)$$

Where T_C is time ordering operator in Keldysh contour, C . The expansion of Eq. (5.11) in \mathcal{H}^λ and use of Wick's theorem paved the way to proceed with the perturbative study of MGF, $\chi(\lambda)$. Then the n -th order (arbitrary) moment of charge current is given by

$$\mathcal{C}_n = \frac{1}{\mathcal{T}} (-i)^n \left. \frac{d^n}{d\lambda^n} \ln \chi(\lambda) \right|_{\lambda=0}. \quad (5.12)$$

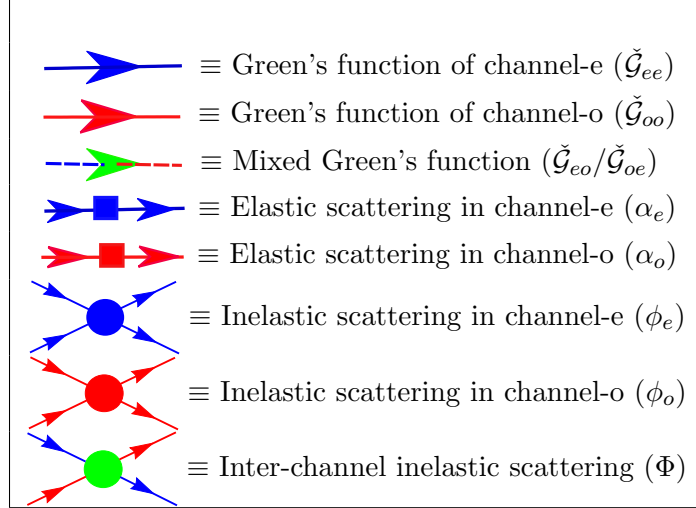


Figure 5.2: Feynman diagrammatic codex used for the calculation of FCS in the presence of two conduction mode.

To proceed with the calculation for the higher cumulants of charge current, we require Keldysh Green's functions (GFs) in λ -rotated basis. As the odd conduction channel remains completely decoupled, the Keldysh GFs of even channel ($\check{\mathcal{G}}_{ee}$) suffice to characterize the transport of 1CK schemes. However, the consistent treatment of 2SK effect requires two additional Keldysh GFs, the Keldysh GFs of odd channel ($\check{\mathcal{G}}_{oo}$) and that of mixed channel ($\check{\mathcal{G}}_{eo/oe}$). Note that, the spin index in these GFs is implicit. Besides, we prefer the renaming of GFs $\check{\mathcal{G}}_{ee}$ and $\check{\mathcal{G}}_{oo}$ as the channel-diagonal GFs, and $\check{\mathcal{G}}_{eo/oe}$ as mixed GFs, whenever necessary. The energy representation of these Keldysh GFs is

$$\check{\mathcal{G}}_{aa/a\bar{a}}(\varepsilon) = \begin{bmatrix} \mathcal{G}_{aa/a\bar{a}}^{--}(\varepsilon) & \mathcal{G}_{aa/a\bar{a}}^{-+}(\varepsilon) \\ \mathcal{G}_{aa/a\bar{a}}^{+-}(\varepsilon) & \mathcal{G}_{aa/a\bar{a}}^{++}(\varepsilon) \end{bmatrix}, \quad (5.13)$$

with the diagonal GFs,

$$\mathcal{G}_{aa/a\bar{a}}^{--}(\varepsilon) = \mathcal{G}_{aa/a\bar{a}}^{++}(\varepsilon) = i\pi\nu [(f_S - 1/2) \pm (f_D - 1/2)], \quad (5.14)$$

are independent of counting field λ . Here, $f_{S/D} \equiv f_{S/D}(\varepsilon)$ is the free-electron Fermi distribution function of source/drain reservoir. The off-diagonal GFs explicitly depend on λ , are given by

$$\mathcal{G}_{aa/a\bar{a}}^{+-}(\varepsilon) = e^{i\lambda/2} (f_S - 1) \pm e^{-i\lambda/2} (f_D - 1). \quad (5.15)$$

$$\mathcal{G}_{aa/a\bar{a}}^{-+}(\varepsilon) = e^{-i\lambda/2} f_S \pm e^{i\lambda/2} f_D. \quad (5.16)$$

The pictorial representation of these GFs is as shown in Fig. 5.2. Neither of the above GFs includes the principal parts, since they do not contribute to the local quantities in the flat band model [93]. The Fourier transformation (FT) of Eq. (5.16) into the real time permits,

$$\mathcal{G}_{aa/a\bar{a}}^{-+}(t) = \mp\pi\nu T \frac{e^{i(\frac{\lambda}{2} + \frac{eV}{2}t)} \pm e^{-i(\frac{\lambda}{2} + \frac{eV}{2}t)}}{2 \sinh(\pi T t)}. \quad (5.17)$$

The singularity in Eq. (5.17) is removed by shifting the contour of integration upward from the origin such that $t \rightarrow t + i\eta$ for $\eta \rightarrow 0$. The GFs $\mathcal{G}^{+-}(t)$ has the analogous expression as $\mathcal{G}^{-+}(t)$ [95].

We substitute the scattering (elastic) part of the Hamiltonian, H_{el} , into Eq. (5.11) and use Wick's theorem to get the elastic contribution to CGF, $\ln \chi_{\text{el}}(\lambda)$. Following the diagrammatic-codex of Fig. 5.2, we succeed to re-express $\ln \chi_{\text{el}}(\lambda)$ in terms of two topologically different Feynman diagrams. These diagrams are classified as type-E1 and type-E2 (see upper panel of Fig. 5.3). Following the standard technique of Feynman diagrammatic calculation with the GFs given in Eqs. (5.14), (5.15) and (5.16), we obtained the CGF contribution of type-E1 and type-E2 diagram. As detailed in Appendix 5.A, the CGF for 2SK effect contributed by the scattering effects is

$$\frac{\ln \chi_{\text{el}}}{(\alpha_e - \alpha_o)^2} = \frac{\mathcal{T}V}{24\pi} \frac{V^2 + 4(\pi T)^2}{\sinh(V/2T)} \sum_{x=\pm} \left(e^{-i\lambda x} - 1 \right) e^{xV/2T}. \quad (5.18)$$

We have used the generalized notation $e=\hbar=k_B=1$ to write Eq. (5.18) and for the rest of discussion. Plugging the Eq. (5.18) into Eq. (5.12) and then taking the limit $T \rightarrow 0$, we bring the zero temperature contribution of scattering effects to the n -th moment of charge current,

$$\mathcal{C}_n^{\text{el}} = \frac{V^3}{12\pi} (-1)^n (\alpha_e - \alpha_o)^2. \quad (5.19)$$

We follow the similar procedure, as for the calculation of scattering contribution, to get the interaction correction to CGF. Substituting the interaction (inelastic) part of Hamiltonian, H_{in} , into Eq. (5.11) and applying Wick's theorem, we obtain the Feynman diagrams accounting for the interaction effect in 2SK effect. These diagrams are shown in Fig. 5.4. We allocate these interaction correction diagrams into three topologically different classes, namely type-I1, type-I2 and type-I3 as shown in lower panel of Fig. 5.3. We introduce the notation, $\ln \chi_{\text{Ij}}(\lambda)$ ($j = 1, 2, 3$), to represent the interaction correction to CGF corresponding to the diagram of type-Ij. The real time GFs given in Eq. (5.17) pave the way for systematic calculation of $\ln \chi_{\text{Ij}}(\lambda)$. As detailed in Appendix 5.B, we write the type-I1 and type-I3 diagrammatic contribution to CGF as,

$$\begin{aligned} \ln \chi_{\text{I1/I3}} = & \pm \frac{\Phi^2 \mathcal{T}V}{24\pi} \left[\frac{V^2 + 4(\pi T)^2}{\sinh(V/2T)} \sum_{x=\pm} \left(e^{-i\lambda x} - 1 \right) e^{xV/2T} \right. \\ & \left. \pm 2 \frac{V^2 + (\pi T)^2}{\sinh(V/T)} \sum_{x=\pm} \left(e^{-2i\lambda x} - 1 \right) e^{xV/T} \right]. \end{aligned} \quad (5.20)$$

Furthermore, the type-I2 diagram produces the interaction correction to CGF as,

$$\ln \chi_{\text{I2}} = \frac{\Phi^2 \mathcal{T}V}{12\pi} \frac{V^2 + (\pi T)^2}{\sinh(V/T)} \sum_{x=\pm} \left(e^{-2i\lambda x} - 1 \right) e^{xV/T}. \quad (5.21)$$

Substituting Eqs. (5.20) and (5.21) into Eq. (5.12) we get the n -th order cumulant of charge current, $\mathcal{C}_n^{\text{Ij}}$, corresponding to the diagram type-Ij. Of particular interest, the zero temperature results are

$$\mathcal{C}_n^{\text{I1/I3}} = \pm \frac{V^3}{12\pi} (-1)^n [1 \pm 2^{n+1}] \Phi^2. \quad (5.22)$$

$$\mathcal{C}_n^{\text{I2}} = \frac{V^3}{12\pi} (-1)^n 2^{n+1} \Phi^2. \quad (5.23)$$

Collecting all the interaction contributions as detailed in Fig. 5.4, and the scattering contribution given in Eq. (5.19), we get the n -th cumulant of charge current at $T = 0$ as

$$\mathcal{C}_n = (-1)^n \frac{V^3}{6\pi} (\alpha_e - \alpha_o)^2 [1 + 2^n \mathcal{L}], \quad (5.24)$$

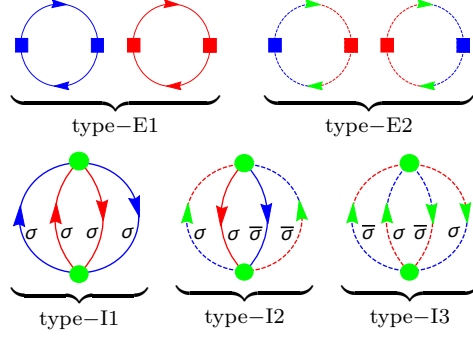


Figure 5.3: Upper panel: Schematic representation of the CGF contribution of scattering effects, $\ln \chi_{\text{el}}(\lambda)$. Lower panel: Topologically different diagrams accounting for the interaction contribution to the CGF, $\ln \chi_{\text{in}}(\lambda)$.

with

$$\mathcal{L} \equiv 1 + 9\mathcal{Z}, \quad \mathcal{Z} = \frac{(\Phi - 2/3\alpha_e)(\Phi - 2/3\alpha_o)}{(\alpha_e - \alpha_o)^2}. \quad (5.25)$$

The parameter \mathcal{Z} signifies the lack of universality away from the symmetry point, $\alpha_e = \alpha_o$ and $\Phi = 2/3 \alpha_a$ of 2SK Hamiltonian. Besides, it has been predicted that the parameter \mathcal{Z} is bounded such that $-1/9 \leq \mathcal{Z} \leq 0$ [2]. For the sake of simplicity, we introduce the new parameter \mathcal{L} ($\equiv 1 + 9\mathcal{Z}$) in such a way that $0 \leq \mathcal{L} \leq 1$. The minimum of \mathcal{L} corresponds to the exact symmetry between two channels at resonance. The case of infinite asymmetry between even and odd channel, $T_K^o/T_K^e \rightarrow 0$, is characterized by the upper bound of \mathcal{L} . This particular point, where the odd channel is decoupled from the impurity, recovers the 1CK paradigm. We see, from Eq. (5.24), that the n -th cumulant of charge current exactly vanishes at the symmetry point due to the destructive interference between two resonance channels. Same result holds true even at finite temperature. However, the l'Hopital's rule permits us to have the finite value of normalized n -th cumulant, $\mathcal{C}_n/\mathcal{C}_1$. Then we define the measure of backscattering via the generalized Fano factor

$$F \equiv |\mathcal{C}_2/\mathcal{C}_1| = \frac{1 + 4\mathcal{L}}{1 + 2\mathcal{L}}. \quad (5.26)$$

Plugging in the parameter \mathcal{L} into Eq. (5.26), we get the Fano factor bounded from upper and below in such a way that $1 \leq F \leq 5/3$. The upper bound reproduces the Fano factor of 1CK effect, the super-Poissonian charge transferred statistics [190]. The regime of maximum interaction in 2SK effect results the lower bound of F . This minimum of F ($= 1$) represent the Poissonian regime of charge distribution. Therefore, a generic 2SK effect exhibits the crossover regime of charge transferred statistics, from Poissonian to super-Poissonian, depending upon the channel asymmetry. This *monotonic* dependence of F on the channel-asymmetry parameter \mathcal{L} is shown in Fig. 5.5. The *non-monotonic* conductance of 2SK effect as a function of temperature, extracted from $\mathcal{C}_1|_{T \neq 0, V \rightarrow 0}$, is shown in the inset of Fig. 5.5 (see Ref. [2] for detailed description).

In 1CK schemes, the definition of generalized Fano factor follows from $F \equiv \delta\mathcal{C}_2/\delta\mathcal{C}_1|_{T \rightarrow 0}$, where $\delta\mathcal{C}_{1/2}$ represents the corresponding quantity after subtracting the linear part (those terms $\propto V$). Nevertheless, the n -th cumulant of charge current in 2SK schemes, the Eq. (5.24), does not

$$\begin{aligned}
 \mathcal{C}_n^{\phi^2} &= \left[\text{type-I1} \right] \\
 \mathcal{C}_n^{\Phi^2} &= +\frac{1}{4} \left[\text{type-I1} \right] \\
 &+ \frac{1}{4} \left[\text{type-I2} \right] \\
 &+ \frac{1}{4} \left[\text{type-I2} \right] \\
 &+ \frac{1}{4} \left[\text{type-I3} \right] \\
 \mathcal{C}_n^{\phi_a \Phi} &= -\frac{1}{2} \left[\text{type-I2} \right] \times 2 + \mathcal{C}_n^{\phi_o \Phi} \\
 \mathcal{C}_n^{\phi_a \phi_a} &= \left[\text{type-I3} \right]
 \end{aligned}$$

Figure 5.4: Feynman diagrams representing the second order interaction corrections to the CGF for 2SK model.

shows up the linear terms in V . This makes very straightforward extraction of F in 2SK effect, since it does not require the proper subtraction of linear terms.

The differential conductance of 2SK effect as a function of B (the Zeeman field), T and V

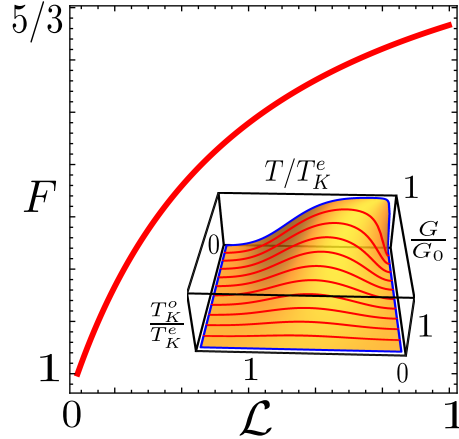


Figure 5.5: The evolution of Fano factor (F) as a function of channel asymmetry parameter (\mathcal{L}) for a generic 2SK effect. Inset: The non-monotonic conductance behavior, the major hallmark of 2SK effect (see text for detail).

is given, in terms of FL transport coefficients, as $G/G_0 = c_B B^2 + c_T (\pi T)^2 + c_V V^2$, where G_0 is the unitary conductance. The transport coefficients bear the compact form: $c_T/c_B = (\mathcal{L} + 2)/3$ and $c_V/c_B = \mathcal{L} + 1/2$ [2]. Thus, the measurement of \mathcal{L} would sufficient the study of transport behaviors of 2SK effect. The compelling monotonic dependence of F on \mathcal{L} , as shown in Fig. 5.5, could furnish an experimental way to extract \mathcal{L} as follows. Given an experimental setup in 2SK scheme, the independent measurements of charge current and noise impart the Fano factor. Thus obtained Fano factor uniquely defines the corresponding asymmetry parameter \mathcal{L} via Eq. (5.5). Following this way of measurements of transport coefficients could be less involved than measuring the response functions.

5.4 Summary

We extended the method FCS from conventional 1CK schemes to multi-channel Kondo paradigm. The developed framework of FCS has been demonstrated considering an example of 2SK effect. We analyzed the charge transferred statistics in the strong-coupling regime of a 2SK model using non-equilibrium Keldysh formulation. We found that the arbitrary cumulant of charge current get nullified at the symmetry point of 2SK model due to the destructive interference between two conducting channel. We studied the destructiveness/constructiveness of interference in terms of channel asymmetry parameter, \mathcal{L} . The n -th order normalized cumulant of charge current, $\mathcal{C}_n/\mathcal{C}_1$ is expressed into a compact function of \mathcal{L} , only. A bounded value of Fano factor, $1 \leq F \leq 5/3$, has been discovered. Studying the observed monotonic growth of F as a function of \mathcal{L} , we uncovered the cross-over regimes of charge transferred statistics in 2SK effect, from Poissonian to super-Poissonian. We proposed a novel way of obtaining the FL transport coefficients of 2SK effect by the independent measurements of charge current and noise. The developed formalism imparts all the transport informations of 1CK effect as well. All the calculations have been performed at finite temperature,

one can easily study the effect of temperature on an arbitrary cumulant of charge current.

Appendices

5.A Scattering corrections to the CGF

The scattering correction to the MGF of 2SK model reads

$$\chi_{\text{el}}(\lambda) = \left\langle T_C \exp \left[-i \int_C \mathcal{H}_{\text{el}}^\lambda(t) dt \right] \right\rangle_0. \quad (5.27)$$

Where the scattering Hamiltonian is given in Eq. (5.5). The logarithm of Eq. (5.27), $\ln \chi_{\text{el}}(\lambda)$, provides the corresponding CGF. The second order expansion of $\ln \chi_{\text{el}}(\lambda)$ in $\mathcal{H}_{\text{el}}^\lambda$ followed by the use of Wick's theorem results in four different Feynman diagrams as shown in Fig. 5.3 (upper panel). The first and second diagrams are composed of only the channel-diagonal GFs. Owing to their similar geometry, we classified them as type-E1 diagram. Note that, in our convention, the two diagrams are geometrically similar if they contain equal number of channel-diagonal GFs (if present) and equal number of mixed-GFs (if present). The type-E2 diagrams shown in Fig. 5.3, nonetheless, consist of only mixed-GFs. The interference between two channels, due to the scattering effects, is accounted for by these type-E2 diagrams. The contribution of type-E1 diagrams to the CGF is proportional to α_a^2 . Similarly, the CGF contribution of type-E2 diagrams is proportional to $\alpha_a \alpha_{\bar{a}}$. Therefore, the overall scattering contribution to CGF is written as

$$\ln \chi_{\text{el}} = \sum_a (\ln \chi_{\alpha_a^2} + \ln \chi_{\alpha_a \alpha_{\bar{a}}}). \quad (5.28)$$

Topologically the type-E1 and type-E2 diagrams are quite distinct. The type-E1 diagrams have been already appeared in several previous works [93–97], however, the type-E2 diagrams has not been considered yet. For completeness, we present the mathematical details of diagrammatic contribution to CGF for both diagrams. For type-E1 diagrams we write

$$\ln \chi_{\alpha_a^2} = -\frac{1}{2} \frac{\alpha_a^2}{(2\pi\nu)^2} \sum_{kk'\sigma} \sum_{pp'\sigma'} (\varepsilon_k + \varepsilon_{k'}) (\varepsilon_p + \varepsilon_{p'}) \int_C dt_1 dt_2 \left\langle T_C b_{ak\sigma}^\dagger(t_1) b_{ak'\sigma}(t_1) b_{ap'\sigma'}^\dagger(t_2) b_{ap'\sigma'}(t_2) \right\rangle. \quad (5.29)$$

Here, we introduced the set of momentum indices (k, k', p, p') , spin indices (σ, σ') and time indices (t_1, t_2) . Equation. (5.29) provides the non-zero contribution only if $k = p'$, $k' = p$ and $\sigma = \sigma'$. Therefore, use of the method of Keldysh disentanglement to the Eq. (5.29) results in

$$\ln \chi_{\alpha_a^2} = -\frac{1}{2} \frac{\alpha_a^2 \mathcal{T}}{(2\pi\nu)^2} \sum_{kk'\sigma} (\varepsilon_k + \varepsilon_{k'})^2 \sum_{\eta_1 \eta_2} \eta_1 \eta_2 \int_C dt \mathcal{G}_{aa,k'\sigma}^{\eta_1 \eta_2}(t) \mathcal{G}_{aa,k\sigma}^{\eta_2 \eta_1}(-t), \quad (5.30)$$

where, \mathcal{T} is the measurement time (see Section 5.3), η_i ($i = 1, 2$) are the Keldysh branch (forward and backward) indices such that $\eta_i = \pm 1$. The channel-diagonal GFs, $\mathcal{G}_{aa}^{\eta_1 \eta_2}$, are defined in

Eqs. (5.14), (5.15) and (5.16). These GFs acquire the special property; $\nu \mathcal{G}_{aa,k\sigma}^{\eta_1\eta_2}(\varepsilon) = \mathcal{G}_{aa,\sigma}^{\eta_1\eta_2}(\varepsilon)\delta(\varepsilon - \varepsilon_k)$, where $\delta(\varepsilon - \varepsilon_k)$ stands for the Kronecker delta symbol. Then, Eq. (5.30) reads

$$\ln \chi_{\alpha_a^2} = -\frac{1}{2} \frac{\alpha_a^2 \mathcal{T}}{(\pi\nu)^2} \sum_{\eta_1\eta_2,\sigma} \eta_1\eta_2 \int_{\mathcal{C}} \frac{d\varepsilon}{2\pi} \varepsilon^2 \mathcal{G}_{aa,\sigma}^{\eta_1\eta_2}(\varepsilon) \mathcal{G}_{aa,\sigma}^{\eta_2\eta_1}(\varepsilon). \quad (5.31)$$

Summing Eq. (5.31) over $\eta_{1/2}$ and then plugging in the various Keldysh GFs from Eqs. (5.14), (5.15) and (5.16) leads

$$\ln \chi_{\alpha_a^2} = \frac{\alpha_a^2 \mathcal{T}}{2\pi} \sum_{\sigma} \mathcal{J}_{\text{el},\sigma}, \quad (5.32)$$

with the compact form of the integral characterizing the scattering effects

$$\mathcal{J}_{\text{el}} = \int_{-\infty}^{\infty} \varepsilon^2 d\varepsilon \left[f_S(1-f_D)(e^{-i\lambda}-1) + f_D(1-f_S)(e^{i\lambda}-1) \right]. \quad (5.33)$$

We called this integral as the ‘‘elastic integral’’, the mathematical details of the computation of this diagram will be discussed in Appendix 5.C.

Repeating all above calculations for type-E2 diagrams with same notations we get the quite similar result

$$\ln \chi_{\alpha_a\alpha_{\bar{a}}} = -\frac{\alpha_a\alpha_{\bar{a}}\mathcal{T}}{2\pi} \sum_{\sigma} \mathcal{J}_{\text{el},\sigma}. \quad (5.34)$$

Though the origin of these two elastic diagrams and corresponding topology is very different, it turns out that they produce equal but opposite contribution to the CGF. Plugging in the Eqs. (5.32) and (5.34) into Eq. (5.28) provides the contribution of scattering effects to the CGF, which is written as

$$\ln \chi_{\text{el}} = \frac{(\alpha_e - \alpha_0)^2 \mathcal{T}}{2\pi} \sum_{\sigma} \mathcal{J}_{\text{el},\sigma}. \quad (5.35)$$

Substituting the value of elastic integral from Eq. (5.54) into Eq. (5.35), we get the final expression for the scattering contribution to the CGF in 2SK model, which is the Eq. (5.18) in the main text of this chapter.

5.B Interaction corrections to the CGF

In the same way and using the same notations as for the scattering contribution, we get several Feynman diagrams contributing to the CGF of 2SK model as shown in Fig. 5.4. These diagrams are classified into three different group, type-Ij (j=1, 2, 3) diagram, based upon the numbers of channel-diagonal GFs and mixed-GFs present in a particular diagram (see the lower panel of Fig. 5.3). For instance, the diagram with all (four) channel-diagonal GFs has been classified as type-I1 diagram, those with two channel-diagonal and remaining two mixed-GFs as the type-I2 and diagrams with all mixed-GFs has been termed as type-I3. As shown in the Fig. 5.4, we expressed the interaction contribution to the CGF in terms of these three diagrams. The two diagrams belonging to the same group might have different weight factor. The numbers of close fermion loops, the product

of Pauli matrices and the renormalization factor in the Hamiltonian determines the weight factor corresponding to a particular diagram (for detail see Ref. [2]).

A single diagram of type-I1 (with CGF contribution proportional to $\phi_{e/o}^2$) completely characterizes the FCS of 1CK schemes [93–97]. However, the type-I2 and type-I3 diagrams are generic feature of multi-channel, multi-stage screening effects. These diagrams have not been studied yet. In this Appendix 5.B we provide the mathematical details of computing CGF contribution of type-Ij diagram.

The type-I1 diagram shown in lower panel of Fig. 5.3 produces the CGF contribution proportional to Φ^2 . Following the standard technique of Feynman diagram calculation, we cast the CGF contribution of type-I1 diagram into the form

$$\ln \chi_{I1} = -\frac{1}{2} \left(\frac{\Phi}{\pi\nu} \right)^2 \int_{\mathcal{C}} dt_1 dt_2 \left[\mathcal{G}_{ee,\sigma}(t_1 - t_2) \mathcal{G}_{ee,\sigma}(t_2 - t_1) \mathcal{G}_{oo,\sigma}(t_1 - t_2) \mathcal{G}_{oo,\sigma}(t_2 - t_1) \right]. \quad (5.36)$$

In Eq. (5.36) we did not consider the spin summation for being more general (implying that the spin index σ is either down or up). Using the technique of Keldysh disentanglement we rewrite the Eq. (5.36) as

$$\ln \chi_{I1} = -\frac{\mathcal{T}}{2} \left(\frac{\Phi}{\pi\nu} \right)^2 \sum_{\eta_1 \eta_2} \eta_1 \eta_2 \times \int_{\mathcal{C}} dt \left[\mathcal{G}_{ee,\sigma}^{\eta_1 \eta_2}(t) \mathcal{G}_{ee,\sigma}^{\eta_2 \eta_1}(-t) \mathcal{G}_{oo,\sigma}^{\eta_1 \eta_2}(t) \mathcal{G}_{oo,\sigma}^{\eta_2 \eta_1}(-t) \right]. \quad (5.37)$$

Summing Eq. (5.37) over Keldysh indices $\eta_{1/2}$ and using the expressions of GFs in Eq. (5.17), we get

$$\ln \chi_{I1} = (\pi\Phi T^2)^2 \mathcal{T} \int_{-\infty+i\gamma}^{\infty+i\gamma} \frac{\cos^4\left(\frac{\lambda}{2} + \frac{V}{2}t\right)}{\sinh^4(\pi T t)} dt. \quad (5.38)$$

Coming from Eq. (5.37) to Eq. (5.38), we retain only the λ -dependent terms. The integral Eq. (5.38) is computed in Appendix 5.D. Then we write the CGF contribution of type-I1 diagram into the form

$$\begin{aligned} \ln \chi_{I1} = & \frac{\Phi^2 \mathcal{T}}{96\pi} \left[\frac{8V(V^2 + (\pi T)^2)}{\sinh(V/T)} \sum_{x=\pm} e^{2ix\lambda} e^{-xV/T} \right. \\ & \left. \frac{4V(V^2 + 4(\pi T)^2)}{\sinh(V/2T)} \sum_{x=\pm} e^{ix\lambda} e^{-xV/2T} \right] + \frac{\pi\Phi^2 T^3 \mathcal{T}}{2}. \end{aligned} \quad (5.39)$$

For proper renormalization of PDF we subtract the $\lambda = 0$ contribution of Eq. (5.39) from the same Eq. (5.39), to write the final expression of CGF contributed by a diagram of type-I1

$$\begin{aligned} \ln \chi_{I1} = & \frac{\Phi^2 \mathcal{T} V}{24\pi} \left[2 \cdot \frac{V^2 + (\pi T)^2}{\sinh(V/T)} \sum_{x=\pm} \left(e^{2ix\lambda} - 1 \right) e^{-xV/T} \right. \\ & \left. + \frac{V^2 + 4(\pi T)^2}{\sinh(V/2T)} \sum_{x=\pm} \left(e^{ix\lambda} - 1 \right) e^{-xV/2T} \right]. \end{aligned} \quad (5.40)$$

In the same way and using the same notations as for the type-I1 diagram, the CGF contribution of type-I2 diagram as shown in Fig. 5.3 reads

$$\ln \chi_{I2} = -(\pi\Phi T^2)^2 \mathcal{T} \int_{-\infty+i\gamma}^{\infty+i\gamma} \frac{\sin^2\left(\frac{\lambda}{2} + \frac{V}{2}t\right) \cos^2\left(\frac{\lambda}{2} + \frac{V}{2}t\right)}{\sinh^4(\pi T t)} dt. \quad (5.41)$$

Using the integral given in Appendix 5.D followed by the proper renormalization of PDF, the Eq. (5.41) results in

$$\ln \chi_{I2} = \frac{\Phi^2 \mathcal{T} V}{12\pi} \frac{V^2 + (\pi T)^2}{\sinh(V/T)} \sum_{x=\pm} \left(e^{2ix\lambda} - 1 \right) e^{-xV/T}. \quad (5.42)$$

Similarly, the CGF contribution of a type-I3 diagram as shown in Fig. 5.3 is given by

$$\ln \chi_{I3} = (\pi \Phi T^2)^2 \mathcal{T} \int_{-\infty+i\gamma}^{\infty+i\gamma} \frac{\sin^4\left(\frac{\lambda}{2} + \frac{V}{2}t\right)}{\sinh^4(\pi T t)} dt. \quad (5.43)$$

The simplification of Eq. (5.43) upon proper renormalization of PDF imparts

$$\begin{aligned} \ln \chi_{I3} = & -\frac{\Phi^2 \mathcal{T} V}{24\pi} \left[\frac{V^2 + 4(\pi T)^2}{\sinh(V/2T)} \sum_{x=\pm} \left(e^{ix\lambda} - 1 \right) e^{-xV/2T} \right. \\ & \left. - 2 \cdot \frac{V^2 + (\pi T)^2}{\sinh(V/T)} \sum_{x=\pm} \left(e^{2ix\lambda} - 1 \right) e^{-xV/T} \right]. \end{aligned} \quad (5.44)$$

5.C Elastic integral

This section contains the detail of the calculation of the elastic integral Eq. (5.33) using the properties of Fourier transform (FT). First we factorized the elastic integral as,

$$\mathcal{J}_{\text{el}} = (e^{-i\lambda} - 1) \mathcal{J}_{\text{el}}^1 + (e^{i\lambda} - 1) \mathcal{J}_{\text{el}}^2. \quad (5.45)$$

Here, we introduced the short hand notations;

$$\mathcal{J}_{\text{el}}^1 = \int_{-\infty}^{\infty} \varepsilon^2 d\varepsilon f_S(1-f_D), \quad \mathcal{J}_{\text{el}}^2 = \int_{-\infty}^{\infty} \varepsilon^2 d\varepsilon f_D(1-f_S). \quad (5.46)$$

At $T = 0$ we have, $f_{S/D}(\varepsilon) = \Theta(\mu_{S/D} - \varepsilon)$ and $1 - f_{S/D}(\varepsilon) = \Theta(\varepsilon - \mu_{S/D})$. Thus the zero temperature limit of Eq. (5.45) is quite trivial

$$\mathcal{J}_{\text{el}}|_{T=0} = (e^{-i\lambda} - 1) \int_{\mu_R}^{\mu_L} \varepsilon^2 d\varepsilon = (e^{-i\lambda} - 1) \frac{V^3}{12}. \quad (5.47)$$

However, the Fermi distribution functions of the source and drain, and their FT at finite temperature are

$$f_{S/D}(\varepsilon) = \frac{e^{-(\varepsilon - \mu_{S/D})/2T}}{2 \cosh[(\varepsilon - \mu_{S/D})/2T]}; \quad f_{S/D}(t) = \frac{iT}{2} \frac{e^{-it\mu_{S/D}}}{\sinh(\pi T t)}. \quad (5.48)$$

For the sake of simplicity we define another function $h_{L/R}(\varepsilon)$ and its FT as

$$h_{S/D}(\varepsilon) = e^{-\frac{\varepsilon}{T}} f_{S/D}(\varepsilon); \quad h_{S/D}(t) = -\frac{iT}{2} \frac{e^{-it\mu_{S/D} - \frac{\mu_{S/D}}{T}}}{\sinh(\pi T t)}. \quad (5.49)$$

The function $h_{S/D}(\varepsilon)$ in Eq. (5.49) imparts the way to convert the product of Fermi functions into weighted sum. For instance,

$$f_S(\varepsilon) f_D(\varepsilon) = \frac{h_S(\varepsilon) - h_D(\varepsilon)}{e^{-\frac{\mu_D}{T}} - e^{-\frac{\mu_S}{T}}} = \frac{h_S(\varepsilon) - h_D(\varepsilon)}{2 \sinh(V/2T)}. \quad (5.50)$$

Then, $\mathcal{J}_{\text{el}}^1$ and $\mathcal{J}_{\text{el}}^2$ get simplified to

$$\mathcal{J}_{\text{el}}^{1/2} = \int_{-\infty}^{\infty} \varepsilon^2 d\varepsilon f_{S/D}(\varepsilon) - \frac{\int_{-\infty}^{\infty} \varepsilon^2 d\varepsilon [h_L(\varepsilon) - h_R(\varepsilon)]}{2 \sinh(V/2T)}. \quad (5.51)$$

Having defined the FT of the functions $f_{S/D}$ and $h_{S/D}$, we performed the integration of Eq. (5.51) by using the property of FT [2],

$$\int_{-\infty}^{\infty} \varepsilon^n y(\varepsilon) d\varepsilon = \frac{2\pi}{(-i)^n} \partial_t^n [y(t)]|_{t=0}. \quad (5.52)$$

Here, $y(\varepsilon)$ is an arbitrary function with FT $y(t)$ and ∂_t^n represents the n -th order differentiation with respect to t . Substitution of Eq. (5.52) for $n=2$ into Eq. (5.51) and then using the definitions of $f_{S/D}(t)$ and $h_{S/D}(t)$ defined in Eqs. (5.48) and (5.49) leads the result

$$\mathcal{J}_{\text{el}}^{1/2} = \pm \frac{V}{2} \left[\frac{(\pi T)^2}{3} + \frac{V^2}{12} \right] \times \left[1 \pm \coth \left(\frac{V}{2T} \right) \right]. \quad (5.53)$$

Plugging in $\mathcal{J}_{\text{el}}^{1/2}$, from Eq. (5.53), into Eq. (5.45) we obtain the final expression for the elastic integral

$$\mathcal{J}_{\text{el}} = \frac{V}{24} \frac{V^2 + 4(\pi T)^2}{\sinh(V/2T)} \left[(e^{-i\lambda} - 1)e^{V/2T} + (e^{i\lambda} - 1)e^{-V/2T} \right]. \quad (5.54)$$

This is the central equation governing the CGF contribution of scattering effects in 2SK model.

5.D Inelastic Integral

For the computation of integrals in Eqs. (5.38), (5.41) and (5.43), we expand their numerators in powers of $e^{\pm i(\lambda/2 + Vt/2)}$. Each term gives an integral of the form

$$\mathcal{I}_{\pm} = \int_{-\infty+i\gamma}^{\infty+i\gamma} \frac{e^{\pm i\mathcal{A}t}}{\sinh^4(\pi Tt)} dt, \quad \mathcal{A} > 0. \quad (5.55)$$

The singularity of the integral in Eq. (5.55) is removed by shifting the time contour by $i\gamma$ in the complex plane such that $\gamma D \gg 1$, $\gamma T \ll 1$ and $\gamma \mathcal{A} \ll 1$. Here, D is the band cutoff. The poles of the integrand of \mathcal{I}_{\pm} are given by the solution of $\sinh(\pi Tt) = 0$ for t . Which leads,

$$\pi Tt = \pm im\pi \Rightarrow t = \pm \frac{im}{T}, \quad m = 0, \pm 1, \pm 2, \pm 3 \dots$$

With the choice of the rectangular contour shifted by i/T in the complex plane which includes the pole of the integrand at $t = 0$, the standard method of complex integration results in

$$\mathcal{I}_+ \left(1 - e^{\mathcal{A}/T} \right) = -2\pi i \times \text{Res}|_{t=0}, \quad (5.56)$$

where $\text{Res}|_{t=0}$ stands for Cauchy residue of the integrand in Eq. (5.55) at $t = 0$. Plugging in the residue into Eq. (5.56) results in

$$\mathcal{I}_+ = - \frac{2\pi (\mathcal{A}^3 + 4\mathcal{A}(\pi T)^2)}{6(\pi T)^4} \times \frac{1}{1 - e^{\mathcal{A}/T}}. \quad (5.57)$$

Similarly we computed \mathcal{I}_- . These integrals \mathcal{I}_{\pm} are sufficient for the computation of all the inelastic diagrams shown in Fig. 5.4.

Chapter 6

Conclusions and perspectives

In this thesis we developed a low energy theory of thermoelectric transport through a multi-level Kondo impurity based on the multi-color Fermi-liquid (FL) theory in combination with non-equilibrium Keldysh approach. In particular, the quantum transport through the strong-coupling regime of spin-1/2 and spin-1 quantum impurity tunnel coupled to two conducting reservoirs has been investigated. The effects of voltage bias and temperature gradient are consistently described within the out-of-equilibrium Keldysh framework. Note that, though both setups considered in this thesis fall into the same universality class described by a local FL theory, they are characterized by strikingly different transport fingerprints. The findings of this thesis could be useful for low temperature quantum technologies, and significantly improve the understanding of the many-body physics associated with the strongly-correlated electronic systems. This thesis not only suggests possible resolution of some long-standing puzzle observed in the experiment but also propose some new experiments to understand further the nano scale transport properties. The outcomes of this work are divided into two broad categories: i) investigation of thermoelectric transport through the $SU(N)$ Kondo impurity as presented in chapter 2 and chapter 3, and ii) exploration of charge transport statistics in the strong-coupling regime of the generic multi-stage Kondo effect composing the chapter 4 and chapter 5 of this thesis.

The emergent particle-hole (PH) symmetry at the low energy regime of conventional $SU(2)$ spin $S=1/2$ Kondo effects tends to produce vanishingly small thermopower since the current carried by the hole exactly compensates that by the electrons. Interestingly, the difficulty associated with the undesirable PH symmetry can be elegantly circumvented by uplifting the degeneracy of Kondo ground state. Therefore, we chose to explore the thermoelectric associated with the general $SU(N \geq 2)$ Kondo impurity motivated by the recent experiments on carbon nano tubes and double quantum dot setups [36, 68–74]. The paradigmatic $SU(N)$ Kondo effect offer lots of freedom on the electron occupancy m , which can takes all the possible values starting from 1 to $N-1$ resulting in various filling factors m/N . Therefore, unlike the $N=2$ case, for general N the $SU(N)$ model allows a nontrivial occupation away from half filling. For such occupations PH symmetry is lifted, which results in a much larger thermoelectric response than in the presence of PH symmetry. Note that the broken PH symmetry within $SU(N)$ Kondo model is not analogous to the other systems beyond

PH symmetric regime. In the $SU(N)$ regime, the strong interplay of filling factor and Kondo resonance allows to be away from the PH symmetric regime but still utilizing the advantage (enhanced electronic feature) of Kondo effect thereby producing a giant thermopower or the power output. In this work, the thermoelectric performance of a $SU(N)$ Kondo impurity has been characterized via two reciprocal measurements, namely the Seebeck coefficient (thermopower) and Peltier coefficient. From the information of electronic conductance and thermoelectric coefficient, we analyzed the maximum power output of a heat engine in $SU(N)$ Kondo regime. As presented in chapter 2, about 50% of quantum upper bound of power output can be easily produced with the $SU(N)$ Kondo impurity. Though the power output per degeneracy is half of the quantum upper bound, the $SU(N)$ Kondo effect provides an universal mean of increasing total power production by increasing both the degeneracy factor N and the electron occupation factor m as far as the filling factor of $m/N \sim 1/6$ is mentioned. This is because, as revealed in chapter 2, the power production grows linearly with N for some suitable choice of electron occupancy. After analyzing the output power of a heat engine in $SU(N)$ Kondo regime and its relation with the corresponding non-interacting upper bound, we moved to the investigation of nonlinear effects on the thermoelectric characterization as presented in chapter 3. We identified all the thermoelectric transport coefficients characterizing the charge current through the $SU(N)$ Kondo impurity up to the cubic response coefficients in voltage bias and temperature gradient. By solving the zero charge current condition, we analyzed the thermopower associated with the linear and nonlinear effects. The nonlinear effects are found to be very significant at low temperature regime since the investigated nonlinear thermopower always overshoots the corresponding linear response contribution. In addition, we explained this finite offset associated with nonlinear thermopower in relation to the long-standing experimental puzzle of thermo-voltage offset in the $SU(2)$ Kondo effect [32] and suggested some new experiments to clarify further the issue of observed offset. The developed theoretical framework is also able to capture the influence of coupling asymmetry on the low energy thermoelectric of a $SU(N)$ Kondo impurity. We explored the greatly enhanced thermopower by tailoring the coupling asymmetry of beyond PH-symmetric $SU(N)$ Kondo effects. Our investigation related to the enhancing thermopower via properly engineering of coupling asymmetry could also be of great value for the propose of temperature sensing. Summarizing, in chapter 2 and chapter 3, we presented a very general theoretical framework for the description of thermoelectric in the strong-coupling regime of a $SU(N)$ Kondo impurity and various measures of thermoelectric such as upper bound of power output, thermopower and Peltier coefficients are explored in fully nonlinear regime. These findings have open diverse valid avenues for future research, both theoretical and experimental. Our formalism could be easily extended for the exploration of thermoelectric in AB-interferometer with embedded $SU(N)$ Kondo impurity, which is still an open fundamental problem of the field. Embedding a $SU(N)$ Kondo impurity in one arm of AB-ring leaving another arm open, one can also study the coherent properties (such as transmission phase shifts and normalized visibility) of Kondo correlated systems described by higher symmetry group in the spirit of seminal work [120]. Likewise, thermoelectric description with multi-terminal $SU(N)$ Kondo impurity also appears to be a valid avenue for future research. The presented theory could also be of great value while investigating the magneto-Seebeck effect associated with the $SU(N)$ Kondo impurity, to the best of our knowledge, this is also the open problem persisting for many years. In addition, the presented framework would be useful for the

study of gate voltage dependences on the thermoelectric of a $SU(N)$ quantum impurity.

The transport properties of Kondo correlated system studied in chapter 2 and chapter 3 has been limited to the setup with $S=1/2$ quantum impurity described by the single-level Anderson model. In many cases truncation of the impurity spectrum to one level is not possible and besides, there are several orbitals of conduction electrons which interact with the higher spin $S>1/2$ of the localized magnetic impurity, giving rise to the phenomenon of multistage, multichannel Kondo screening [47–49, 135]. Therefore in the chapter 4 and chapter 5, we investigated the low energy transport properties of the spin $S=1$ Kondo effect as a prototypical example of multi-stage Kondo screening mechanism. The spin $S=1$ Kondo impurity tunnel coupled to two conducting reservoirs results in the fully-screened ground state in two separate processes: the first stage consist of under-screened $S=1/2$ Kondo effect which subsequently got fully-screened at the second stage. This two stage screening mechanism is generic for any systems containing two interacting resonance channels. Unlike the $S=1/2$ Kondo effect, the two stage Kondo effect occurring with the $S=1$ quantum impurity results in the non-monotonic conductance as a function of temperate (similarly with the magnetic filed or the voltage bias). Thought, the non-monotonic nature of conductance has been reported in several previous theoretical and experimental work [47], complete explanation of the strong-coupling regime of the problem has remained open for almost two decades. The main difficulty for the description of the strong-coupling regime of two-stage Kondo effect has been associated with the fact that both channels are interacting with the quantum impurity and are close the the resonance. Consistent transport description, thus, requires to introduce the inter-channel interaction in addition to the intra-channel interaction. The lack of correct form of the inter-channel interaction was one of the problem for the persistence of this open problem for many years. The channel interaction, if known, introduces the vertex-correction in the theory which adds the complexity problem in great amount. However, in this contribution, we developed a theoretical framework for the description of quantum transport in the strong-coupling regime of the two-stage Kondo effect based on the local FL theory. By using the current algebra approach, we first constructed the low energy Hamiltonian of the problem including both intra- and inter-channel interactions. Using the low energy Hamiltonian, we calculated the charge current following out of the $S=1$ Kondo impurity using fully-fledged Keldysh out of equilibrium approach. The introduction of the inter-channel interaction has resulted to produce six topologically different transport diagrams (current, noise etc.); two for elastic effects and remaining for the interactions associated with the FL quasi-particles. Note that for the single channel two diagrams, one for elastic effects and the other for the interactions, would be enough for the low energy transport description. The four new diagrams, appeared in our work, in addition to the two conventional diagrams (characterizing single channel Kondo effects) are also the new finding of this project. After computing all the diagrams using Keldysh approach, we analyzed the new emergent symmetry of the problem and computed all the FL transport coefficients characterizing the effects of magnetic field (Zeeman field), temperature and voltage bias in strongly nonlinear regime. The significant deviation of FL coefficients from the corresponding single channel values are observed and explained in terms of the asymmetry of the two Kondo temperature of the resonance channels. With this contribution, we believe that, the long-standing problem for the explanation of non-monotonic

conductance in two-stage Kondo effect has been closed. In addition, we developed a method of full counting statistics applicable to the multi-stage Kondo paradigm in order to analyze all the moments of corresponding charge current. The investigation of charge current in two-stage Kondo effect and the noise associated with it allowed us to explore the Fano factor quantifying the effective charge of FL quasi particles. We proposed a novel way of measuring all the FL transport coefficient of two-stage Kondo paradigm by the independent measurements of charge current and its noise. Note that, though we restrict ourself for the investigation of Kondo effect, the multi-stage transport framework developed in this work would be applicable to any systems with two interacting resonance channels (not necessarily of the Kondo origin). Furthermore, the transport diagrams identified in this work would be enough for the extension of our two-stage Kondo theory for the general $SU(N)$ spin system. Generalizing our work to the $SU(N)$ systems and computing the thermoelectric response in multi-stage Kondo setup would be the ambitious future research project. We also believe that the extensive ongoing research for the spin-1/2 Kondo effects in cold atomic setup would be soon pointing towards the search of multi-stage Kondo paradigm.

Bibliography

- [1] D. B. Karki and M. N. Kiselev, “Thermoelectric transport through a $SU(N)$ Kondo impurity,” Phys. Rev. B, vol. 96, p. 121403, Sep 2017.
- [2] D. B. Karki, C. Mora, J. von Delft, and M. N. Kiselev, “Two-color Fermi-liquid theory for transport through a multilevel Kondo impurity,” Phys. Rev. B, vol. 97, p. 195403, May 2018.
- [3] D. B. Karki and M. N. Kiselev, “Full counting statistics of the two-stage Kondo effect,” Phys. Rev. B, vol. 98, p. 165443, Oct 2018.
- [4] D. B. Karki and M. N. Kiselev, “Effects of strong electron interactions and resonance scattering on power output of nano-devices,” arXiv e-prints, p. arXiv:1906.00724v2, Jun 2019.
- [5] D. B. Karki and M. N. Kiselev, “Nonlinear Seebeck effect of $SU(N)$ Kondo impurity,” Phys. Rev. B, vol. 100, p. 125426, Sep 2019.
- [6] W. de Haas, J. de Boer, and G. van den Berg, “The electrical resistance of gold, copper and lead at low temperatures,” Physica, vol. 1, no. 7, pp. 1115 – 1124, 1934.
- [7] J. Kondo, “Resistance Minimum in Dilute Magnetic Alloys,” Progress of Theoretical Physics, vol. 32, pp. 37–49, 07 1964.
- [8] L. Kouwenhoven and L. Glazman, “Revival of the Kondo effect,” Physics World, vol. 14, no. 1, p. 33, 2001.
- [9] K. G. Wilson, “The renormalization group: Critical phenomena and the Kondo problem,” Rev. Mod. Phys., vol. 47, pp. 773–840, Oct 1975.
- [10] A. Hewson, The Kondo Problem to Heavy Fermions. Cambridge University Press, Cambridge, 1993.
- [11] T. A. Costi, A. C. Hewson, and V. Zlatic, “Transport coefficients of the Anderson model via the numerical renormalization group,” Journal of Physics: Condensed Matter, vol. 6, pp. 2519–2558, mar 1994.
- [12] A. F. G. Wyatt, “Anomalous Densities of States in Normal Tantalum and Niobium,” Phys. Rev. Lett., vol. 13, pp. 401–404, Sep 1964.
- [13] R. A. Logan and J. M. Rowell, “Conductance Anomalies in Semiconductor Tunnel Diodes,” Phys. Rev. Lett., vol. 13, pp. 404–406, Sep 1964.

-
- [14] J. Appelbaum, “ $s - d$ Exchange Model of Zero-Bias Tunneling Anomalies,” Phys. Rev. Lett., vol. 17, pp. 91–95, Jul 1966.
- [15] C. B. Duke, Tunneling in solids. New York, Academic Press, 1969.
- [16] P. W. Anderson and G. Yuval, “Exact Results in the Kondo Problem: Equivalence to a Classical One-Dimensional Coulomb Gas,” Phys. Rev. Lett., vol. 23, p. 89, 1969.
- [17] P. W. Anderson, G. Yuval, and D. R. Hamann, “Exact Results in the Kondo Problem. II. Scaling Theory, Qualitatively Correct Solution, and Some New Results on One-Dimensional Classical Statistical Models,” Phys. Rev. B, vol. 1, p. 4464, 1970.
- [18] M. Fowler and A. Zawadowski, “Scaling and the renormalization group in the kondo effect,” Solid State Communications, vol. 9, no. 8, pp. 471 – 476, 1971.
- [19] G. Gruner and A. Zawadowski, “Magnetic impurities in non-magnetic metals,” Reports on Progress in Physics, vol. 37, pp. 1497–1583, dec 1974.
- [20] P. Nozieres, “A fermi-liquid description of the Kondo problem at low temperatures,” J. Low Temp. Phys., vol. 17, pp. 31–42, 1974.
- [21] P. W. Anderson, “Localized Magnetic States in Metals,” Phys. Rev., vol. 124, pp. 41–53, Oct 1961.
- [22] P. Nozieres and A. Blandin, “Kondo effect in real metals,” J. Phys, vol. 41, no. 3, pp. 193–211, 1980.
- [23] I. Affleck, “A current algebra approach to the Kondo effect,” Nuclear Physics B, vol. 336, no. 3, pp. 517 – 532, 1990.
- [24] I. Affleck and A. W. W. Ludwig, “Exact conformal-field-theory results on the multichannel Kondo effect: Single-fermion Green’s function, self-energy, and resistivity,” Phys. Rev. B, vol. 48, no. 10, pp. 7297–7321, 1993.
- [25] I. Affleck, “Conformal Field Theory Approach to the Kondo Effect,” Acta Polonica B, vol. 26, no. 12, pp. 1869 – 1931, 1995.
- [26] D. L. Cox and A. Zawadowski, “Exotic Kondo effects in metals: Magnetic ions in a crystalline electric field and tunnelling centres,” Adv. Phys., vol. 47, pp. 599–942, 1998.
- [27] D. Goldhaber-Gordon, H. Shtrikman, D. Mahalu, D. Abusch-Magder, U. Meirav, and M. A. Kastner, “Kondo effect in a single-electron transistor,” Nature, vol. 391, pp. 156–159, 1998.
- [28] S. M. Cronenwett, T. H. Oosterkamp, and L. P. Kouwenhoven, “A Tunable Kondo Effect in Quantum Dots,” Science, vol. 281, pp. 540–543, 1998.
- [29] M. Pustilnik and L. Glazman, “Kondo effect in quantum dots,” J. Phys.: Condens. Matter, vol. 16, p. R513, 2004.

- [30] S. De Franceschi, R. Hanson, W. G. van der Wiel, J. M. Elzerman, J. J. Wijkema, T. Fujisawa, S. Tarucha, and L. P. Kouwenhoven, “Out-of-Equilibrium Kondo Effect in a Mesoscopic Device,” Phys. Rev. Lett., vol. 89, p. 156801, Sep 2002.
- [31] P. Coleman, Introduction to Many-Body Physics. Cambridge University Press, Cambridge, 2015.
- [32] R. Scheibner, H. Buhmann, D. Reuter, M. N. Kiselev, and L. W. Molenkamp, “Thermopower of a Kondo Spin-Correlated Quantum Dot,” Phys. Rev. Lett., vol. 95, p. 176602, Oct 2005.
- [33] S. Jezouin, F. D. Parmentier, A. Anthore, U. Gennser, A. Cavanna, Y. Jin, and F. Pierre, “Quantum Limit of Heat Flow Across a Single Electronic Channel,” Science, vol. 342, no. 6158, pp. 601–604, 2013.
- [34] Z. Iftikhar, S. Jezouin, A. Anthore, U. Gennser, F. D. Parmentier, A. Cavanna, and F. Pierre, “Two-channel Kondo effect and renormalization flow with macroscopic quantum charge states,” Nature, vol. 526, pp. 233–236, OCTOBER 8 2015.
- [35] S. Jezouin, Z. Iftikhar, A. Anthore, F. D. Parmentier, U. Gennser, A. Cavanna, A. Ouerghi, I. P. Levkivskyi, E. Idrisov, E. V. Sukhorukov, L. I. Glazman, and F. Pierre, “Controlling charge quantization with quantum fluctuations,” Nature, vol. 536, pp. 60–62, AUGUST 4 2016.
- [36] M. Ferrier, T. Arakawa, T. Hata, R. Fujiwara, R. Delagrangé, R. Weil, R. Deblock, R. Sakano, A. Oguri, and K. Kobayashi, “Universality of non-equilibrium fluctuations in strongly correlated quantum liquids,” Nature Physics, vol. 12, p. 230, 2016.
- [37] A. Svilans, M. Josefsson, A. M. Burke, S. Fahlvik, C. Thelander, H. Linke, and M. Leijnse, “Thermoelectric Characterization of the Kondo Resonance in Nanowire Quantum Dots,” Phys. Rev. Lett., vol. 121, p. 206801, Nov 2018.
- [38] B. Dutta, D. Majidi, A. Garcia Corral, P. A. Erdman, S. Florens, T. A. Costi, H. Courtois, and C. B. Winkelmann, “Direct Probe of the Seebeck Coefficient in a Kondo-Correlated Single-Quantum-Dot Transistor,” Nano Letters, vol. 19, no. 1, pp. 506–511, 2019.
- [39] A. A. Abrikosov, “Electron scattering on magnetic impurities in metals and anomalous resistivity effects,” Physics, vol. 2, no. 1, pp. 5–20, 1965.
- [40] H. Shul, “Paramagnetic impurities in metals at finite temperatures,” Physics, vol. 2, no. 1, pp. 39–59, 1965.
- [41] A. A. Abrikosov and A. A. Migdal, “Exact Results in the Kondo Problem: Equivalence to a Classical One-Dimensional Coulomb Gas,” J. Low Temp. Phys., vol. 3, p. 519, 1970.
- [42] A. M. Tsvetlik and P. B. Wiegmann, “Exact results in the theory of magnetic alloys,” Advances in Physics, vol. 32, p. 453, 1983.

-
- [43] P. D. Sacramento and P. Schlottmann, “Thermodynamics of the n-channel Kondo model for general n and impurity spin S in a magnetic field,” J. Phys.: Condens. Matter, vol. 3, no. 48, p. 9687, 1991.
- [44] N. Andrei and C. Destri, “Solution of the Multichannel Kondo Problem,” Phys. Rev. Lett., vol. 52, pp. 364–367, Jan 1984.
- [45] A. Posazhennikova and P. Coleman, “Anomalous Conductance of a Spin-1 Quantum Dot,” Phys. Rev. Lett., vol. 94, pp. 036802–4, 2005.
- [46] W. Koller, A. C. Hewson, and D. Meyer, “Singular dynamics of underscreened magnetic impurity models,” Phys. Rev. B, vol. 72, p. 045117, Jul 2005.
- [47] S. Sasaki, S. De Franceschi, J. M. Elzerman, W. G. van der Wiel, M. Eto, S. Tarucha, and L. P. Kouwenhoven, “Kondo effect in an integer-spin quantum dot,” Nature, vol. 405, pp. 764–767, 2000.
- [48] M. Eto and Y. V. Nazarov, “Enhancement of Kondo Effect in Quantum Dots with an Even Number of Electrons,” Phys. Rev. Lett., vol. 85, pp. 1306–1309, Aug 2000.
- [49] M. Pustilnik and L. I. Glazman, “Kondo Effect in Real Quantum Dots,” Phys. Rev. Lett., vol. 87, p. 216601, 2001.
- [50] A. Kogan, G. Granger, M. A. Kastner, D. Goldhaber-Gordon, and H. Shtrikman, “Singlet-triplet transition in a single-electron transistor at zero magnetic field,” Phys. Rev. B, vol. 67, p. 113309, Mar 2003.
- [51] C. H. L. Quay, J. Cumings, S. J. Gamble, R. d. Picciotto, H. Kataura, and D. Goldhaber-Gordon, “Magnetic field dependence of the spin- $\frac{1}{2}$ and spin-1 Kondo effects in a quantum dot,” Phys. Rev. B, vol. 76, p. 245311, Dec 2007.
- [52] S. Di Napoli, M. A. Barral, P. Roura-Bas, L. O. Manuel, A. M. Llois, and A. A. Aligia, “Kondo physics in a Ni impurity embedded in O-doped Au chains,” Phys. Rev. B, vol. 92, p. 085120, Aug 2015.
- [53] P. Coleman, L. B. Ioffe, and A. M. Tsvelik, “Simple formulation of the two-channel Kondo model,” Phys. Rev. B, vol. 52, pp. 6611–6627, 1995.
- [54] S. Datta, Electronic Transport in Mesoscopic Systems. Cambridge Studies in Semiconductor Physics and Microelectronic Engineering, Cambridge University Press, 1995.
- [55] M. S. Dresselhaus, G. Dresselhaus, X. Sun, Z. Zhang, S. B. Cronin, and T. Koga, “Low-dimensional thermoelectric materials,” Physics of the Solid State, vol. 41, pp. 679–682, May 1999.
- [56] M. Dresselhaus, G. Chen, M. Tang, R. Yang, H. Lee, D. Wang, Z. Ren, J.-P. Fleurial, and P. Gogna, “New Directions for Low-Dimensional Thermoelectric Materials,” Advanced Materials, vol. 19, no. 8, pp. 1043–1053, 2007.

- [57] G. Benenti, G. Casati, K. Saito, and R. Whitney, “Fundamental aspects of steady-state conversion of heat to work at the nanoscale,” Physics Reports, vol. 694, pp. 1 – 124, 2017. Fundamental aspects of steady-state conversion of heat to work at the nanoscale.
- [58] B. J. van Wees, H. van Houten, C. W. J. Beenakker, J. G. Williamson, L. P. Kouwenhoven, D. van der Marel, and C. T. Foxon, “Quantized conductance of point contacts in a two-dimensional electron gas,” Phys. Rev. Lett., vol. 60, pp. 848–850, Feb 1988.
- [59] Y. M. Blanter and Y. V. Nazarov, Quantum Transport: Introduction to Nanoscience. Cambridge University Press, Cambridge, England, 2009.
- [60] L. P. Kouwenhoven, D. G. Austing, and S. Tarucha, “Few-electron quantum dots,” Reports on Progress in Physics, vol. 64, pp. 701–736, may 2001.
- [61] R. Hanson, L. P. Kouwenhoven, J. R. Petta, S. Tarucha, and L. M. K. Vandersypen, “Spins in few-electron quantum dots,” Rev. Mod. Phys., vol. 79, pp. 1217–1265, Oct 2007.
- [62] V. Zlatic and R. Monnier, Modern Theory of Thermoelectricity. Oxford University Press, 2014.
- [63] L. Onsager, “Reciprocal Relations in Irreversible Processes. I.,” Phys. Rev., vol. 37, pp. 405–426, Feb 1931.
- [64] L. Onsager, “Reciprocal Relations in Irreversible Processes. II.,” Phys. Rev., vol. 38, pp. 2265–2279, Dec 1931.
- [65] T. A. Costi and V. Zlatic, “Thermoelectric transport through strongly correlated quantum dots,” Phys. Rev. B, vol. 81, p. 235127, Jun 2010.
- [66] T.-S. Kim and S. Hershfield, “Thermoelectric effects of an Aharonov-Bohm interferometer with an embedded quantum dot in the Kondo regime,” Phys. Rev. B, vol. 67, p. 165313, Apr 2003.
- [67] J. Azema, A.-M. Daré, S. Schäfer, and P. Lombardo, “Kondo physics and orbital degeneracy interact to boost thermoelectrics on the nanoscale,” Phys. Rev. B, vol. 86, p. 075303, Aug 2012.
- [68] P. Jarillo-Herrero, J. Kong, H. S. van der Zant, C. Dekker, L. P. Kouwenhoven, and S. D. Franceschi, “Orbital Kondo effect in carbon nanotubes,” Nature, vol. 434, pp. 484–488, 2005.
- [69] A. Makarovski, J. Liu, and G. Finkelstein, “Evolution of Transport Regimes in Carbon Nanotube Quantum Dots,” Phys. Rev. Lett., vol. 99, p. 066801, Aug 2007.
- [70] A. Makarovski, A. Zhukov, J. Liu, and G. Finkelstein, “SU(2) and SU(4) Kondo effects in carbon nanotube quantum dots,” Phys. Rev. B, vol. 75, p. 241407, Jun 2007.
- [71] M. Ferrier, T. Arakawa, T. Hata, R. Fujiwara, R. Delagrangé, R. Deblock, Y. Teratani, R. Sakano, A. Oguri, and K. Kobayashi, “Quantum Fluctuations along Symmetry Crossover in a Kondo-Correlated Quantum Dot,” Phys. Rev. Lett., vol. 118, p. 196803, May 2017.

- [72] T. Hata, R. Delagrangé, T. Arakawa, S. Lee, R. Deblock, H. Bouchiat, K. Kobayashi, and M. Ferrier, “Enhanced Shot Noise of Multiple Andreev Reflections in a Carbon Nanotube Quantum Dot in SU(2) and SU(4) Kondo regimes,” Phys. Rev. Lett., vol. 121, p. 247703, Dec 2018.
- [73] A. J. Keller, S. Amasha, I. Weymann, C. P. Moca, I. G. Rau, J. A. Katine, H. Shtrikman, G. Zarand, and D. Goldhaber-Gordon, “Emergent SU(4) Kondo physics in a spin charge entangled double quantum dot,” Nature Physics, vol. 10, pp. 145–150, 2014.
- [74] G. C. Tettamanzi, J. Verduijn, G. P. Lansbergen, M. Blaauboer, M. J. Calderón, R. Aguado, and S. Rogge, “Magnetic-Field Probing of an SU(4) Kondo Resonance in a Single-Atom Transistor,” Phys. Rev. Lett., vol. 108, p. 046803, Jan 2012.
- [75] K. Le Hur, P. Simon, and D. Loss, “Transport through a quantum dot with SU(4) Kondo entanglement,” Phys. Rev. B, vol. 75, p. 035332, Jan 2007.
- [76] M.-S. Choi, R. López, and R. Aguado, “SU(4) Kondo Effect in Carbon Nanotubes,” Phys. Rev. Lett., vol. 95, p. 067204, Aug 2005.
- [77] M. Eto, “Enhancement of Kondo Effect in Multilevel Quantum Dots,” Journal of the Physical Society of Japan, vol. 74, no. 1, pp. 95–102, 2005.
- [78] J. S. Lim, M.-S. Choi, M. Y. Choi, R. López, and R. Aguado, “Kondo effects in carbon nanotubes: From SU(4) to SU(2) symmetry,” Phys. Rev. B, vol. 74, p. 205119, Nov 2006.
- [79] J. S. Lim, R. López, and D. Sánchez, “Orbital caloritronic transport in strongly interacting quantum dots,” New Journal of Physics, vol. 16, p. 015003, Jan 2014.
- [80] Y. Kleeorin and Y. Meir, “Abrupt disappearance and re-emergence of the SU(4) and SU(2) Kondo effects due to population inversion,” Phys. Rev. B, vol. 96, p. 045118, Jul 2017.
- [81] A. Carmi, Y. Oreg, and M. Berkooz, “Realization of the SU(N) Kondo Effect in a Strong Magnetic Field,” Phys. Rev. Lett., vol. 106, p. 106401, Mar 2011.
- [82] R. López, T. c. v. Rejec, J. Martinek, and R. Žitko, “SU(3) Kondo effect in spinless triple quantum dots,” Phys. Rev. B, vol. 87, p. 035135, Jan 2013.
- [83] T. Kita, R. Sakano, T. Ohashi, and S.-i. Suga, “Three-Orbital Kondo Effect in Single Quantum Dot System with Plural Electrons,” Journal of the Physical Society of Japan, vol. 77, no. 9, p. 094707, 2008.
- [84] I. Kuzmenko and Y. Avishai, “SU(12) Kondo effect in a carbon nanotube quantum dot,” Phys. Rev. B, vol. 89, p. 195110, May 2014.
- [85] Y. Nishida, “SU(3) Orbital Kondo Effect with Ultracold Atoms,” Phys. Rev. Lett., vol. 111, p. 135301, Sep 2013.
- [86] J. Bauer, C. Salomon, and E. Demler, “Realizing a Kondo-Correlated State with Ultracold Atoms,” Phys. Rev. Lett., vol. 111, p. 215304, Nov 2013.

- [87] Y. Nishida, “Transport measurement of the orbital Kondo effect with ultracold atoms,” Phys. Rev. A, vol. 93, p. 011606, Jan 2016.
- [88] I. Kuzmenko, T. Kuzmenko, Y. Avishai, and G.-B. Jo, “Coqblin-Schrieffer model for an ultracold gas of ytterbium atoms with metastable state,” Phys. Rev. B, vol. 93, p. 115143, Mar 2016.
- [89] A. Posazhennikova, B. Bayani, and P. Coleman, “Conductance of a spin-1 quantum dot: The two-stage Kondo effect,” Phys. Rev. B, vol. 75, pp. 245329–15, 2007.
- [90] R. S. Whitney, “Most Efficient Quantum Thermoelectric at Finite Power Output,” Phys. Rev. Lett., vol. 112, p. 130601, Apr 2014.
- [91] R. S. Whitney, “Finding the quantum thermoelectric with maximal efficiency and minimal entropy production at given power output,” Phys. Rev. B, vol. 91, p. 115425, Mar 2015.
- [92] I.-J. Chen, A. Burke, A. Svilans, H. Linke, and C. Thelander, “Thermoelectric Power Factor Limit of a 1D Nanowire,” Phys. Rev. Lett., vol. 120, p. 177703, Apr 2018.
- [93] A. O. Gogolin and A. Komnik, “Full Counting Statistics for the Kondo Dot in the Unitary Limit,” Phys. Rev. Lett., vol. 97, p. 016602, 2006.
- [94] A. O. Gogolin and A. Komnik, “Towards full counting statistics for the Anderson impurity model,” Phys. Rev. B, vol. 73, p. 195301, 2006.
- [95] T. L. Schmidt, A. O. Gogolin, and A. Komnik, “Full counting statistics of spin transfer through a Kondo dot,” Phys. Rev. B, vol. 75, p. 235105, Jun 2007.
- [96] T. L. Schmidt, A. Komnik, and A. O. Gogolin, “Full counting statistics of spin transfer through ultrasmall quantum dots,” Phys. Rev. B, vol. 76, p. 241307, Dec 2007.
- [97] R. Sakano, Y. Nishikawa, A. Oguri, A. C. Hewson, and S. Tarucha, “Full Counting Statistics for Orbital-Degenerate Impurity Anderson Model with Hund’s Rule Exchange Coupling,” Phys. Rev. Lett., vol. 108, p. 266401, Jun 2012.
- [98] F. L. Curzon and B. Ahlborn, “Efficiency of a Carnot engine at maximum power output,” American Journal of Physics, vol. 43, no. 1, pp. 22–24, 1975.
- [99] C. Van den Broeck, “Thermodynamic Efficiency at Maximum Power,” Phys. Rev. Lett., vol. 95, p. 190602, Nov 2005.
- [100] B. Jiménez de Cisneros and A. C. Hernández, “Collective Working Regimes for Coupled Heat Engines,” Phys. Rev. Lett., vol. 98, p. 130602, Mar 2007.
- [101] M. Esposito, K. Lindenberg, and C. V. den Broeck, “Thermoelectric efficiency at maximum power in a quantum dot,” EPL (Europhysics Letters), vol. 85, p. 60010, mar 2009.
- [102] R. S. Whitney, “Thermodynamic and quantum bounds on nonlinear dc thermoelectric transport,” Phys. Rev. B, vol. 87, p. 115404, Mar 2013.

- [103] D. Goldhaber-Gordon, H. Shtrikman, D. Mahalu, D. Abusch-Magder, U. Meirav, and M. A. Kastner, “Kondo effect in a single-electron transistor,” Nature, vol. 391, pp. 156–159, 1998.
- [104] S. M. Cronenwett, T. H. Oosterkamp, and L. P. Kouwenhoven, “A Tunable Kondo Effect in Quantum Dots,” Science, vol. 281, no. 5376, pp. 540–544, 1998.
- [105] J. Nygåard, D. H. Cobden, and P. E. Lindelof, “Kondo physics in carbon nanotubes,” Nature, vol. 408, pp. 342–346, 2000.
- [106] C. Mora, P. Vitushinsky, X. Leyronas, A. A. Clerk, and K. Le Hur, “Theory of nonequilibrium transport in the $SU(N)$ Kondo regime,” Phys. Rev. B, vol. 80, p. 155322, Oct 2009.
- [107] C. Mora, “Fermi-Liquid theory for $SU(N)$ Kondo model,” Phys. Rev. B, vol. 80, pp. 125304–7, 2009.
- [108] L. W. Molenkamp, H. V. Houten, C. W. J. Beenakker, R. Eppenga, and C. T. Foxon, “Quantum oscillations in the transverse voltage of a channel in the nonlinear transport regime,” Phys. Rev. Lett., vol. 65, p. 1052, 1990.
- [109] H. V. Houten, L. W. Molenkamp, C. W. J. Beenakker, and C. T. Foxon, “Thermo-electric properties of quantum point contacts,” Semicond. Sci. Technol., vol. 7, p. B215, 1992.
- [110] H. R. Krishna-murthy, J. W. Wilkins, and K. G. Wilson, “Renormalization-group approach to the Anderson model of dilute magnetic alloys. I. Static properties for the symmetric case,” Phys. Rev. B, vol. 21, pp. 1003–1043, Feb 1980.
- [111] L. I. Glazman and M. E. Raikh, “Resonant Kondo Transparency of a barrier with quasilocal impurity states,” J. Exp. Theor. Phys., vol. 27, pp. 452–455, 1988.
- [112] J. R. Schrieffer and P. A. Wolff, “Relation between the Anderson and Kondo Hamiltonians,” Phys. Rev., vol. 149, pp. 491–492, Sep 1966.
- [113] O. Parcollet, A. Georges, G. Kotliar, and A. Sengupta, “Overscreened multichannel $SU(N)$ Kondo model: Large N solution and conformal field theory,” Phys. Rev. B, vol. 58, pp. 3794–3813, Aug 1998.
- [114] D. L. Cox and A. Zawadowski, “Exotic Kondo effects in metals: Magnetic ions in a crystalline electric field and tunnelling centres,” Advances in Physics, vol. 47, no. 5, pp. 599–942, 1998.
- [115] L. V. Keldysh, “Diagram technique for nonequilibrium processes,” Sov. Phys. JETP, vol. 20, no. 4, pp. 1018–1026, 1965.
- [116] C. W. J. Beenakker and A. A. M. Staring, “Theory of the thermopower of a quantum dot,” Phys. Rev. B, vol. 46, pp. 9667–9676, Oct 1992.
- [117] L. W. Molenkamp, T. Gravier, H. van Houten, O. J. A. Buijk, M. A. A. Mabeoone, and C. T. Foxon, “Peltier coefficient and thermal conductance of a quantum point contact,” Phys. Rev. Lett., vol. 68, pp. 3765–3768, Jun 1992.

- [118] T.-S. Kim and S. Hershfield, “Thermopower of an Aharonov-Bohm Interferometer: Theoretical Studies of Quantum Dots in the Kondo Regime,” Phys. Rev. Lett., vol. 88, p. 136601, Mar 2002.
- [119] K. A. Matveev and A. V. Andreev, “Thermopower of a single-electron transistor in the regime of strong inelastic cotunneling,” Phys. Rev. B, vol. 66, p. 045301, Jul 2002.
- [120] A. Carmi, Y. Oreg, M. Berkooz, and D. Goldhaber-Gordon, “Transmission phase shifts of Kondo impurities,” Phys. Rev. B, vol. 86, p. 115129, Sep 2012.
- [121] M. Pustilnik and L. I. Glazman, “Kondo Effect in Real Quantum Dots,” Phys. Rev. Lett., vol. 87, p. 216601, Nov 2001.
- [122] M. Pustilnik and L. Glazman, “Kondo effect in quantum dots,” Journal of Physics: Condensed Matter, vol. 16, pp. R513–R537, apr 2004.
- [123] M. Pustilnik, L. Borda, L. I. Glazman, and J. von Delft, “Quantum phase transition in a two-channel-Kondo quantum dot device,” Phys. Rev. B, vol. 69, p. 115316, Mar 2004.
- [124] J. Park, S.-S. B. Lee, Y. Oreg, and H.-S. Sim, “How to Directly Measure a Kondo Cloud’s Length,” Phys. Rev. Lett., vol. 110, p. 246603, Jun 2013.
- [125] A. Dorda, M. Ganahl, S. Andergassen, W. von der Linden, and E. Arrigoni, “Thermoelectric response of a correlated impurity in the nonequilibrium Kondo regime,” Phys. Rev. B, vol. 94, p. 245125, Dec 2016.
- [126] D. Pérez Daroca, P. Roura-Bas, and A. A. Aligia, “Enhancing the nonlinear thermoelectric response of a correlated quantum dot in the Kondo regime by asymmetrical coupling to the leads,” Phys. Rev. B, vol. 97, p. 165433, Apr 2018.
- [127] U. Eckern and K. I. Wysokiński, “Multi-terminal far-from-equilibrium thermoelectric nano-devices in the Kondo regime,” arXiv e-prints, p. arXiv:1904.05064, Apr 2019.
- [128] E. N. Bogachev, A. G. Scherbakov, and U. Landman, “Nonlinear Peltier effect and thermo-conductance in nanowires,” Phys. Rev. B, vol. 60, pp. 11678–11682, Oct 1999.
- [129] R. López and D. Sánchez, “Nonlinear heat transport in mesoscopic conductors: Rectification, Peltier effect, and Wiedemann-Franz law,” Phys. Rev. B, vol. 88, p. 045129, Jul 2013.
- [130] R. López, S.-Y. Hwang, and D. Sánchez, “Thermoelectric effects in quantum Hall systems beyond linear response,” Journal of Physics: Conference Series, vol. 568, p. 052016, dec 2014.
- [131] M. A. Sierra and D. Sánchez, “Strongly nonlinear thermovoltage and heat dissipation in interacting quantum dots,” Phys. Rev. B, vol. 90, p. 115313, Sep 2014.
- [132] D. Boese and R. Fazio, “Thermoelectric effects in Kondo-correlated quantum dots,” Europhysics Letters (EPL), vol. 56, pp. 576–582, nov 2001.
- [133] M. Pustilnik and L. I. Glazman, “Kondo effect induced by a magnetic field,” Phys. Rev. B, vol. 64, pp. 045328–15, 2001.

-
- [134] W. Hofstetter and H. Schoeller, “Quantum phase transition in a Multilevel dot,” Phys. Rev. Lett., vol. 88, p. 016803, 2001.
- [135] M. Pustilnik, L. I. Glazman, and W. Hofstetter, “Singlet-triplet transition in a lateral quantum dot,” Phys. Rev. B, vol. 68, p. 161303(R), 2003.
- [136] W. Hofstetter and G. Zarand, “Singlet-triplet transition in lateral quantum dots: A numerical renormalization group study,” Phys. Rev. B, vol. 69, p. 235301, Jun 2004.
- [137] R. M. Potok, I. G. Rau, H. Shtrikman, Y. Oreg, and D. Goldhaber-Gordon, “Observation of the two-channel Kondo effect,” Nature, vol. 446, pp. 167–171, 2007.
- [138] D. C. Ralph and R. A. Buhrman, “Observations of Kondo scattering without magnetic impurities: A point contact study of two-level tunneling systems in metals,” Phys. Rev. Lett., vol. 69, pp. 2118–2121, Oct 1992.
- [139] D. C. Ralph and R. A. Buhrman, “Kondo scattering from atomic two-level tunneling systems in metals: Enhanced conductance, critical-bias transitions, and the non-Fermi-liquid electronic state,” Phys. Rev. B, vol. 51, pp. 3554–3568, 1995.
- [140] W. G. van der Wiel, S. De Franceschi, J. M. Elzerman, S. Tarucha, L. P. Kouwenhoven, J. Motohisa, F. Nakajima, and T. Fukui, “Two-Stage Kondo Effect in a Quantum Dot at a High Magnetic Field,” Phys. Rev. Lett., vol. 88, p. 126803, Mar 2002.
- [141] K. A. Matveev, “Coulomb blockade at almost perfect transmission,” Phys. Rev. B, vol. 51, pp. 1743–1751, 1995.
- [142] A. Rosch, J. Kroha, and P. Wolfle, “Kondo Effect in Quantum Dots at High Voltage: Universality and Scaling,” Phys. Rev. Lett., vol. 87, pp. 156802–4, 2001.
- [143] Y. Oreg and D. Goldhaber-Gordon, “Two-Channel Kondo Effect in a Modified Single Electron Transistor,” Phys. Rev. Lett., vol. 90, pp. 136602–4, 2003.
- [144] K. A. Matveev, “Coulomb blockade at almost perfect transmission,” Phys. Rev. B, vol. 51, p. 1743, 1995.
- [145] S. Tarucha, D. G. Austing, Y. Tokura, W. G. van der Wiel, and L. P. Kouwenhoven, “Direct Coulomb and Exchange Interaction in Artificial Atoms,” Phys. Rev. Lett., vol. 84, pp. 2485–2488, Mar 2000.
- [146] P. W. Anderson, “A poor man’s derivation of scaling laws for the Kondo problem,” J. Phys. C, vol. 3, no. 12, p. 2436, 1970.
- [147] M. Hanl, A. Weichselbaum, J. von Delft, and M. Kiselev, “Equilibrium Fermi-liquid coefficients for the fully screened N-channel Kondo model,” Phys. Rev. B, vol. 89, pp. 195131–11, 2014.
- [148] C. Mora, C. P. Moca, J. von Delft, and G. Zaránd, “Fermi-liquid theory for the single-impurity Anderson model,” Phys. Rev. B, vol. 92, pp. 075120–14, 2015.

- [149] M. Filippone, C. P. Moca, J. von Delft, and C. Mora, “At which magnetic field, exactly, does the Kondo resonance begin to split? A Fermi liquid description of the low-energy properties of the Anderson model,” Phys. Rev. B, vol. 95, p. 165404, 2017.
- [150] A. O. Gogolin, A. A. Nersesyan, and A. M. Tsvelik, Bosonization and strongly correlated systems. Cambridge University Press, Cambridge, 1998.
- [151] C. Mora, X. Leyronas, and N. Regnault, “Current Noise through a Kondo Quantum Dot in a $SU(N)$ Fermi Liquid State,” Phys. Rev. Lett., vol. 100, pp. 036604–4, 2008.
- [152] P. Vitushinsky, A. A. Clerk, and K. L. Hur, “Effects of Fermi Liquid Interactions on the Shot Noise of an $SU(N)$ Kondo Quantum Dot,” Phys. Rev. Lett., vol. 100, pp. 036603–4, 2008.
- [153] F. Bauer, J. Heyder, E. Schubert, D. Borowsky, D. Taubert, B. Bruognolo, D. Schuh, W. Wegscheider, J. von Delft, and S. Ludwig, “Microscopic origin of the ”0.7-anomaly” in quantum point contacts,” Nature, vol. 501, pp. 73–78, 2013.
- [154] T. Rejec and Y. Meir, “Magnetic impurity formation in quantum point contacts,” Nature, vol. 442, pp. 900–903, 2006.
- [155] L. S. Levitov and G. B. Lesovik, “Charge distribution in quantum shot noise,” JETP Lett., vol. 58, p. 230, 1993.
- [156] Y. V. Nazarov, ed., Quantum Noise in Mesoscopic Systems. Kluwer, Dordrecht, 2003.
- [157] A. Oguri and A. C. Hewson, “Higher-Order Fermi-Liquid Corrections for an Anderson Impurity Away from Half Filling,” Phys. Rev. Lett., vol. 120, p. 126802, Mar 2018.
- [158] A. Oguri and A. C. Hewson, “Higher-order Fermi-liquid corrections for an Anderson impurity away from half filling : Equilibrium properties,” Phys. Rev. B, vol. 97, p. 045406, 2018.
- [159] A. Oguri and A. C. Hewson, “Higher-order Fermi-liquid corrections for an Anderson impurity away from half filling: Nonequilibrium transport,” Phys. Rev. B, vol. 97, p. 035435, 2018.
- [160] Y. Blanter and M. Buttiker, “Shot noise in mesoscopic conductors,” Physics Reports, vol. 336, no. 1, pp. 1 – 166, 2000.
- [161] H. Lee, L. S. Levitov, and A. Y. Yakovets, “Universal statistics of transport in disordered conductors,” Phys. Rev. B, vol. 51, pp. 4079–4083, Feb 1995.
- [162] L. S. Levitov, H. Lee, and G. B. Lesovik, “Electron counting statistics and coherent states of electric current,” Journal of Mathematical Physics, vol. 37, p. 4845, 1996.
- [163] D. A. Bagrets and Y. V. Nazarov, “Full counting statistics of charge transfer in Coulomb blockade systems,” Phys. Rev. B, vol. 67, p. 085316, Feb 2003.
- [164] L. S. Levitov and M. Reznikov, “Counting statistics of tunneling current,” Phys. Rev. B, vol. 70, p. 115305, 2004.

-
- [165] S. Gustavsson, R. Leturcq, B. Simovič, R. Schleser, T. Ihn, P. Studerus, K. Ensslin, D. C. Driscoll, and A. C. Gossard, “Counting Statistics of Single Electron Transport in a Quantum Dot,” Phys. Rev. Lett., vol. 96, p. 076605, Feb 2006.
- [166] W. Belzig, “Full counting statistics of super-Poissonian shot noise in multilevel quantum dots,” Phys. Rev. B, vol. 71, p. 161301, Apr 2005.
- [167] A. A. Clerk, M. H. Devoret, S. M. Girvin, F. Marquardt, and R. J. Schoelkopf, “Introduction to quantum noise, measurement, and amplification,” Rev. Mod. Phys., vol. 82, pp. 1155–1208, Apr 2010.
- [168] B. Reulet, J. Senzier, and D. E. Prober, “Environmental Effects in the Third Moment of Voltage Fluctuations in a Tunnel Junction,” Phys. Rev. Lett., vol. 91, p. 196601, Nov 2003.
- [169] Y. Bomze, G. Gershon, D. Shovkun, L. S. Levitov, and M. Reznikov, “Measurement of Counting Statistics of Electron Transport in a Tunnel Junction,” Phys. Rev. Lett., vol. 95, p. 176601, Oct 2005.
- [170] T. Fujisawa, T. Hayashi, R. Tomita, and Y. Hirayama, “Bidirectional Counting of Single Electrons,” Science, vol. 312, no. 5780, pp. 1634–1636, 2006.
- [171] C. Fricke, F. Hohls, W. Wegscheider, and R. J. Haug, “Bimodal counting statistics in single-electron tunneling through a quantum dot,” Phys. Rev. B, vol. 76, p. 155307, Oct 2007.
- [172] A. V. Timofeev, M. Meschke, J. T. Peltonen, T. T. Heikkilä, and J. P. Pekola, “Wideband Detection of the Third Moment of Shot Noise by a Hysteretic Josephson Junction,” Phys. Rev. Lett., vol. 98, p. 207001, May 2007.
- [173] G. Gershon, Y. Bomze, E. V. Sukhorukov, and M. Reznikov, “Detection of Non-Gaussian Fluctuations in a Quantum Point Contact,” Phys. Rev. Lett., vol. 101, p. 016803, Jul 2008.
- [174] J. Gabelli and B. Reulet, “Full counting statistics of avalanche transport: An experiment,” Phys. Rev. B, vol. 80, p. 161203, Oct 2009.
- [175] C. Flindt, C. Fricke, F. Hohls, T. Novotný, K. Netočný, T. Brandes, and R. J. Haug, “Universal oscillations in counting statistics,” Proceedings of the National Academy of Sciences, vol. 106, no. 25, pp. 10116–10119, 2009.
- [176] B. A. Muzykantskii and D. E. Khmelnitskii, “Quantum shot noise in a normal-metal–superconductor point contact,” Phys. Rev. B, vol. 50, pp. 3982–3987, Aug 1994.
- [177] W. Belzig and Y. V. Nazarov, “Full Current Statistics in Diffusive Normal-Superconductor Structures,” Phys. Rev. Lett., vol. 87, p. 067006, Jul 2001.
- [178] S. Pilgram, A. N. Jordan, E. V. Sukhorukov, and M. Büttiker, “Stochastic Path Integral Formulation of Full Counting Statistics,” Phys. Rev. Lett., vol. 90, p. 206801, May 2003.
- [179] F. Taddei and R. Fazio, “Counting statistics for entangled electrons,” Phys. Rev. B, vol. 65, p. 075317, Feb 2002.

-
- [180] A. Di Lorenzo and Y. V. Nazarov, “Full Counting Statistics of Spin Currents,” Phys. Rev. Lett., vol. 93, p. 046601, Jul 2004.
- [181] A. Braggio, J. König, and R. Fazio, “Full Counting Statistics in Strongly Interacting Systems: Non-Markovian Effects,” Phys. Rev. Lett., vol. 96, p. 026805, Jan 2006.
- [182] F. Pistolesi, “Full counting statistics of a charge shuttle,” Phys. Rev. B, vol. 69, p. 245409, Jun 2004.
- [183] S. D. Bennett and A. A. Clerk, “Full counting statistics and conditional evolution in a nano-electromechanical system,” Phys. Rev. B, vol. 78, p. 165328, Oct 2008.
- [184] D. Kambly, C. Flindt, and M. Büttiker, “Factorial cumulants reveal interactions in counting statistics,” Phys. Rev. B, vol. 83, p. 075432, Feb 2011.
- [185] N. E. Bickers, D. L. Cox, and J. W. Wilkins, “Thermodynamic, Transport, and Excitation Properties of Ce Impurities in a Model Metal: Kondo Resonance and Universality in the Mixed-Valent Regime,” Phys. Rev. Lett., vol. 54, pp. 230–233, Jan 1985.
- [186] J. Nygåard, D. H. Cobden, and P. E. Lindelof, “Kondo physics in carbon nanotubes,” Nature, vol. 408, pp. 342–346, 2000.
- [187] A. Golub, “Shot noise near the unitary limit of a Kondo quantum dot,” Phys. Rev. B, vol. 73, p. 233310, Jun 2006.
- [188] C. H. L. Quay, J. Cumings, S. J. Gamble, R. d. Picciotto, H. Kataura, and D. Goldhaber-Gordon, “Magnetic field dependence of the spin- $\frac{1}{2}$ and spin-1 Kondo effects in a quantum dot,” Phys. Rev. B, vol. 76, p. 245311, Dec 2007.
- [189] A. K. Mitchell, K. G. L. Pedersen, P. Hedegard, and J. Paaske, “Kondo blockade due to quantum interference in single-molecule junctions,” Nature Communications, vol. 8, p. 15210, 2017.
- [190] E. Sela, Y. Oreg, F. von Oppen, and J. Koch, “Fractional Shot Noise in the Kondo Regime,” Phys. Rev. Lett., vol. 97, pp. 086601–4, 2006.